HAL
open science

Study and analysis of premixed flame dynamics of zero carbon fuel - ammonia

Alka Karan

To cite this version:

Alka Karan. Study and analysis of premixed flame dynamics of zero carbon fuel - ammonia. Thermics [physics.class-ph]. Université d'Orléans, 2022. English. NNT : 2022ORLE1008 . tel-04105590v2

HAL Id: tel-04105590

https://theses.hal.science/tel-04105590v2

Submitted on 24 May 2023

HAL is a multi-disciplinary open access archive for the deposit and dissemination of scientific research documents, whether they are published or not. The documents may come from teaching and research institutions in France or abroad, or from public or private research centers.

L'archive ouverte pluridisciplinaire **HAL**, est destinée au dépôt et à la diffusion de documents scientifiques de niveau recherche, publiés ou non, émanant des établissements d'enseignement et de recherche français ou étrangers, des laboratoires publics ou privés.

UNIVERSITY OF ORLEANS

ÉCOLE DOCTORALE ÉNERGIE, MATÉRIAUX, SCIENCES DE LA TERRE ET DE L'UNIVERS

INSTITUT DE COMBUSTION, AÉROTHERMIQUE, RÉACTIVITÉ ET ENVIRONNEMENT

THESIS dissertation by :

Alka KARAN

presented on : **14 November 2022**

In partial fulfillment of the requirements for the degree of : **Doctor of Philosophy**

Discipline/ Speciality : **Energy**

Study and analysis of premixed flame dynamics of zero carbon fuel – ammonia

Thesis directed by :

Fabien HALTER	Professor, University of Orleans, ICARE-CNRS
Christian CHAUVEAU	Director of Research, ICARE-CNRS

EXAMINATORS :

Julien SOTTON	Professor, ISAE-ENSMA, Institut PPrime-CNRS
Thibault GUIBERTI	Assistant Professor, KAUST

JURY :

Christine ROUSELLE	Professor, University of Orleans, President of jury
Olivier MATHIEU	Associate Professor, Texas A& M University
Guillaume DAYMA	Professor, University of Orleans, ICARE-CNRS
Julien SOTTON	Professeur, ISAE-ENSMA, Institut PPrime-CNRS
Thibault GUIBERTI	Assistant Professor, KAUST
Fabien THIESSET	Chargé de Recherche, CORIA-CNRS

UNIVERSITÉ D'ORLÉANS

ÉCOLE DOCTORALE ÉNERGIE, MATÉRIAUX, SCIENCES DE LA TERRE ET DE L'UNIVERS

INSTITUT DE COMBUSTION, AÉROTHERMIQUE, RÉACTIVITÉ ET ENVIRONNEMENT

THÈSE présentée par :

Alka KARAN

soutenue le : **14 Novembre 2022**

pour obtenir le grade de : **Docteur de l'Université d'Orléans**

Discipline/ Spécialité : **Enérgetique**

Etude et analyse de la dynamique de flammes prémélangées d'un carburant zéro carbone - ammoniac

Thèse dirigée par :

Fabien HALTER	Professeur, Université d'Orléans, ICARE-CNRS
Christian CHAUVEAU	Directeur de Recherche, ICARE-CNRS

RAPPORTEURS :

Julien SOTTON	Professeur, ISAE-ENSMA, Institut PPrime-CNRS
Thibault GUIBERTI	Assistant Professor, KAUST

JURY :

Christine ROUSELLE	Professeur, Université d'Orléans, Présidente du jury
Olivier MATHIEU	Associate Professor, Texas A& M University
Guillaume DAYMA	Professeur, Université d'Orléans, ICARE-CNRS
Julien SOTTON	Professeur, ISAE-ENSMA, Institut PPrime-CNRS
Thibault GUIBERTI	Assistant Professor, KAUST
Fabien THIESSET	Chargé de Recherche, CORIA-CNRS

Alka KARAN

Etude et analyse de la dynamique de flammes prémélangées d'un carburant zéro carbone - ammoniac

Résumé :
Dans le cadre de la recherche de carburants alternatifs pour atténuer la pollution, le réchauffement climatique, l'épuisement des ressources, etc., l'ammoniac est apparu comme l'un des principaux candidats parmi les autres carburants verts. L'objectif de cette thèse est de fournir des données expérimentales et des analyses qui soient utiles à la fois à l'industrie et à la communauté scientifique. Ce travail a été divisé en 3 parties pour atteindre les objectifs fixés. La première partie est dédiée à fournir des vitesses de flamme laminaire, qui est un paramètre de dimensionnement important pour les chambres de combustion. Cette section met également en évidence la chimie impliquée et les différents facteurs qui l'influencent, expliquant certains comportements atypique comme l'indépendance vis-à-vis de la pression. La deuxième partie est une tentative de compréhension de la structure interne des flammes d'ammoniac. Il est important de comprendre la réponse des différentes espèces aux changements de paramètres. Cela permet de mieux paramétrer la combustion en fonction des besoins. L'épaisseur de la flamme d'ammoniac a été calculé. Cette épaisseur influe sur le calcul de la vitesse de flamme. De plus, la courbure impacte les différentes espèces excitées, ce qui modifie la position du taux de libération de chaleur. La dernière partie de cette thèse est une étude approfondie de la deuxième partie. La concentration de certaines des espèces excitées, qui est utile pour s'adapter à tout schéma cinétique, a été donnée. Il est connu que les flammes turbulentes permettent d'améliorer certaines propriétés souhaitables. Cependant, les flammes turbulentes sont très complexes et ne sont pas faciles à analyser. La première étape est d'étudier une flamme perturbée. Ainsi, des interactions flamme-acoustique ont été réalisées pour comprendre l'influence de la courbure sur les flammes d'ammoniac. Cela conclut ce travail, ouvrant la voie à de nouvelles directions dans le monde de la combustion de l'ammoniac.

Mots clés : ammoniac, vitesse de la flamme laminaire, épaisseur de la flamme, chimiluminescence, espèces excitées, interaction flamme-acoustique, étirement local

Study and analysis of premixed flame dynamics of zero carbon fuel – ammonia

Abstract :
In the quest for alternative fuels to mitigate crises like pollution, global warming, depletion of resources, etc, ammonia has emerged as one of the top contenders amongst other green fuels. The goal of this thesis is to provide experimental data and analyses that are useful both to the industry and the scientific community. This work has been divided into 3 parts to meet the set objectives. The first part is dedicated to providing laminar flame speeds, which is an important sizing parameter, at conditions that are encountered in combustors. This section also highlights the chemistry involved and various factors influencing it; explaining some unique behaviour like pressure independency. The second part is an attempt to understand the inner structure of ammonia flames. It is important to understand the response of different species to variations introduced into the parameters which may help enhance various desirable properties. The thickness of ammonia flame and its impact while calculating flame speeds have been pointed out. The effect of curvature on different excited species and the position of the heat release rate has been determined. The final part of this thesis is an extension of the second part. The concentration of some of the excited species is useful in accommodating it in any kinetic scheme and has been given here. It is known that turbulent flames help to improve certain desirable properties. However, turbulent flames are very complex and not easy to analyse. The most simple step would be to study a perturbed flame and so, tests on flame-acoustic interactions have been performed to understand the influence of curvature for ammonia flames. This study is concluded with insights paving paths to new directions in the world of ammonia combustion.

Keywords : ammonia, laminar flame speed, flame thickness, chemiluminescence, excited species, flame-acoustic interaction, local stretch

ICARE-CNRS, 1C Avenue de la recherche scientifque

LE SOMMAIRE

L'idée d'utiliser l'ammoniac comme combustible a reçu une attention particulière ces dernières années. En effet l'ammoniac est l'un des combustibles les plus étudiés par les chercheurs en combustion au cours des 5 ans écoulés. Mais comme toute nouvelle idée proposée, il y a toujours un débat entre les chercheurs ; certains se portant garants de l'idée en raison de son côté décarboné et de ses autres avantages, tandis que d'autres soulignent largement les inconvénients de l'utilisation de l'ammoniac. Formulé chimiquement sous le nom de NH_3, l'ammoniac est bien connu du grand public pour son utilisation comme réfrigérant et comme engrais. L'augmentation constante des émissions de carbone et l'épuisement rapide des combustibles fossiles suscitent des inquiétudes alarmantes et appellent à la recherche de combustibles verts alternatifs. Plusieurs tentatives sont faites pour réduire ces émissions nocives qui provoquent le réchauffement de la planète et le changement climatique. De nombreux pays se sont engagés à réduire leur empreinte carbone et à recourir à des sources d'énergie vertes. Ils ont également signé des conventions telles que le protocole de Kyoto et l'accord de Paris et ont participé activement à des sommets mondiaux. L'hydrogène est un excellent exemple de carburant décarbone qui a été largement accepté comme solution aux problèmes actuels. Toutefois, le stockage et le transport de l'hydrogène présentent toujours un risque en raison de sa nature explosive. Une autre solution proposée est l'utilisation de batteries électriques, même si l'impact environnemental et l'efficacité de ces batteries restent contestés. Les études sur la combustion métallique et les biocarburants sont toujours en cours. Le stockage de l'énergie provenant de sources d'énergie renouvelables est toujours un problème majeur. Les recherches sur l'ammoniac montrent qu'à l'exception de quelques obstacles, l'ammoniac en tant que carburant est a un avenir prometteur. Au fil des ans, son utilisation en tant que combustible a été viable avec des performances comparables à celles de ses homologues conventionnels. Si l'on compare les tendances de la recherche sur l'ammoniac, l'hydrogène et le méthane, on constate que l'ammoniac a suscité un grand intérêt au cours de la dernière décennie et qu'il devrait connaître une croissance exponentielle au cours de la prochaine décennie. Du point de vue de la recherche, il reste beaucoup de questions à résoudre pour comprendre le comportement des flammes d'ammoniac.

L'utilisation de l'ammoniac dans les moteurs à allumage commandé et les turbines à gaz est bien établie. Cependant, les données nécessaires au dimensionnement des moteurs dans les conditions rencontrées dans ces chambres de combustion font défaut. Le premier objectif de ce travail de thèse est de trouver des données sur la vitesse de la flamme dans ces conditions. En outre, on a constaté qu'il y avait peu d'études sur la structure interne de la flamme. Si l'on veut savoir comment améliorer le processus de combustion, il est important de comprendre les paramètres qui affectent la zone de réaction. Ainsi, le second objectif est de comprendre certaines propriétés de la flamme d'ammoniac. Il a été noté qu'il n'y a pas eu de tentative pour fournir la concentration de certaines espèces excitées. Une analyse qualitative et quantitative a été faite pour diverses de ces espèces afin de déterminer leurs concentrations . Il est connu que les systèmes industriels mettent en jeu des écoulements réactifs turbulents. Cependant, les flammes turbulentes sont extrêmement complexes par nature. La première étape, et la plus fondamentale, consiste à étudier une flamme laminaire perturbée. Bien que les flammes laminaires perturbées soient différentes des flammes turbulentes, elles peuvent donner un aperçu de la façon dont les flammes réagissent lorsqu'elles sont soumises à une perturbation turbulente. L'objectif final de cette thèse est étudier les interactions flamme-acoustique.

Pour répondre aux objectifs fixés, cette thèse a été divisée en 3 parties :

(i) Partie I : Vitesses de flammes laminaires à haute pression et température,

(ii) Partie II : Structure interne de la flamme prémélangée étirée et,

(iii) Partie III : Analyses chimiques et dynamiques de la flamme prémélangée.

La partie I est consacrée à l'obtention des vitesses de flamme et à l'évaluation des schémas cinétiques présents dans la littérature dans des conditions élevées pour des mélanges pauvres, quasi stœchiométriques et riches. L'objectif de la partie II est de comprendre les différentes propriétés réactives ainsi que la structure interne de la flamme prémélangée étirée à différents richesses. La partie III a deux aspects importants. Le premier aspect est de fournir analyses qualitatives et quantitatives de certaines des espèces excitées. Le second aspect est de comprendre l'effet de la perturbation sur la structure interne de la flamme à différents richesses. Chaque partie est divisée en chapitres et inclue une brève introduction et une conclusion. Cette brève introduction vise à fournir l'objectif de l'étude et l'essentiel de chaque chapitre et la conclusion donne un aperçu de l'étude. Cette thèse se termine enfin par un résumé concluant et une note de réflexion sur la portée future de ce projet.

Partie I : Vitesses de flammes laminaires à haute pression et haute température

Comme indiqué précédemment, on sait que l'utilisation de l'ammoniac dans les moteurs à allumage commandé et les turbines à gaz est favorable en raison de ses propriétés antidétonantes dues à son indice d'octane élevé. La pression rencontrée dans ces chambres de combustion est de l'ordre de 20 bar à faible charge et de 70-100 bar à pleine charge. La vitesse de propagation d'une flamme laminaire de prémélange est l'un des principaux paramètres de dimensionnement d'un moteur. Il y a un besoin de données de vitesse de flamme dans

des conditions élevées. L'objectif de cette partie est de fournir des données de vitesse de flamme pour des flammes d'oxy-ammoniac jusqu'à une pression de 30 bar et une température de 585 K et d'évaluer les schémas cinétiques récents disponible dans la littérature pour ces conditions.

Le **Chapitre 1** présente la littérature disponible pour l'évaluation de la vitesse de la flamme et du schéma cinétique. La plupart des expériences sont réalisées dans des conditions atmosphériques. Dans des conditions élevées, il n'y a pas suffisamment de données. On a également constaté que la technique la plus couranment utilisée pour réaliser les expériences était la chambre sphérique fermée. Les dernières données disponibles visent à combiner l'ammoniac avec d'autres combustibles non conventionnels comme le Dimethyl éther (DME), l'éthanol et le méthanol. Lors de l'analyse des différents schémas cinétiques, il a été constaté que Okafor [1] a donné les résultats les plus conformes pour les mélanges pauvres et que Klippenstein [2] et Zhang [3] ont donné les meilleurs résultats pour les mélanges riches en carburant. Konnov [4] et Mathieu [5] semblent surestimer et sous-estimer respectivement les vitesses de flamme par rapport aux données expérimentales [6]. Du point de vue des analyses de sensibilité [7], $H + O_2 \rightleftharpoons O + OH$ est la réaction la plus dominante, sa sensibilité à la vitesse de la flamme étant d'environ 0,5.

Le **Chapitre 2** se concentre sur la méthodologie utilisée pour atteindre cet objectif. Les expériences sont réalisées dans l'installation OPTIPRIME qui consiste en une chambre de combustion sphérique à volume constant avec une vue optique à 360 degrés. Ce large champ de visibilité permet de visualiser la flamme depuis son point d'allumage jusqu'à ce qu'elle atteigne la paroi. Cette chambre est placée à l'intérieur d'un four, ce qui permet d'effectuer des tests à une température initiale supérieure à la température ambiante. Cette chambre est équipée d'un thermocouple de type K et de 2 transducteurs de pression. Une caméra CMOS est utilisée pour enregistrer l'évolution du rayon de flamme. L'évolution de la pression et du rayon sont combinées pour évaluer la vitesse de la flamme. Un modèle de perte de chaleur est utilisé pour limiter les valeurs maximales de température et pression à considéré . Pour éviter les effets d'étirement qui affectent la vitesse de flamme, le front de flamme est considéré lorsque la pression dans la chambre atteint deux fois la pression initiale. Après avoir effectué une recherche bibliographique, 9 schémas cinétiques récents pour la combustion de l'ammoniac ont été choisis pour cette étude et sont présentés dans le Tableau 2.1. Des tests ont été réalisés pour un mélange ammoniac-oxygène à 3 richesses différentes : 0,8, 1,1 et 1,3 à une température initiale de 300 K. Pour les mélanges riches, la pression initiale était comprise entre 1 bar et 4 bar alors que pour le mélange pauvre, elle était à 1 bar et 2 bar. Le mélange comburant est composé à 30% d'oxygène et les 70 % restants constituent le diluant pour toutes les conditions. Le diluant est nécessaire car ces flammes sont assez instables par nature, les instabilités hydrodynamiques et thermo-diffusives étant favorisées dans ces conditions de température et de pression. Les conditions initiales utilisées sont représentées dans le Tableau 2.2.

Le **Chapitre 3** se concentre sur les vitesses de flamme et les analyses de sensibilité pour les différentes conditions d'essai afin de mettre en évidence les réactions prédominantes dans les différents schémas cinétiques. Pour toutes les conditions, les mécanismes de Nakamura [8] et Stagni [9] se situaient dans la gamme expérimentale. Des analyses de sensibilité ont été effectuées sur quelques mécanismes pour comprendre le comportement et mettre en évidence

les réactions clés. On a vu que la réaction la plus dominante, quel que soit le mécanisme et les conditions initiales, est $O_2 + H \rightleftharpoons O + OH$. Il est intéressant de noter que même si la vitesse de flamme prédite par Nakamura et Stagni est assez proche, les 10 réactions les plus prédominantes ne sont pas exactement les mêmes. Les deux réactions communes en dehors de la réaction dominante sont : $HNO + H \rightleftharpoons NO + H_2$ et $NH_2 + NO \rightleftharpoons NNH + OH$. De plus, d'après analyses de sensibilité, il a été constaté que la vitesse de la flamme n'est pas très sensible à la pression.

Le **Chapitre 4** se penche sur la propriété d'indépendance à la pression des flammes d'ammoniac. Une liste d'études de cas, dissociant la température et la pression, est réalisée pour trois mécanismes différents : Shrestha [10], Nakamura et Stagni pour trois richesses différentes. Ces études de cas permettent de comprendre les effets individuels sur la vitesse de la flamme pour différents mécanismes. Il a été constaté l'importance de la température sur la vitesse de flamme contrairement à la pression qui joue un rôle moindre, particulièrement à haute pression. Ces observations restent valables indépendamment de la richesse et du mécanisme choisi. L'impact maximum de la pression est remarqué entre 1-5 bar. Une autre étude de cas a été réalisée pour comprendre les effets de la pression et de la température lorsque le gaz diluant est changé. Des conclusions similaires ont été tirées. En outre, il a été constaté que les mécanismes de Shrestha étaient les moins affectés par le changement de la composition du gaz diluant. Enfin, les facteurs exponentiels α et β de l'équation 4.1 qui renseignent sur les dépendances à la température et à la pression,sont calculés. Il a été remarqué que la valeur de β était beaucoup plus faible que la plupart des combustibles. Ces facteurs exponentiels ont également été calculés pour les conditions d'essai données.

Pour conclure, des vitesses de flamme expérimentales pour la combustion de l'ammoniac jusqu'à une pression de 30 bars et une température de 585 K ont été fournies. L'évaluation des schémas cinétiques choisis dans les mêmes conditions d'essai a été effectuée. La propriété d'indépendance vis-à-vis de la pression des vitesses de flamme de l'ammoniac, en particulier à haute pression, suggère que l'ammoniac est un combustible idéal pour les moteurs à allumage commandé et les turbines à gaz, puisque les oscillations de pression auraient des effets moindre sur la vitesse de flamme. Enfin, à partir des données générées, une carte 3D de la vitesse de flamme en fonction de la pression et de la température utilisant une adaptation proposée par [11] été réalisée.

Partie II: Structure interne de la flamme prémélangée étirée

Dans la partie précédente, on a vu que les vitesses de flamme ammoniac/oxygène dans des conditions de température et pression élevées sont comparables à celles des combustibles classiques. Cependant, on sait que les vitesses de flamme ammoniac/air dans des conditions atmosphériques sont assez faibles. Il est important de connaître la structure interne de la flamme pour mieux comprendre le processus de combustion et, par conséquent, pour comprendre l'influence des différents paramètres afin d'améliorer ce processus. La partie II donne un aperçu de la structure des flammes étirées et prémélangées ammoniac/air aux conditions atmosphériques. Les paramètres étudiés sont l'influence

de la richesse et de la courbure sur l'épaisseur et la réactivité de la flamme. Cela a été réalisé expérimentalement en étudiant la signature par chimiluminescence de certaines espèces.

Le **Chapitre 5** donne une vue d'ensemble des études de la littérature sur la vitesse des flammes d'ammoniac dans l'air aux conditions atmosphériques et sur les différents diagnostics utilisés. Un résumé sur la signature par chimiluminescence des flammes d'ammoniac, sur les effets d'étirement, et sur la structure de la flamme est également fourni. Il existe plusieurs méthodes pour déterminer expérimentalement la vitesse de la flamme. La méthode la plus couramment utilisée est l'utilisation d'une chambre sphérique fermée, comme OPTIPRIME (cf. chapitre 2). Selon le but de l'expérience, la technique la plus appropriée est choisi pour réaliser l'expérience. Les techniques expérimentales trouvées dans la littérature pour la combustion de l'ammoniac sont : la chambre à pression constante, la chambre à volume constant, le brûleur Bunsen, le brûleur à flux thermique et la méthode du flux stagnant. Ici, les expériences sont réalisées sur le brûleur Bunsen avec des diagnostics comme la PIV (Particle image velocimetry) et la chimiluminescence. À partir des spectres d'émission des flammes d'ammoniac et d'air, NH* et NH_2* ont été reconnus comme des espèces intéressantes à étudier. La chimiluminescence de diverses espèces [12] a été utilisée pour étudier la formation de radicaux dans des réactions à haute température pour des mélanges NH_3/CH_4 dans des écoulements tourbillonnaires, à la fois expérimentalement et numériquement, et également pour déterminer l'emplacement du taux de dégagement de chaleur le plus élevé. À notre connaissance, aucune information sur le profil du taux de libération de chaleur (HRR :heat release rate) et les effets de courbure sur les espèces via la chimiluminescence n'est disponible pour les flammes ammoniac/air. Le travail effectué sur les effets d'étirement dans la flamme a montré qu'il est important de les connaître car ils modifient la surface de la flamme et, par conséquent, augmentent ou diminuent la réactivité selon que l'étirement est négatif ou positif. Enfin, l'étude de la structure de la flamme donne un aperçu des différentes espèces qui coexistent. Comprendre la position de ces espèces et la façon dont elles réagissent à une perturbation permet de connaître directement leur influence sur la réactivité. Il est donc important de comprendre la structure de la flamme pour améliorer les propriétés de la flamme et favoriser la combustion.

Le **Chapitre 6** est consacré à la description du dispositif expérimental. Ces expériences sont réalisées aux conditions atmosphériques sur un brûleur Bunsen. Une flamme pilote de méthane-air à la stœchiométrie a été utilisée pour stabiliser la flamme principale. Des tests ont été effectués pour s'assurer qu'il n'y avait pas d'effet direct de la flamme pilote sur les mesures calculées sur la flamme principale. De plus, la région d'intérêt était éloignée de la base de la flamme. Les pertes de chaleur vers le brûleur ne sont pas considérées pour la même raison. Des effets de rayonnement peuvent se produire dans les gaz brûlés à partir de la vapeur d'eau. Pour cette étude, ces effets ne sont pas considéres car la région d'intérêt est limitée à la partie amont de la zone de réaction qui est éloignée des gaz brûlés. La vitesse moyenne des gaz frais à la sortie du brûleur était comprise entre 0,18 et 0,2 m/s. Pour le montage de PIV, le DEHS (Diethyl-hexyl-sebacate) qui s'évapore à 525 K a été utilisé pour ensemencer les gaz frais avec des gouttelettes. Le dispositif de PIV consiste en une source laser dirigée et mise syr la flamme. La source lumineuse utilisée est un laser continu Coherent Verdi G20 de 532 nm. La puissance du laser est de 5 W. Le faisceau est

réfléchie sur le miroir à angle droit en traversant une lentille cylindrique puis une lentille sphérique de longueur focale f = 750 mm fournissant une nappe laser perpendiculaire à la flamme. Un diaphragme est utilisé pour contrôler la taille de cette nappe laser afin de s'assurer que seule la flamme est illuminée par le laser. Une caméra CMOS haute vitesse (PHANTOM V1611) est utilisée pour capturer les images et un code écrit en Python est utilisé pour suivre les particules et fournir une carte du champ de vitesse. La structure interne de la flamme a été déterminée par chimiluminescence. Les filtres utilisés pour NH* et NH_2* sont centrés sur les longueurs d'onde de 337 nm et 632 nm respectivement avec un diamètre de 50 mm et une largeur de bande passante de 10 nm. Ces filtres ont été achetés chez Edmund Optics. Le filtre est placé devant l'intensificateur IRO à haute vitesse qui est placé devant la caméra CMOS. L'intensificateur est utilisé pour avoir une sensibilité maximale et une bonne qualité d'image. Deux objectifs différents ont été utilisés : un objectif UV pour NH* et un objectif à spectre visible pour NH_2*. Enfin, pour étudier la structure de la flamme, des simulations Chemkin 1D ont été réalisées pour donner le profil de température, le profil HRR et la fraction molaire des espèces non excitées.

Le **Chapitre 7** met l'accent sur l'épaisseur de la flamme et explique pourquoi il est important de choisir la bonne isotherme pour calculer des paramètres tels que la vitesse de flamme. Une comparaison avec la littérature montre que la valeur de la vitesse de flamme change si la bonne isotherme n'est pas choisie. Les résultats concluent que les approximations de flamme mince ne sont pas valables pour le cas des flammes ammoniac-air.

Le **Chapitre 8** se concentre sur les effets de la courbure sur les espèces et la structure de la flamme. Deux courbures principales k1 et k2 sont introduites. k2 est la courbure dans la direction circonférentielle tandis que k1 est la courbure dans le plan. D'après la chimiluminescence de NH* et NH_2*, on constate que plus la flamme est riche, moins l'effet de courbure est important. Puisque le nombre de Lewis augmente avec la richesse et est proche de l'unité [13], l'effet de la courbure négative n'est pas bien prononcé à la pointe de la flamme, bien qu'un effet légèrement plus élevé soit attendu pour les flammes plus riches. Indépendamment de l'espèce excitée et de la richesse du mélange, il a été observé que l'épaisseur de l'espèce continue à augmenter et commence à diminuer à sommet de la flamme (courbature négative indiquée par k1). k2, par contre, augmente lorsqu'on se déplace de la base de la flamme vers la pointe de la flamme. Cela montre que l'effet de courbure moyenne est simplement considéré comme un changement d'épaisseur des espèces produites, et non directement comme la concentration des espèces dans une région donnée, puisque l'intensité moyenne reste la même. En effectuant une comparaison par espèce, on constate que NH_2* subit un effet de courbure moyen légèrement supérieur à celui de NH*. La flamme, à une hauteur d'environ 6 mm de sa base, a des coefficient de courbure faibles : k1 quasiment nul et k2 proche de -0. $2mm^{-1}$. A cette hauteur, la flamme peut donc être comparée à une flamme non étirée à propagation libre 1D. Des simulations Chemkin avec le schéma cinétique de Stagni ont été réalisées pour effectuer des comparaisons. La température, le HRR ainsi que la concentration des espèces non excitées correspondent à une gaussienne (à 95%) et sont tracés le long du domaine 1D. NH_2* est produit à une température plus basse que NH*. De plus, NH* et NH_2* sont assez proches de leurs espèces non excitées correspondantes. Un mécanisme de for-

mation des espèces excitées pourrait être incorporé dans n'importe lequel des schémas cinétiques. Le HRR maximum se produit entre NH* et NH_2* pour chacun des cas. Par conséquent, le produit de NH* et de NH_2* est un bon indicateur pour déterminer le HRR maximal de manière expérimentale. Il s'agit en effet d'un moyen vraiment efficace pour déterminer la position du HRR.

Partie III : Analyses chimiques et dynamiques de la flamme prémélangée

La deuxième partie s'est concentrée sur la structure interne d'une flamme sur un brûleur Bunsen en utilisant des diagnostics comme la chimiluminescence. Il a été constaté qu'aucune espèce excitée associée n'est prise en compte dans la cinétique chimique. Il est intéressant d'ajouter ces espèces surtout lorsque ces espèces peuvent être utilisées pour obtenir des informations directes sur la position du HRR comme vu dans la partie précédente. La première étape de la partie III consiste à aller plus loin en fournissant la concentration de certaines espèces excitées pour la même configuration, ce qui est nécessaire pour ajouter les espèces excitées dans les schémas cinétiques. Cette étape est particulièrement utile lors de l'exécution de simulations pour différentes géométries et configurations. Il est connu que la turbulence améliore la réactivité. Mais la turbulence est de nature très complexe et il est difficile de saisir tous les phénomènes lorsqu'ils sont couplés. Ainsi, une étape très rudimentaire consiste à comprendre une flamme laminaire perturbée. C'est dans cet esprit que les interactions flamme-acoustique sont étudiées. L'objectif de cette section est d'étudier l'influence de la courbure sur les espèces. En parcourant la littérature, aucun travail expérimental antérieur sur les interactions flamme-acoustique pour les flammes d'ammoniac n'a été trouvé.

Le **Chapitre 9** présente une brève revue de la littérature relative à l'analyse quantitative et qualitative de la chimiluminescence dans la combustion de l'ammoniac. Bien qu'il existe des études sur l'analyse qualitative, il n'y a pas d'études sur l'analyse quantitative de la combustion de l'ammoniac, ce qui fait du présent travail l'une des premières tentatives de quantifier les espèces excitées à partir de la chimiluminescence. En ce qui concerne les études sur les flammes perturbées, il existe une littérature abondante sur les écoulements tourbillonnaires et turbulents, mais il n'y a pratiquement aucun travail expérimental sur les flammes laminaires perturbées. Quelques simulations numériques ont été réalisées pour étudier les effets de la courbure sur les espèces. Le travail actuel est la première étude expérimentale faite sur les interactions flamme-acoustique pour la combustion d'ammoniac prémélangé.

Le **Chapitre 10** présente l'utilisation d'une caméra à faible vitesse (KURO sCMOS rétroéclairé) qui a une meilleur résolution spatiale et une meilleur résolution quantitative (bit par pixel). La caméra est plus sensible et l'intensificateur IRO peut donc être retiré. La qualité des images obtenues à partir de cette caméra est bien meilleure car le rapport signal/bruit est assez élevé. Une fois encore, le diagnostic d'intérêt reste la chimiluminescence. Trois espèces différentes sont étudiées: NH_2*, OH*, et NO*. Le montage utilisé pour l'interaction flamme-acoustique a également été décrit. Un haut-parleur est fixé à la base du brûleur et ce dernier est connecté à un amplificateur qui est, lui-même, connecté à un générateur d'ondes. Le générateur d'ondes est utilisé pour contrôler

la forme d'onde, l'amplitude et la fréquence. Seules les ondes sinusoïdales ont été utilisées. Pour cette étude, seul NH_2* est observé car cette espèce est un bon indicateur de la position du HRR. Pour les flammes dynamiques, un compromis entre l'obtention d'une image nette et une image de haute qualité doit être fait. Pour augmenter le rapport signal/bruit, le temps d'exposition de la caméra est augmenté mais lorsqu'il s'agit de capturer des flammes dynamiques, il y a une limite pour éviter d'obtenir des images floues. Des tests ont été effectués pour des flammes stationnaires avec le filtre NH_2* et sans le filtre en utilisant toujours l'objectif visible range (VR). D'après les spectres d'émission des flammes d'ammoniac/air, on sait que la région visible est constituée d'une large bande de pics NH_2*. Par conséquent, sans utiliser le filtre NH_2* et en utilisant uniquement l'objectif VR, NH_2* est toujours visualisé.

Le **Chapitre 11** est consacré à la réalisation d'une analyse quantitative et qualitative de certaines des espèces importantes dans les flammes d'ammoniac. Aucune tentative antérieure n'a été faite pour déterminer la concentration de NH_2* et de OH* à partir de la chimiluminescence dans les flammes d'ammoniac. L'effet d'extinction n'a pas été pris en compte et les concentrations fournies sont pour des flammes étirées. Dans la partie précédente, on a vu que ces effets d'étirement sont assez faibles. Les concentrations ont été déterminées dans le but d'aider à prendre en compte les espèces excitées dans n'importe quel schéma cinétique pour les flammes d'ammoniac. Pour les flammes d'ammoniac, ces espèces excitées doivent encore être ajoutées. L'ajout d'espèces comme le NH_2* peut être important car son suivi dans les simulations numériques peut fournir des informations directes sur le HRR. Ce chapitre détaille le processus de détermination de la concentration des espèces. Un processus en quatre étapes impliquant la calibration de l'optique, la calibration de la lampe tungstène, la tentative de corréler l'intensité vue par la caméra à la concentration de l'espèce et enfin l'adaptation de la méthode au dispositif expérimental donné a été méticuleusement décrit ici. Enfin, une analyse qualitative de NO* a également été proposée.

Le **Chapitre 12** traite des études sur les interactions flamme-acoustique des flammes d'ammoniac-air prémélangées. Il s'agit ici de comprendre l'influence sur la réactivité de l'effet de courbure généré par les perturbations acoustiques. Dans un premier temps, le nombre de Strouhal critique a été défini pour la configuration donnée. D'après [14], on sait que pour avoir un écoulement dominé par l'acoustique, le nombre de Strouhal de l'écoulement doit être supérieur au nombre de Strouhal critique. Sur cette base, une fréquence a été choisie pour les études ultérieures. En étudiant la réponse de la flamme au changement d'amplitude et de fréquence, il a été remarqué que lorsque l'amplitude augmente, l'effet d'élongation et de compression sur la flamme est plus fort et que lorsque la fréquence augmente, différents modes peuvent être obtenus jusqu'à une certaine valeur de fréquence au-delà de laquelle toute augmentation de fréquence ne change pas la réponse de la flamme. Une fréquence de forçage de 40 Hz et une amplitude de 0,5 V pour des richesses allant de 1 à 1,4 sont étudiées ici. Initialement, la courbure moyenne a été obtenue pour quantifier l'effet de courbure mais il a été constaté que la réponse de la flamme était trop complexe et donc, les deux courbures principales k1 et k2 sont utilisées. Quatre paramètres différents : k1, k2, l'épaisseur le long de la normale au front, et l'intensité maximale le long de la normale au front ont tous été tracés en fonction des contours de la flamme. La modification de l'épaisseur du front est un

effet indirect de la modification de la réactivité. Pour comprendre la réponse complète de la réactivité, l'intensité intégrée le long de la normale doit être surveillée. Une fois de plus, le tracé de la courbure en fonction de l'intensité intégrée était trop complexe et ce paramètre a donc été divisé en deux paramètres de base : l'épaisseur et l'intensité maximale. Après un examen attentif, on a constaté que l'effet de k1 et de l'épaisseur le long du contour semblait être corrélé, mais l'intensité maximale et k2, n'ont montré aucune correlation. En évaluant chaque cas, on a vu que l'intensité de la flamme diminuait de la base à la pointe de la flamme, quelle que soit la valeur de la courbure. Cependant, la réduction de l'intensité à la pointe par rapport à la base de la flamme était plus apparente pour Le >1. Il semble que les vitesses de convection-diffusion jouent un rôle majeur. En calculant le nombre de Damköhler, Da, on a vu que cette valeur était légèrement supérieure à 1, ce qui indique que les deux échelles de temps sont comparables. La vitesse de convection était environ 25 fois supérieure à la vitesse de diffusion de l'ammoniac dans l'air aux conditions ambiantes. Ceci indique que ce n'est pas l'ammoniac qui diffuse directement sur les côtés des flammes mais l'ammoniac lui-même qui se décompose en espèces plus légères qui diffusent plus rapidement que le flux convectif. La diffusion préférentielle de H_2 et d'autres espèces vers les côtés joue un rôle majeur dans l'amélioration de la réactivité locale.

En conclusion, la combustion d'ammoniac a suscité un intérêt dans le monde entier en tant que substitut aux combustibles conventionnels. Elle a intrigué la communauté scientifique au cours des dernières années, car de nombreux phénomènes liés à la combustion de l'ammoniac n'ont pas été entièrement compris. Le but de cette thèse est d'identifier quelques-unes de ces inconnues et de tenter de comprendre le comportement de ces flammes. L'objectif principal de cette étude est d'étudier les propriétés chimiques des flammes laminaires d'ammoniac pur prémélangé. Les vitesses de flamme pour différentes conditions initiales, la structure interne de la flamme, le comportement des flammes laminaires perturbées et la réponse de la flamme aux changements de paramètres pour chacun des cas ont été minutieusement étudiés. La majeure partie de ce travail est de nature expérimentale et a été complétée par des études numériques 1D utilisant Chemkin-Pro. Deux montages expérimentaux différents : une chambre de combustion à volume constant et un brûleur Bunsen ont été utilisés. L'un des principaux objectifs était de fournir des données expérimentales qui peuvent être utilisées pour améliorer les schémas cinétiques existants dans la combustion de l'ammoniac, qui sont également utilisés dans les simulations numériques. Cette thèse a été divisée en trois parties pour évaluer et atteindre les objectifs fixés. Chaque partie a apporté de nouvelles connaissances sur la combustion de l'ammoniac. Il y a encore beaucoup de travail à faire pour combler les lacunes de la combustion de l'ammoniac. Des simulations numériques utilisant LES ou DNS peuvent être réalisées dans les mêmes conditions expérimentales pour compléter les données expérimentales. L'utilisation de ces données expérimentales pour améliorer ou mettre à jour les schémas cinétiques existants est intéressante car les expériences réalisées ici sont dans des conditions uniques par rapport aux données de la littérature existante. Comme mentionné précédemment, les concentrations des espèces excitées peuvent être utilisées pour intégrer ces espèces dans les schémas cinétiques, car elles peuvent fournir des informations sur certains paramètres d'intérêt. Pour les études sur les interactions flamme-acoustique, trouver les vitesses de déplacement locales

et les vitesses de consommation et l'impact de la courbure sur celles-ci est très important. De même, en ciblant les flux avec Da<1, il peut être intéressant de voir si la courbure a un effet sur l'intensité. Avec un peu plus de recherche et de technologie pour surmonter certaines des autres limitations, l'ammoniac peut être déployé comme l'une des principales sources d'énergie de demain. En effet, l'ammoniac présente le potentiel nécessaire pour résoudre la crise énergétique mondiale.

ACKNOWLEGEMENTS

They say that life is like a roller coaster. The will to stand up, fight and not give up after every failure is the very first step to progress in life. With a hardship, comes success. Success borne as a fruit of hard work and patience is the most cherished one. Those people who stick around through thick and thin are invaluable. And, I have had the pleasure of being around some amazing people who have motivated me and cheered me throughout my journey as a Ph.D. student.

I would like to start off by thanking CNRS and Université d'Orléans for giving me this opportunity. Next, I would like to thank Région Centre-Val de Loire for funding my work. I would also like to thank the director of the lab- Dr. Philippe Dagaut for everything he has done. No words can describe how grateful I am to the director of my thesis - Prof. Fabien Halter who believed in my abilities and encouraged me to take my decisions. I am indebted to you for all the wisdom parted and support you have provided me not just for those related to my thesis but also for my career. Next in line is the co-director of my thesis - Dr. Christian Chauveau who supported me at every step and stood by me at all times. Thank you for guiding me, giving me valuable pieces of advice and encouraging me. I would equally like to thank Prof. Guillaume Dayma who has always helped me and has made time for me and guided me throughout my work. This thesis was done during the pandemic- COVID-19 and surely enough, there were a lot of difficulties faced during this period. The undeterred support and help I received from the three of you were very vital for me to complete this work within the allotted time. I am deeply grateful to the three of you for celebrating my success even if they weren't always big and for motivating me through the lows.

I thank all the members of my jury for accepting to be a part of my defence. I would like to particularly thank the examinators- Prof. Julien Sotton and Dr. Thibault Guiberti for taking their time to evaluate and provide valuable comments and different insights.

I would like to express my gratitude to the Admin, IT, workshop, and all the other departments for offering to help me whenever required. I would also like to thank the Ecole Doctorale and the members of CSI for helping me navigate through the process. I also would like to take this opportunity to

thank Dr. Fabien Thiesset who was a member of the jury from CORIA, Rouen, Dr. Pierre Brequigny and Prof. Christine Rouselle who was also the president of the jury from PRISME, Orléans for all advices and insights on my work. I would equally like to thank Dr. Olivier Mathieu who was also a member of the jury with whom I had the pleasure of having fruitful interactions on chemical kinetics. I thank Dr. Ivan Fedouin for getting me started with ANSYS.

The people in ICARE have been exceptionally generous and friendly. I would like to profusely thank Dr. Viviana Lago, Dr. Max McGillen, Dr. Stephane Bostyn, Dr. Veronica Belandria and Dr. Mahmoud Idir for the friendly chats. I would also like to thank Prof. Guillaume Legros and Dr. Toufik Boushaki for their help. To the Team OC - during these three years, the entire team including the interns and the permanent staff along with the Ph.D. students and the postdocs have always considered me one as their own. I will always be grateful to this entire team. I have had the pleasure to spend wonderful moments with all of you. Thank you Dr. Nabiha Chaumeix for the interesting conversations and for the fun times with the team.

When I first came to ICARE, I was struggling a lot with French and with being new to the place. I would like to thank Dr. Maxence Laillau, Dr. Nicolas Rembaut, Dr. Hajar Zaidaoui, and Hugo Chouraqui for clearing my french doubts and for the interesting chats. I had the pleasure of meeting some amazing people like Dr. Hajar El Othmani, Lydia Boualem, and Ahlem Ghaabi with whom I had some fun times. I am lucky to have met these colleagues who finally ended up being good friends to me: Dr. Anthony Roque, Dr. Sharath Nagaraju, Dr. Outmane Mghanen, Dr. Miles Burnett, Laura Vastier, Jean-Noel Semaan and Ronan Pelé. You all have always been there for me. Cheers to all the fun we have ever had. I don't know what would I have done if I hadn't meet these three people: Dr. Alaa Hamadi, Leticia Piton and, Fabian Cano. They have become family and have shown me compassion like I have always been a part of them. It is amazing how we come from different parts of the world, cross paths in the pursuit of our dreams and end up sharing a bond as we do. It was fun to travel and discover many unknown places and try out new adventures together.

My team CT have always been very supportive and has always helped me with everything I have ever needed. I am glad to have had some great conversations and some help from all the interns we have seen in the last three years, Dr. Marco Di Lorenzo, Deniz Kaya, Valentin Glasziou, Antoine Mouze-Mornettas, and Samuel Jeanjean. I am happy to have spent some time and learn a lot from Deniz Kaya. I am also glad to have had fun conversations with Valentin Glasziou. Antoine Mouze-Mornettas - Thanks for all that fun and crazy conversations and for placing bets on things others wouldn't. The bets are still on! I do not think words would do justice to what Samuel Jeanjean has done for me. Samuel and I started our thesis together and shared our office. We have become very close friends over the years and have had crazy conversations, played silly games and pranked each other incessantly. You have always helped me whenever I needed it, stood by me when I needed support, taught me French, introduced me to French culture and whatnot! You have made work fun and you have played an important role to achieve my goal. I am sure my path would have been completely different if not for you. And so, I am thankful to have met you.

And last but not the least, I would like to thank all my friends who have

rendered support, my entire family and my parents who have played a huge role in helping me to chase my dreams. My parents have always stood by all my decisions and have believed in me even when I haven't. None of this would have been possible if not for them. I believe that this entire journey was not only just about achieving the target but also, was about meeting new people, learning new things, maintaining a work-life balance and finally with a huge focus on holistic development. I have acquired skills and learnt a lot about myself through this process.

Enfin, je me dois d'écrire quelques mots en français pour vous faire savoir que vos efforts n'ont pas été vains. Merci à tous ceux qui ont participé à cette expérience!

CONTENTS

Nomenclature **xxix**

General Introduction **1**

I Laminar flame speeds at high pressure and temperature **5**

Introduction **7**

1 Chapter 1 **9**

Chapter 1 **9**
1.1 Literature review on experimental flame speed data in ammonia combustion . . . 9
1.2 Literature review on kinetic schemes in ammonia combustion . 10

2 Chapter 2 **13**

Chapter 2 **13**
2.1 Methodology . . . 13
2.1.1 Experimental set-up description . . . 14
2.1.2 Radius and pressure evolution . . . 14
2.1.3 Heat loss model . . . 17
2.1.4 Flame speed evaluation . . . 18
2.2 Chemical kinetic schemes . . . 19
2.3 Test conditions . . . 19

3 Chapter 3 **23**

Chapter 3 **23**
3.1 Experimental and numerical flame speeds . . . 23
3.2 Sensitivity analyses . . . 26

4 Chapter 4 **31**

Chapter 4 **31**
4.1 Isotherms and isobars . . . 31
4.1.1 Temperature and pressure effects . . . 31
4.1.2 Bath gases effects . . . 33
4.1.3 Alpha and beta . . . 34
4.2 Alpha and beta values for the experiment and numerical flame speeds . . . 35

Conclusion **37**

II Inner structure of a stretched premixed flame **39**

Introduction **41**

5 Chapter 5 **43**

Chapter 5 **43**
5.1 Experiments and optical diagnostics for flame speeds in ammonia combustion . . . 43
5.2 Chemiluminescence signature of ammonia flames . . . 44
5.3 Studies of stretch effects in ammonia flames . . . 45
5.4 Literature on ammonia flame structure . . . 45

6 Chapter 6 **47**

Chapter 6 **47**
6.1 The experimental set-up . . . 47
6.1.1 The PIV set-up . . . 48
6.1.2 The chemiluminescence set-up . . . 50
6.2 1D simulation . . . 52

7 Chapter 7 **53**

Chapter 7 **53**
7.1 Flame thickness . . . 53
7.2 Flame speed determination . . . 54

8 Chapter 8 **57**

Chapter 8 **57**
8.1 Curvature effects on the species . . . 57
8.2 Flame structure . . . 61

Conclusion **65**

III Chemical and dynamical analyses of a premixed flame **67**

Introduction **69**

9 Chapter 9 **71**

Chapter 9 **71**
9.1 Quantitative and qualitative analysis of chemiluminescence of ammonia flames . . . 71
9.2 Perturbed laminar ammonia flames . . . 72

10 Chapter 10 **73**

Chapter 10 **73**
10.1 The chemiluminescence set-up . . . 73
10.2 The flame-acoustic interaction set-up . . . 74

11 Chapter 11 **77**

Chapter 11 **77**
11.1 Step 1: Optics calibration 77
11.2 Step 2: Tungsten lamp calibration 80
11.3 Step 3: Correlation between concentration and intensity of the species 81
11.4 Step 4: Adapting the given irradiation values to the experiment set-up 82
11.5 Quantitative and qualitative analyses of species 82

12 Chapter 12 **87**

Chapter 12 **87**
12.1 Flame feedback due to acoustic perturbation 87
12.2 Curvature effects on the reactivity 89
12.2.1 Phi = 1.0 90
12.2.2 Phi = 1.1 91
12.2.3 Phi = 1.2 92
12.2.4 Phi = 1.3 93
12.2.5 Phi = 1.4 94

Conclusion **97**

General Conclusion **99**

Communications **103**

A Laminar flame speeds and sensitivity analyses **107**
A.1 Flame speed data for different test conditions 107
A.2 Sensitivity analyses for different test conditions 113
A.3 Sensitivity analysis at isothermal and isobaric conditions for Stagni 115

B Inner structure of stretched premixed flame **117**
B.1 NH_2* 117
B.2 NH* 118

C Chemical and dynamical analyses of a premixed flame **123**

Bibliography **129**

LIST OF FIGURES

1 Comparison of the trend for ammonia (blue), methane (orange), and hydrogen (grey) for almost two centuries. The number of publications is represented in the logarithmic scale 3

2.1 Sketch of the spherical combustion chamber - OPTIPRIME (left) and the furnace (right) [15]. 15

2.2 Time-based evolution of flame radius as the flame front propagates from its ignition to the walls. The mixture used here is methane-air at φ=1.3, p0=1 bar and T0=300K [16]. 15

2.3 Pressure and radius evolution with regions of stretch effects and heat losses (regions where the data cannot be retrieved) and isochoric conditions (region for which data is presented here) [17]. 16

3.1 Laminar flame speeds at p_0=4 bar, T_0=302.3K, φ = 1.3, 21% Ar and 49% He.The experimental flame speeds have been thickened in yellow to account for the uncertainties incurred. The y-axis represents the flame speed whereas the x-axis is split as temperature and pressure. This is done as the flame speed is a function of both pressure and temperature which evolves isotropically during the combustion process. The orange colour represents Klippenstein [2], violet represents Zhang (2017) [3], blue represents Dagaut [18], brown represents Otomo [19], pink represents Mathieu [5], cyan represents Modified Okafor [1], green represents Shrestha [10], red represents Stagni [9] and black represents Nakamura [8] 24

3.2 Laminar flame speeds at p_0=1 bar, T_0=296.8K, φ = 1.3, 49% Ar and 21% He 25

3.3 Laminar flame speeds at p_0=1 bar, T_0=296.2K, φ = 0.8, 49% Ar and 21% He 25

3.4 Comparison of specific rate constant, k of $NH_3 + NH \rightleftharpoons NH_2 + H_2$ over inverse of temperature for Nakamura (predicts flame speed within the experimental range) and Klippenstein (overpredicts the flame speed) 27

3.5 Sensitivity analyses at p_0=1 bar, φ = 0.8, 49% Ar and 21% He with the minimum pressure at 1 bar (dark blue) and the maximum at 8 bar (light blue) 28

3.6 Sensitivity analyses at p_0=1 bar, φ = 1.1, 49% Ar and 21% He with the minimum pressure at 1 bar (dark blue) and the maximum at 8 bar (light blue) 28

3.7 Sensitivity analyses at p_0=3 bar, φ = 1.1, 21% Ar and 49% He with the minimum pressure at 3 bar (dark blue) and the maximum at 24 bar (light blue) 28

3.8 Sensitivity analyses at p_0=4 bar, φ = 1.1, 70% He with the minimum pressure at 4 bar (dark blue) and the maximum at 36 bar (light blue) 29

3.9 Sensitivity analyses at p_0=2 bar, φ = 1.3, 21% Ar and 49% He with the minimum pressure at 2 bar (dark blue) and the maximum at 15 bar (light blue) 29

3.10 Sensitivity analyses at p_0=4 bar, φ = 1.3, 70% He with the minimum pressure at 4 bar (dark blue) and the maximum at 36 bar (light blue) 29

4.1 Comparison study of Nakamura, Stagni and Shrestha for φ = 0.8, 1.1 and 1.3 at a diluent mixture of 49% Ar and 21% He with isothermal plots at T=300 K and isobaric plots at p=1 bar, circles represent φ = 0.8, squares represent φ = 1.1 and triangles represent φ = 1.3 whereas the colours green, black and red represent the mechanisms of Shrestha, Nakamura and Stagni respectively. 32

4.2 Comparison study of Nakamura, Stagni and Shrestha for φ = 0.8, 1.1 and 1.3 at a diluent mixture of 49% Ar and 21% He with isothermal plots at T=500 K and isobaric plots at p=3 bar, circles represent φ = 0.8, squares represent φ = 1.1 and triangles represent φ = 1.3 whereas the colours green, black and red represent the mechanisms of Shrestha, Nakamura and Stagni respectively. 32

4.3 Comparison study of Nakamura, Stagni and Shrestha for φ = 1.1 for different bath gases compositions, circles represent 70% He with isothermal plots at T=300 K and isobaric plots at p=1 bar, crosses represent 49% He and 21% Ar and diamonds represent 21% He and 49% Ar whereas the colours green, black and red represent the mechanisms of Shrestha, Nakamura and Stagni respectively. 33

4.4 Comparison study of Nakamura, Stagni and Shrestha for φ = 1.1 for different bath gases compositions, circles represent 70% He with isothermal plots at T=500 K and isobaric plots at p=3 bar, crosses represent 49% He and 21% Ar and diamonds represent 21% He and 49% Ar whereas the colours green, black and red represent the mechanisms of Shrestha, Nakamura and Stagni respectively. 33

4.5 Beta trends from isotherms at T=500 K calculated using p_0=1 bar, T_0= 500 K and the corresponding flame speed depending on the equivalence ratio and the diluent mixture. φ=0.8, 21% He 49% Ar is represented by dash-dot, φ=1.3, 21% He 49% Ar by a dash, φ=1.1, 21% He 49% Ar by round dot, φ=1.1, 49% He 21% Ar by solid and φ=1.1, 70% He by long dash-dot-dot and the colours black, red and green represent Nakamura, Stagni and Shrestha respectively. 34

4.6 Experimental flame speeds of $NH_3/O_2/He/Ar$ mixtures at ϕ = 1.1, T_0 = 300 K, p_0 = 1 (blue), 2 (red), and 3 bar (green). . . 38

5.1 Different experimental techniques used to study flames along with the pressure and temperature range. 44

6.1 Sketch of the Bunsen burner set-up. 47

6.2 Images of buoyancy-driven flame flickering before and after using the chimney. 49

6.3 Schematic diagram of the experimental set-up along with the PIV set-up. CL: cylindrical lens, SL: spherical lens, DM: dichroic mirror, RM: rotameter, MF: mass flowmeter 50

6.4 Emission spectra for ammonia/air flames at stoichiometry identifying important species. The intensity has not been calibrated. The background illumination and the pilot flame emissions have been subtracted. The emission peaks are not calibrated. 51

6.5 Schematic diagram of the experimental set-up for the chemiluminescence study. 51

7.1 Definition of flame thickness. 53

7.2 Ammonia-air flame at φ = 1.1 with PIV depicting the thick flame. The inner cone and the outer cone represent the fresh gas surface and the outer flame surface respectively. The camera used to capture this image is NIKON D850 and the exposure time has been set to 250 ms. The x and y axes have been normalized over the radius of the burner axes. 54

7.3 Comparison of ammonia-air laminar flame speed at atmospheric conditions available in the literature for different φ . OC (black square) and IC (black circle) represent the flame speed at the outer cone and inner cone and Sd represented by a black diamond is the displacement flame speed. 55

8.1 Representation of the principal curvatures k1 and k2 in the flame contour. k1 is along the contour and k2 is along the circumferential direction. Negative curvature is defined for a concave flame in the direction of the burnt gas and a positive curvature is defined for a convex flame in the direction of the burnt gas. . . . 57

8.2 NH_2* and NH* signal in an atmospheric NH_3/air flame at φ = 1.4, (a) Abel inversion transformed image of NH_2*, (b) Abel inversion transformed image of NH* with the colour bar representing the pixel intensity, (c) The thickness of the species (NH_2* in black and NH* in violet) evaluated in the direction of the normal of the front vs. normalized position, (d) k1 (blue) and k2 (red) of NH_2* vs. normalized position. 59
8.3 Chemiluminescence images of NH* at (a) φ=0.9, (b) φ=1.1, (c) φ=1.3, and NH_2* at (d) φ=1, (e) φ=1.2, (f) φ=1.4. The exposure time of these images is not the same. 60
8.4 Results obtained from the experiments 61
8.5 Results obtained from the simulations 62
8.6 Flame structure at (a) φ=0.9, (b) φ=1.1, (c) φ=1.4. Temperature (solid black line) and the normalized HRR (dashed black line) are plotted on the left and the right y-axis respectively. The green line represents the fresh gas isotherm. The distance along the x-axis represents the 1D domain. Each of the species has been thickened to a width corresponding to the standard deviation of the gaussian-fit curve resulting in overlapping of the species. For easy visualization, each of the species has been plotted as a quarter bar in order to minimize the overlapping between species which otherwise would have resulted in difficulty to understand the figure. 63

10.1 Schematic diagram of the chemiluminescence set-up. 73
10.2 Schematic diagram of the chemiluminescence set-up. 74
10.3 Raw images of the flame to note the differences between using a NH_2* filter and not. 75

11.1 On comparing the normalized intensities along the centre of the images captured, it can be seen that by using the filter, the incoming intensity is reduced by less than 2%. The ROI is in betweeen 0.1 and 0.8 on the x-axis and is marked in orange. . . 78
11.2 Intensity vs potentiometer of LED lamp at an exposure time of 1ms with the NH_2* filter mounted on the camera. 79
11.3 Intensity vs exposure time of camera with the potentiometer of the lamp set at k=6 with the NH_2* filter mounted on the camera. 79
11.4 Transmission of the neutral desnity filters as a function of wavelength. 80
11.5 Intensity vs exposure time of camera with the ND filters and NH_2* filter. 81
11.6 Concentration of NH_2* for φ = 0.9-1.4 with the colour bar representing the concentration in mol/m^3. 83
11.7 Concentration of OH* for φ = 0.9-1.4 with the colour bar representing the concentration in mol/m^3. 84
11.8 Qualitative analysis on NO* for φ = 0.9-1.4. 85

12.1 The effect of amplitude on flames creating pockets of fresh gases for the same frequency (30 Hz) and equivalence ratio (1.1). . . 88
12.2 FAI for phi=1, A=0.5 V and f=40 Hz 90

12.3 FAI for phi=1.1, A=0.5 V and f=40 Hz 91
12.4 FAI for phi=1.2, A=0.5 V and f=40 Hz 92
12.5 FAI for phi=1.3, A=0.5 V and f=40 Hz 93
12.6 FAI for phi=1.4, A=0.5 V and f=40 Hz 94
12.7 Flame response at different instants at φ =1.1, A=0.5 V, f=40 Hz. 95

A.1 Laminar flame speeds at p_0=2 bar, φ = 0.8, 49% Ar and 21% He 107
A.2 Laminar flame speeds at p_0=1 bar, φ = 1.1, 49% Ar and 21% He 108
A.3 Laminar flame speeds at p_0=2 bar, φ = 1.1, 49% Ar and 21% He 108
A.4 Laminar flame speeds at p_0=2 bar, φ = 1.3, 49% Ar and 21% He 109
A.5 Laminar flame speeds at p_0=1 bar, φ = 1.1, 49% He and 21% Ar 109
A.6 Laminar flame speeds at p_0=2 bar, φ = 1.1, 49% He and 21% Ar 110
A.7 Laminar flame speeds at p_0=3 bar, φ = 1.1, 49% He and 21% Ar 110
A.8 Laminar flame speeds at p_0=2 bar, φ = 1.3, 49% He and 21% Ar 111
A.9 Laminar flame speeds at p_0=4 bar, φ = 1.3, 49% He and 21% Ar 111
A.10 Laminar flame speeds at p_0=4 bar, φ = 1.1, 70% He 112
A.11 Laminar flame speeds at p_0=4 bar, φ = 1.3, 70% He 112
A.12 Sensitivity analyses at p_0=2 bar, φ = 0.8, 49% Ar and 21% He 113
A.13 Sensitivity analyses at p_0=2 bar, φ = 1.1, 49% Ar and 21% He 113
A.14 Sensitivity analyses at p_0=1 bar, φ = 1.3, 49% Ar and 21% He 113
A.15 Sensitivity analyses at p_0=2 bar, φ = 1.3, 49% Ar and 21% He 114
A.16 Sensitivity analyses at p_0=1 bar, φ = 1.1, 49% He and 21% Ar 114
A.17 Sensitivity analyses at p_0=2 bar, φ = 1.1, 49% He and 21% Ar 114
A.18 Sensitivity analyses at p_0=3 bar, φ = 1.3, 49% He and 21% Ar 115
A.19 Sensitivity analyses at p_0=3 bar, φ = 1.3, 49% He and 21% Ar 115
A.20 Sensitivity analyses for isotherms at T=300 K over a pressure range of 1-20 bar for φ = 1.3, diluent mixture of 21% He and 49% Ar indicating that the dominant reaction is O2+H<=>O+OH and the recombination reaction of ammonia is relatively not sensitive. 116
A.21 Sensitivity analyses for isobars at p= 3 bar over a temperature range of 300-700 K for φ = 1.3, diluent mixture of 21% He and 49% Ar indicating that the dominant reaction is $O_2{}^+H$ and the recombination reaction of ammonia is relatively not sensitive although the magnitude of sensitivity to the flame speed is not the same for isobaric and isothermal cases. 116

B.1 Chemiluminescence images of NH_2* at φ = (a) 0.9, (b) 1, (c) 1.1, (d) 1.2, (e) 1.3, (f) 1.4. 117
B.2 Abel inversion transformed images of NH_2* at φ = (a) 0.9, (b) 1, (c) 1.1, (d) 1.2, (e) 1.3, (f) 1.4 depicting the positive curvature at the base of the flame for weak and stoichiometric conditions and the enhanced reactivity at the tip of the flame for φ = 1.1 and 1.2. The x and y axis represent the pixel and the color bar indicates the intensity of the pixel. 118
B.3 k1 and k2 at φ = 0.9. 119
B.4 k1 and k2 at φ = 1.1. 119
B.5 Chemiluminescence images of NH* at φ = (a) 0.9, (b) 1, (c) 1.1, (d) 1.2, (e) 1.3, (f) 1.4. 120

B.6 Abel inversion transformed images of NH* at φ = (a) 0.9, (b) 1, (c) 1.1, (d) 1.2, (e) 1.3, (f) 1.4 depicting the positive curvature at the base of the flame for weak and stoichiometric conditions and the enhanced reactivity at the tip of the flame for φ= 1.1 and 1.2 with strong reactivity near the burner for all the cases. The x and y axis represent the pixel and the color bar indicates the intensity of the pixel. 120
B.7 k1 and k2 at φ = 0.9. 121
B.8 k1 and k2 at φ = 1.1. 121
B.9 k1 and k2 at φ = 1.4. 122

C.1 Image captured at an exposure time of 1 ms with the ROI. . . 123
C.2 Image captured at an exposure time of 1 ms, potentiometer of LED lamp set at k=6 with the filter. 124
C.3 Image captured at an exposure time of 1 ms, potentiometer of LED lamp set at k=6 without the filter. 124
C.4 Thickness, maximum intensity, k1 and k2 as a function of contour at φ=1.0 125
C.5 Thickness, maximum intensity, k1 and k2 as a function of contour at φ=1.1 126
C.6 Thickness, maximum intensity, k1 and k2 as a function of contour at φ=1.2 126
C.7 Thickness, maximum intensity, k1 and k2 as a function of contour at φ=1.3 127
C.8 Thickness, maximum intensity, k1 and k2 as a function of contour at φ=1.4 128

LIST OF TABLES

1.1 Experimental literature available on ammonia combustion . . . 12

2.1 Chemical kinetic schemes used in this study 20
2.2 Initial conditions for the test cases along with the adiabatic flame temperature (AFT) 21

3.1 Initial pressure and equivalence ratio with the range of pressure and temperature for which the flame speed has been measured. The initial temperature, T_0, was maintained at 300K 24

12.1 Strouhal numbers for different flow conditions 88

NOMENCLATURE

Symbols

φ	Equivalence ratio
R_f	Flame radius
R_0	Inner chamber radius
x	Burnt gas mass fraction
p_0	Initial pressure
p	Pressure in chamber
γ_u	Heat capacity ratio of unburnt gases
m	Total mass
m_b	Burnt gas mass
p_e	Theoretical end pressure
T_0	Initial temperature
δ_{ph}	Thickness of preheating zone
δ_f	Thickness of reaction zone
A	ratio of preheating zone to reaction zone
$T_{ignition}$	Ignition temperature
k	Specific rate constant
S_u	Laminar flame speed of unburnt gases
T_u	Temperature of unburnt gases
p_u	Pressure of unburnt gases
${S_u}^0$	Initial laminar flame speed of unburnt gases
${T_u}^0$	Initial temperature of unburnt gases
${p_u}^0$	Initial pressure of unburnt gases
α_u	Temperature exponential factor
β_u	Pressure exponential factor

S_L	Laminar flame speed
δ	Flame thickness
S_d	Displacement speed
Ma	Markstein number
A_b	Exit area of the burner
U_{fg}	Fresh gas velocity at the burner exit
ρ_{fg}	Fresh gas density
A_u	Area of the unburnt gas surface
u	Fluid velocity
w	Absolute flame speed in a fixed laboratory frame
n	flame normal vector oriented towards the fresh gases
k1	Curvature along the flame contour
k2	Circumferential curvature
K_T	Strain rate
K_C	Curvature effect
K_m	Mean curvature
r	Radial direction in cylindrcial coordiante system
h	Streamwise direction in cylindrcial coordiante system
s	Curvilinear coordinate
I	Intensity
N	Number of photons emitted
N_A	Avogadro's constant
S_c	Irradiation of calibration lamp
h	Planck's constant
η	Filter efficiency
τ	Optics efficiency
λ	Wave length
ν	Frequency of light
Δ t	Exposure time
St	Strouhal number
St_c	Critical strouhal number
f	Forcing frequency
A	Forcing amplitude
D	Diameter of the burner at the exit
U_0	Convective fluid velocity
Le	Lewis number
Da	Damköhler number

Abbreviations

WW I	World War I
IC	Internal combustion
WW II	World War II
SI	Spark ignition
SCR	selective catalytic reduction
LHV	Low heating value
DME	Dimethyl ether
HRR	Heat release rate
1D	1 dimension
PIV	Particle image velocimetry
DEHS	Di-ethyl-hexyl-sebacate
CMOS	Complementary metal–oxide–semiconductor
OC	Outer cone
IC	Inner cone
3D	3 dimension
2D	2 dimension
FWHM	Full width half mean
LED	Light emitting diode
sCMOS	scientific Complementary metal–oxide–semiconductor
ROI	Region of interest
ND	Neutral density
LES	Large eddy simulation
DNS	Direct numerical simulation
PDF	Probability density function

GENERAL INTRODUCTION

Today, in 2022, the idea of using ammonia as a fuel has received worldwide attention and is one of the most sought fuels by combustion researchers. But like any new idea proposed faces a dispute, there is still a debate among the researchers, some vouching for the use of ammonia as a fuel due to its non-zero carbon along with some other desirable properties while others emphasizing largely on the downside of using ammonia. Chemically formulated as NH_3, ammonia is well known to the common man for its use as a refrigerant and also as a fertilizer. It was first used as a refrigerant in the 1850s in France and was applied in the United States in the 1860s for artificial ice production [20]. Ammonia is produced on a large scale by the well-known Haber-Bosch process which was originally developed by Fritz Haber in Germany to use ammonia as fertilizers, later joined by Carl Bosch to scale up the production during World War I (WWI) to use nitrates as a source of ammunition [21]. Using ammonia as a fuel for internal combustion (IC) engines dates back to the early 1800s and saw a surge in its use as an alternative fuel during World War II (WWII) when oil stockpiles became low [22]. In recent times, there is an alarming concern with the ever increase in carbon emissions and the rapid depletion of fossil fuels calling for the need for alternative green fuels. Several attempts are being made to curb these harmful emissions which cause global warming further leading to climate change. Many countries have pledged to reduce their carbon footprint and resort to green sources of energy and have also signed conventions like the Kyoto protocol [23] and the Paris agreement [24] and have been actively participating in global summits. Hydrogen is an excellent example of a green fuel that has been accepted widely as a solution to present-day problems. However, there is still a risk of storing and transporting hydrogen due to its explosive nature. Another solution that is proposed is to use electric batteries but the safe disposal of these batteries without impacting the environment still needs to be addressed. Studies on metallic combustion and biofuels are still in progress. The storage of energy from renewable sources of energy is still a major issue. Research on ammonia shows that on overcoming a few obstacles, ammonia as a fuel is feasible and has a promising future.

The Gazamo process (patented by J.L. Restieau and E. Kroch) was the first application of using ammonia as a fuel in a large-scale road test in 1941-

1942 [25]. In November 1942, during WW II, when Belgium faced a shortage of diesel, public transportation had come to a halt. The engineers had adapted about 100 buses to run on liquid ammonia, pumped into tanks on the buses' roofs. The buses travelled over 100,000 km without a single accident or spill [26]. During the 1960s, efforts were made by the US military forces to study alternative fuels including ammonia [27]. NASA developed X-15, the fastest aircraft ever built that used the XLR99 engine fuelled by liquid ammonia had set outstanding records [28]. The use of ammonia in gas turbines [29] and especially in spark-ignition (SI) engines [30] has already been tested. In 2008, a diesel-fuelled 2007 Dodge Truck and a 2008 gasoline-fuelled Ford Crown Victoria was converted to run on NH_3 [25]. Zamfirescu and Dincer [31] have shown that ammonia is the cheapest fuel per 100 km driving range and is cost-effective when compared to other fuels like hydrogen. The economic statistics report by the ARPA-E, U.S. Department of Energy [32] shows that ammonia is the most feasible form of energy delivery option for transportation when compared to both hydrogen and gasoline. This non-carbon fuel has also been of interest to power up marine engines. Germany's MAN Energy Solutions and Korean shipbuilder Samsung Heavy Industries are part of an initiative to develop the first ammonia-fuelled oil tanker by 2024 [33].

Although the first use of ammonia combustion in the last century was in public transportation in Belgium, the first publication available in the database today is by Egerton [34] and Strutt [35] in 1912 where they inspect an ammonia flame. Bodenstein [36] traced out the intermediate products both experimentally and theoretically. One of the first studies of this century published on ammonia combustion in an engine is by Peter Van Blarigan [37] where he studies the use of several alternative fuels in an engine. Konnov and Ruyck [38] provided improved kinetic modelling for ammonia decomposition with corrected sensitivity coefficients and rate constants. Most of the studies concluded that ammonia combustion has low flame speeds leading to an early blow-off. Interest began to spark in studying blended fuels. One of the first thesis published this century on ammonia/methane combustion is by Mann [39] where he studied the use of ammonia as an additive in methane/air flames. It was concluded that the NOx emissions were quite high. CFD studies in various domains started becoming popular and one of the first simulation studies of this century dedicated to ammonia combustion was a detailed DNS on ammonia/methane combustion provided by Grcar et al [40] in 2004, where they used the kinetic scheme of Glarborg [41]. Overall the results in ammonia combustion started to show that this fuel has good potential but it was important to address the emissions from ammonia itself. There are several studies on NOx emissions and on how to reduce them [42–44]. It is known that ammonia is hazardous when released into the atmosphere due to its high toxicity. From the investigations made by Westlye et al., [45] on a spark-ignition engine, it was concluded that there may be unburned ammonia emissions along with intermediary oxides of nitrogen which are harmful to the environment. To reduce the impact of these emissions, a selective catalytic reduction (SCR) was developed to promote complete combustion and also to ensure that exhaust emissions do not pollute the environment. Attempts are being made to make the manufacturing process of ammonia carbon-free. Green ammonia is made with hydrogen that comes from water electrolysis powered by alternative energy. A massive project in Saudi Arabia aims to make more than 1 million metric tons of ammonia per

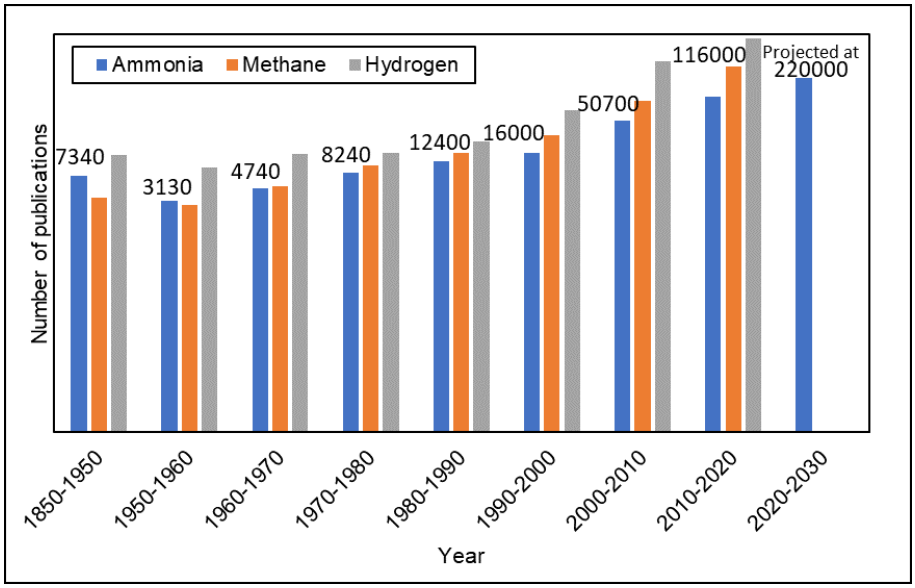

Figure 1: Comparison of the trend for ammonia (blue), methane (orange), and hydrogen (grey) for almost two centuries. The number of publications is represented in the logarithmic scale

year [46]. Weighing 17 g/mol, it is often compared to methane which weighs 16 g/mol and is similar in structure. Although methane flames are associated with higher speeds, ammonia flames have a higher-octane rating. Researchers often compare and contrast the behaviour of these two flames. As research in blend studies depict an easy solution to overcome the undesirable aspects, ammonia is often combined with hydrogen or methane to increase the overall performance like the flame speeds, flammability limits, and power output [47, 48]. There are also a large number of studies on blending ammonia with oxygenated fuels or oxygenated air which results in increasing the performance as well. Since ammonia can be easily stored and transported and by decomposing one mole of ammonia, one can produce 3 moles of hydrogen; studies show that it can be used as a hydrogen carrier [49, 50] by simply cracking ammonia. It can also be used as fuel cells as shown in some studies [51–53].

From preliminary research in the literature available back in 2019 and on reading reports from various countries/continents including Japan, China and, Europe, it was seen that ammonia could be the main source of energy of tomorrow if the major problems pertaining to the use of ammonia is well addressed. This meant that there is a large scope of work that needs to be done to put it into use. From a scientific point of view, ammonia has definitely become a trendsetter and the new talk amongst combustion researchers who are in the quest for a capable green replacement for conventional fuels. Figure 1 represents a bar graph to show an approximated number of papers published every decade on ammonia combustion (blue), methane combustion (orange), and, hydrogen combustion (grey). The number of publications is on a logarithmic scale. The numbers on top of the bar represent the approximated number of publications on ammonia combustion and it can be seen that it increases expo-

nentially signifying the strong research interest. The estimated value for this decade stands at a massive 220000. On comparing the three fuels, it can be seen that a large amount of work is dedicated to hydrogen combustion followed by methane, and finally ammonia combustion. However, the trend over the decades shows that publications in ammonia combustion are increasing much faster than methane combustion but still lesser than hydrogen combustion. This is an indicator of the dichotomy among combustion researchers. As an aspiring researcher myself with similar goals, it was agreed upon by my team to contribute to the ammonia research. There is a lot of literature on ammonia blended fuels. In order to understand the behaviour of blended fuels, one must have sufficient knowledge of the properties of the individual fuels. The main priority of this particular work is to add to the pure ammonia studies. The use of ammonia in SI engines and gas turbines has been well-established due to its high octane number and anti-knock characteristics. However, there is a dearth of data needed for engine sizing at the conditions encountered in these combustors. Finding flame speed data under these conditions was the first goal. Further, it was seen that there were not a lot of studies on the inner structure of the flame. If one needs to know how to enhance the combustion process, it is important to understand the parameters affecting the flame. And so, the second goal is to understand certain properties of ammonia flames. It was noted that there was no previous attempt to provide the concentration of some of the excited species. A qualitative and quantitative analysis was done for various excited species. It is known that turbulent flames enhance mixing thereby promoting the combustion process. It is also known that turbulent flames are extremely complex in nature. The first and perhaps, the most basic step is to study a perturbed laminar flame. Though a perturbed laminar flame is quite far from turbulent flames, it can help to give an insight into how flames respond when subjected to a perturbation. Therefore, establishing the final objective of this thesis: to study flame-acoustic interactions.

To meet the objectives set, this thesis has been divided into 3 parts:

(i) **Part I:** Laminar flame speeds at high pressure and temperature,

(ii) **Part II :** Inner structure of a stretched premixed flame and,

(iii) **Part III :** Chemical and dynamical analyses of a premixed flame.

Part I is dedicated to obtaining flame speeds and evaluating some of the kinetic schemes present in the literature at elevated conditions for lean, near stoichiometric, and, rich mixtures. The goal of **Part II** is to understand different reactive properties as well as the inner structure of the stretched premixed flame at different equivalence ratios. **Part III** has two important aspects. The first aspect is to provide qualitative and quantitative analyses of some of the excited species. The second aspect is to understand the effect of the perturbation on the inner structure of the flame at different equivalence ratios. Each part is further divided into chapters with a brief introduction and a conclusion. This brief introduction aims to provide the goal of the study and the gist of each chapter and the conclusion gives an overview of the study. This thesis finally ends with a conclusive summary and a note probing into the future scope of this project.

Part I

Laminar flame speeds at high pressure and temperature

INTRODUCTION

It is known that using ammonia in SI engines [30] and gas turbines [29] and is favourable in SI engines due to its anti-knock properties owing to its high-octane number. The pressure encountered in these combustors is in the range of 20 bar at light loads and 70-100 bar at full load. Flame speed is one of the important sizing parameters of an engine. And so, there is a need of flame speed data at elevated conditions. The objective of this part is to provide flame speed data for oxy-ammonia flames up to a pressure of 30 bar and a temperature of 585 K and to evaluate the recent kinetic schemes in the literature for these conditions [54].

Chapter 1 discusses the literature available for the flame speed of pure ammonia and ammonia blended with other fuels along with a brief assessment of the kinetic schemes available in the literature.

Chapter 2 focusses on the experimental set-up (OPTIPRIME) used to obtain the high pressure and temperature conditions. The theory involved in converting the obtained experimental data to flame speed has been addressed as well. The experimental test conditions and the chosen kinetic schemes from the literature have been listed.

Chapter 3 presents the first part of the results of this study i.e. the flame speed data at elevated conditions along with an evaluation of the chosen kinetic schemes. An effort has been made to understand the reactions involved with pressure change through sensitivity analyses. The important reactions have been marked out and the behaviour of the flame speed with the pressure and temperature change has been noted.

Chapter 4 highlights the second part of the results. The effect of temperature and pressure on flame speeds has been isolated and studied to understand the behaviour noted in Chapter 3. The effect of diluents on the flame speed over the chosen range of pressure and temperature has also been examined. A range of exponential factors α and β in the flame speed model has been provided as well marking the importance of pressure and temperature effects on ammonia flame speeds.

To conclude a 3D evolution of flame speed with pressure and temperature along with a fit model optimised to fit the experimental data has been provided. This 3D map and the fit equation enable us to provide flame speed for any

pressure and temperature within the given pressure and temperature range and the initial conditions used in this study.

CHAPTER 1

CHAPTER 1

Ammonia combustion has indeed become a vast topic with a lot of work done especially in the past few years as pointed out in the statistical analysis in the section General Introduction. This chapter aims to give a brief literature review on laminar flame speed data obtained experimentally and numerically.

1.1 Literature review on experimental flame speed data in ammonia combustion

One of the first reports on experimental ammonia flame speed was by Andrews and Gray [55]. They measured flame speeds for ammonia in oxygen, a mixture of ammonia and oxygen with different diluents like argon, helium and nitrogen for an equivalence ratio ranging between 0.18 and 1.13 at 333 K and a pressure ranging between 0.005-0.009 MPa in a closed vessel with schlieren photography. Different techniques are used to determine the flame speed to achieve different ranges of conditions. The most common technique that was used was a closed spherical vessel.

Despite the numerous properties which make ammonia a desirable fuel, there are a few added disadvantages in addition to the low flammability limit and the low LHV. Ammonia is well known to be hazardous when released into the atmosphere due to its high toxicity. The value of flame speed for an ammonia-air mixture at ambient atmospheric conditions has been reported to be as low as 7 cm/s at an equivalence ratio, $\varphi = 1.1$. From a combustion performance point of view, this low speed of ammonia flames [56, 57] leads to an early blow-off and a difficulty in the ignition. Ammonia is often combined with hydrogen or methane to increase the overall performance like the flame speeds, flammability limits and power output. Literature is available on different conditions for the combined fuel mixture [58, 59]. Data at high pressure and high temperature is available for ammonia mixed with hydrogen or methane [60–64]. On one hand, ammonia is blended with other fuels and on the other hand, ammonia is also burnt with oxygenated air mixtures [65] to

attain similar goals.

For pure ammonia combustion, analyses have been made for a narrow range of pressure and temperature conditions for different equivalence ratios [57]. Most of the data are obtained at ambient conditions. The newest data available aims at combining ammonia with other non-conventional fuels like Dimethyl ether (DME), ethanol and even, methanol. Table 1.1 gives a synopsis of the experimental literature available in ammonia combustion.

Despite the abundant data, when it comes to high pressure and temperature conditions it is seen that the maximum flame speed for ammonia combustion available in the literature is much lesser than what is encountered in gas turbines and engines.

From the flame speed data obtained by combining ammonia with either other fuels or by using oxidizers that contain more oxygen than that of air, the flame speed, flammability limit and energy release have been significantly improved. Some of the unique properties like the lack of change in values of burned Markstien length at 0.3 MPa and 0.5 MPa have been recently pointed out [79].

1.2 Literature review on kinetic schemes in ammonia combustion

There are several kinetic schemes developed for ammonia combustion which are available in the literature. There are assessments on various aspects like predictions of NOx emissions, ignition delay time etc. Nevertheless, the focus of this section is purely on evaluating the performance of laminar flame speed prediction and sensitivity analyses. Despite the focus being on laminar flame speed assessment and sensitivity analyses, this is not the only criteria to evaluate to rate the performance of any kinetic scheme.

On performing a literature review [7, 74], it was understood that Okafor [1] gave the most congruent results for lean mixtures and Klippenstein [2] and Zhang [3] gave the best results for the fuel-rich mixtures. Konnov [4] and Mathieu [5] seem to over-estimate and under-estimate the flame speeds respectively when compared to the experimental data [6]. Goldmann and Dinkelacker [61] analyse different schemes and concluded that Mathieu's mechanism tends to underpredict whereas Tian's [90] and Konnov's mechanism tend to overpredict the laminar flame speed of ammonia/air mixtures. Xiao and Valera-Medina [91] compared 12 of the latest schemes for ammonia/hydrogen mixtures and concluded that Mathieu gave the best agreement with their experimental data. The mechanisms of Konnov, Miller [92], Duynslaegher [93] overpredicted the values whereas Lindsted [94] overpredicted only for the lean conditions and were well within the range for rich conditions. On the other, the scheme of Abo Akademi (AA) [95] underpredicted for lean mixtures and was within the experimental range for rich mixtures. Dagaut [18] , Klippenstein [2] , Tian and Mendiara [96] slightly underestimated the flame speed values. GRI 3.0 [97] and Mevel [98] gave flame speed data that was lower than the experimental range by over 50%.

From the perspective of sensitivity analyses [7], $H + O_2 \rightleftharpoons O + OH$ is the most dominant reaction with its sensitivity to flame speed value being around 0.5. The mechanisms of Mendiara and Glarborg, Okafor et al., Otomo

et al. and Mathieu and Petersen, which predict better the experimental data, show the reaction $H^{+}NO^{+}M \rightleftharpoons HNO^{+}M$ as the second most important in the promotion of flame speed in ammonia-air mixtures, with sensitivity values between 0.1 and 0.2. The mechanisms that overpredict the flame speeds have this reaction as a lesser important one. The mechanisms of Konnov and Dagaut et al do not list this reaction among the ten most important, and the mechanism of Glarborg et al. provides a sensitivity value of less than 0.1 for the same reaction. The mechanisms of Konnov, Klippenstein et al. and Glarborg et al. show the reaction NH2+NO <=> NNH+OH as one of the most important with sensitivity values higher than 0.1.

Wang et al [74] in their work also mention that $H + O_2 \rightleftharpoons O + OH$ is the most dominant reaction with the most important rate-limiting branching reaction for laminar burning velocity predictions. They noted that $H_2 + O \rightleftharpoons H + OH$ is active when the H_2 concentration is high at rich mixtures, but its sensitivity is not notable in the scheme of Okafor. In contrast, the sensitivity of reactions in the HNO, and NHx sub-mech presented higher positive values at lean mixtures. Two reactions $NO + H + M \rightleftharpoons HNO + M$, $NH_2 + NO \rightleftharpoons NNH + OH$ consuming the NO and generating active radicals, give large positive sensitivity in both models, the terminating reaction $HNO + H \rightleftharpoons NO + H_2$ generating NO, gives large negative sensitivity. In different conditions, NO can either promote fuel oxidation by converting stable HO_2 radicals into active OH radicals or inhibit fuel oxidation by the removal of free radicals through a catalyzing recombination process. Two opposite effects are competitive, but in the given test conditions, the inhibiting effects were dominant, resulting in the NO consumption reactions possessing positive sensitivity to laminar burning velocity. For rich mixtures, sensitivity of $NH_2 + NH \rightleftharpoons N_2H_2 + H$, $NH_2 + O \rightleftharpoons HNO + H$ are notable in Zhang (2017). Similarly, two reactions in the N_2H_x block $N_2H_2 + M \rightleftharpoons NNH + H + M$, $N_2H_2 + H \rightleftharpoons NNH + H_2$ also gives large sensitivity, but they were not notable in Okafor. It implies that the discrepancy of Okafor in the rich conditions may due to the incompleteness of N-2-related reactions.

From Xiao and Valera-Medina's work [91], it was concluded that $H + O_2 \rightleftharpoons O + OH$ and $H + O_2\,(^{+}M) \rightleftharpoons HO_2\,(^{+}M)$ have the largest impacts on the predictions of flame speed in Miller and Mathieu with these reactions playing a larger role in the scheme of Miller. For rich conditions, $H + O_2 \rightleftharpoons O + OH$ has the largest impacts on the predictions of flame speed in both mechanisms while the most inhibiting reactions in the two mechanisms are different, $N + OH \rightleftharpoons H + NO$ in Mathieu mechanism and $H + O_2\,(^{+}M) \rightleftharpoons H + O_2\,(^{+}M)$ in Miller mechanism.

Overall, depending on the mechanism, different reactions are highlighted as the most important set of reactions for the same initial conditions. As the initial conditions change, the important set of reactions that plays a major role too changes.

Table 1.1: Experimental literature available on ammonia combustion

Mixture	φ	**T (K)**	**P (Mpa)**	**Technique**	**Author**	**Year**	**Ref.**
NH_3/DME	0.7-1.6	298, 373, 423	0.1, 0.2, 0.4, 0.5	Closed spherical vessel	Yin et al.	2022	[66]
NH_3/O_2/He/Ar	0.7-1.3	298	0.1-1.5	Closed spherical vessel	Hou et al.	2022	[67]
NH_3/C_2H_5OH	0.8-1.3	423	0.1	Closed spherical vessel	Pelé et al.	2022	[68]
NH_3/air	1	600,700	0.1,0.3	Stagnation flow	Hayakawa et al.	2021	[69]
$NH_3/H_2/O_2$/Ar (N_2)	0.7-1.5	368	0.1	Mache-Hebra burner	Osipova et al.	2021	[70]
NH_3/C_2H_5OH/ CH_3OH	0.7-1.8	298-448	-	Heat flux burner	Wang et al.	2021	[71]
NH_3/H_2/air	0.7-1.7	298-473	0.1-1	Closed spherical vessel	Shrestha et al.	2021	[72]
NH_3/syngas/air	0.7-1.6	298	0.1	Heat flux burner	Han et al.	2020	[73]
$NH_3/O_2/N_2$	0.6-1.4	303	0.1	Constant volume chamber	Wang et al.	2020	[74]
NH_3/H_2/air	0.8-1.4	298-473	0.1	Closed spherical vessel	Lhuillier et al.	2019	[75]
NH_3/air	0.8-1.3	298	0.1	Heat flux burner	Han et al.	2019	[48]
NH_3/O_2	0.2-2	298	0.1	Constant volume chamber	Liu et al.	2019	[76]
$NH_3/O_2/N_2$	0.6-1.5	298	0.1-0.5	Constant volume cyl.	Mei et al.	2019	[77]
NH_3/air	0.8,1,1.2	298	0.1	Swirl burner	Hayakawa et al.	2017	[78]
NH_3/H_2/air	1	298	0.1-0.5	Closed vessel	Ichikawa et al.	2015	[79]
NH_3/air	0.7-1.3	298	0.1-0.5	Closed vessel	Hayakawa et al.	2015	[80]
NH_3/H_2/air	1-1.25	293	0.1	Burner direct imaging	Li et al.	2014	[81]
NH_3/H_2/air	0.5-1.1	293	0.1	Burner direct imaging	Kumar et al.	2013	[82]
NH_3/H_2/air	0.6-1.67	293	0.1	Closed vessel	Lee et al.	2010	[83]
NH_3/air	0.89-1.2	298	0.1	Closed spherical vessel	Takizawa et al.	2008	[84]
NH_3/air	0.9-1.3	298	0.1	Vertical tube direct imaging	Jabbour & Clodic	2004	[85]
NH_3/air	0.49-1.19	295	0.15	Closed vessel	Pfahl et al.	2000	[86]
NH_3/air	0.58-1.79	300	0.1-0.2	Closed vessel direct imaging	Ronney	1988	[87]
NH_3/air	0.74-1.35	293	0.1	Vertical tube direct imagingl	Zakaznov et al.	1979	[88]
$NH_3/H_2/O_2$/Ar/ N_2	0.18-1.13	333	0.005-0.009	Closed vessel	Andrews & Gray	1964	[89]

CHAPTER 2

CHAPTER 2

This chapter is dedicated to describing the experimental method and the simulations that were carried out using Chemkin-Pro. The test conditions and the chosen kinetic schemes are also presented here.

2.1 Methodology

There are several methods to experimentally calculate flame speeds. The method to be used depends on the targeted conditions. For example, the stagnation/counterflow method and Bunsen burners are used for low-pressure and temperature conditions. Spherical flame propagating in constant pressure chambers and constant volume chambers are the most common methods used for elevated conditions. Constant volume chambers can cover a wider range of high-pressure and temperature conditions. Hence, it has been deployed as the experimental apparatus here. Also, since the idea is to find flame speed for SI engines and gas turbines which under ideal conditions follow the Otto cycle where two strokes happen at constant volume conditions, it is useful to investigate flame speeds using the constant volume method.

To validate the kinetic schemes available at these conditions, CHEMKIN a software tool originally developed at Sandia National Laboratories for solving complex chemical kinetics problems is used. Chemkin- Pro 2009 version is used to obtain the results here. Three input files are used to carry out the simulations.

(i) an input file containing the elements, species and reactions,

(ii) a thermodata file containing data required to compute different thermal quantities like enthalpy, entropy and, heat capacity for a given temperature range,

(iii) and, a transport data file containing the diffusion and collision coefficients.

2.1.1 Experimental set-up description

The experiments are performed in the full OPTIcal access Perfectly spheRical combustIon chaMber (OPTIPRIME) facility of ICARE-CNRS, Orléans, France. The salient features of this new chamber are a perfect sphericity of the inner chamber surface and a full visualization of the flame front propagation from the central ignition to the walls. The use of a 360° fused silica ring enables a complete flame visualization. The inner and outer surfaces of this fused silica ring are machined to ensure perfect internal and external spherical profiles. The outer diameter of the crown is 144 mm with a quartz thickness of 11 mm. This thickness was calculated such that it holds at a pressure greater than 100 bars. OPTIPRIME consists of the assembly of two stainless steel half shells with a 360° fused silica ring with spherical inner and outer surfaces in-between as illustrated in Figure 2.1. The internal volume is scrupulously spherical, and its radius is R_0 = 60.85 mm (i.e. 0.943 litres in volume). There are several important advantages to smaller combustion bombs. The effects of radiation and hydrodynamic instabilities are less pronounced at small flame radii. One drawback of working with small flames is that they are more strongly affected by stretch.

To minimize dead volumes, the diameters of the inlet (1/16 inch) and exhaust (1/8 inch) tubing were reduced and their end is flushed with the inner surface of the chamber. The exhaust tubing is larger to facilitate the vacuum procedure after each test. Two pressure sensors (AVL GU21D), with high sensitivity and high frequency, are arranged diametrically opposite in the chamber. The sensitive surface of the sensors is flushed. The sensitivity and frequency of the sensor are 35 pC/bar and 85 kHz, respectively. The linearity of the sensor is ± 0.3 % of the full-scale range. A type-K thermocouple with a stainless steel sheath is introduced into the chamber to control the initial temperature of the unburnt gas. As shown in Figure 2.1, the combustion chamber is placed in the centre of a furnace with a volume of 32 L, having a power of 1050 W and is capable of operating over a temperature range of 10 °C to 300 °C with time stability lower than 0.2 °C. A complete immersion of the chamber has the major advantage of avoiding temperature gradients either on the enclosure or in unburnt gas. The maximum initial temperature (200 °C) is limited by the thermal resistance of the pressure sensor cables as the whole system is in the furnace. In the context of this study, the furnace was not used as the experiments were performed at room temperature.

To ensure perfect mixture repeatability, a high-pressure buffer tank (3.78 L) is filled with the components of the desired mixture following Dalton's law of partial pressures. The relatively large volume of the buffer tank, compared to the chamber volume (i.e. less than 1 L), allows for carrying out successive shots tests to ensure repeatability with minimum errors. The detailed experiment set-up description is provided in [15].

2.1.2 Radius and pressure evolution

Flame propagation was observed from its ignition point until it hit the chamber walls through the 360° fused silica ring. The accurate flame front position determination using chemiluminescence through the ring was assessed in [15]. A CMOS camera (PHANTOM V1611) placed in front of the chamber

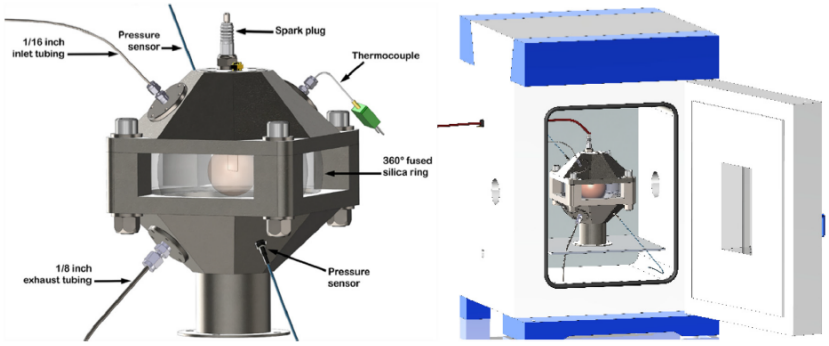

Figure 2.1: Sketch of the spherical combustion chamber - OPTIPRIME (left) and the furnace (right) [15].

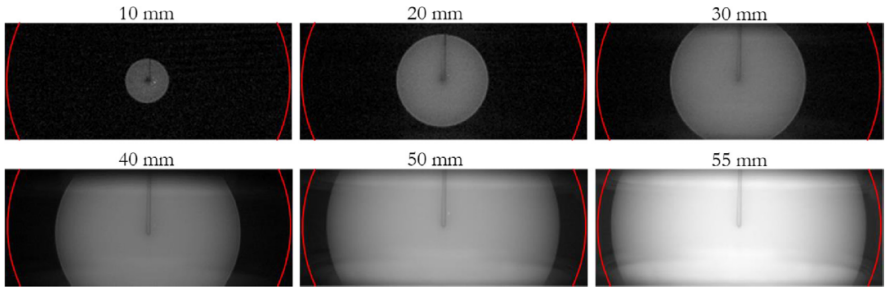

Figure 2.2: Time-based evolution of flame radius as the flame front propagates from its ignition to the walls. The mixture used here is methane-air at φ=1.3, p0=1 bar and T0=300K [16].

aligned with the window is used to capture the images at an acquisition rate of 12000 fps for the present study. The camera electronic shutter was set to the minimum value allowing sufficient flame detection during propagation (i.e. $< 10\ \mu s$ for all flame conditions), ensuring that the flame front displaces for largely less than one pixel during this time. The resolution of the CMOS sensor was set to 1024 $\times$768 pixels^2. An example of flame propagation visualization is illustrated in Figure 2.2. Here, in Figure 2.2, a rich methane-air mixture is shown. The inner lateral spherical surface of the combustion chamber is delimited by the left and right red arcs. The ring allows a maximal vertical field of view of 50 mm. As illustrated in Figure 2.2, flame visualization is possible until the flame reaches the wall. The plane in which the electrodes are located is tilted to be perpendicular to the viewing axis of the camera. The accuracy of the flame radius determination has been carefully assessed in [15]. The contributions of the different sources of inaccuracy were considered and precision on the flame radius of less than 0.5 % is attributed, as the pressure increases.

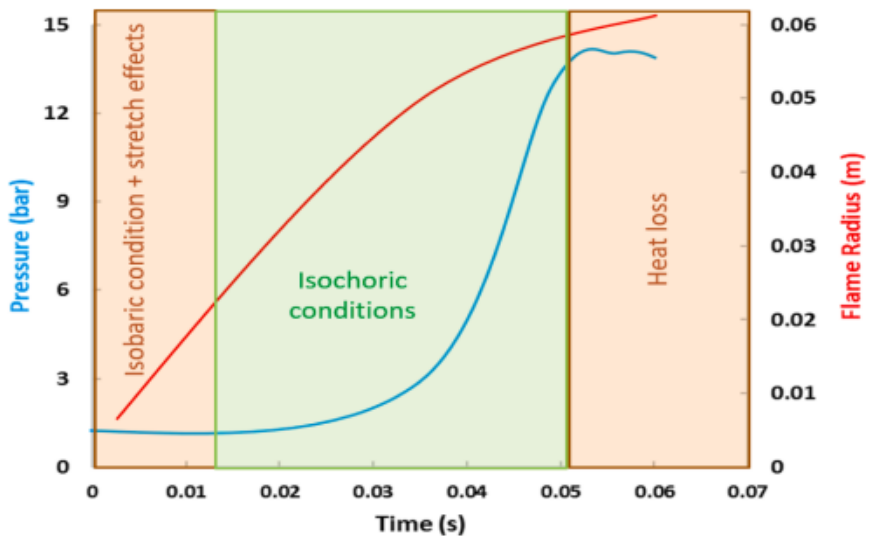

Figure 2.3: Pressure and radius evolution with regions of stretch effects and heat losses (regions where the data cannot be retrieved) and isochoric conditions (region for which data is presented here) [17].

Pressure traces were acquired at a frequency of 20 kHz using two identical pressure transducers, connected to charge amplifiers linked to an acquisition system. The linearity of the sensor is $\pm$ 0.3 % of the full-scale range. The two pressure traces are similar until the flame reaches the wall so only data from the top sensor is taken. Pressure and flame radius signals, and their time derivatives, were filtered using zero-phase digital filtering to remove noise. Both the order of the filter and the range of data considered (minimal and maximal pressure) were systematically varied and adapted to each signal to ensure that this filtering procedure does not affect the results. the typical pressure and flame radius evolutions are demonstrated in Figure 2.3 for one of the cases. Pressure transducers and the high-speed camera are both triggered

at the ignition deposit. When the flame is close to the chamber walls, the pressure evolution is affected by heat losses which prevent it from reaching the theoretical end pressure. The minimal flame radius detection is limited to 10 mm to avoid any disturbance from the ignition. Both isobaric and isochoric measurements can be taken from this setup. However, in the present study, only the isochoric measurements are of interest. The isochoric method has the advantage to afford a large quantity of flame speed data for elevated pressure and temperature conditions. This method had been initially limited, to 2 $<$ p/p0 $<$ 5. The maximum pressure/radius to be considered for the flame speed evaluation should correspond to the adiabatic process. As explained in Omari and Tartakovsky [99] and Burrell et al. [100] , the time derivative of the pressure trace is a good indicator of the heat losses to the wall. In [15] , a criterion of 90% of max (dp/ dt) was introduced to define the maximum experimental pressure to be considered in order to ensure that no wall effect can occur during the propagation investigated. The detection of instabilities by direct visualization or chemiluminescence was illustrated in [15] , 23] and the reader is referred to [15] . This method may help to detect the occurrence of instabilities for weakly stretched flames. For unstable flames, the curves exhibit a slight change of slope and the position of max (dp/ dt) is advanced. This information may be useful to detect the occurrence of instabilities in the absence of optical access. With a criterion of 90% of max (dp/dt) , the maximal pressure to consider is initially estimated to be at least five times the initial pressure (5 p0) for all stable conditions. The position of max (dp/dt) occurs for slightly lower p/p0 when pressure is increased, keeping the initial temperature constant (i.e. T^0 = 300 K). This would suggest that heat losses to the wall are more pronounced as initial pressure increases, which can be explained by the slowing down of the flame front and so an increase of the propagation and heat exchange times. More details associated to the use of this method for the experiments performed is described in [16].

2.1.3 Heat loss model

In [17] various criteria to determine the limit of high pressure at which heat losses occur including the previously proposed 90% of max (dp/dt) have been compared. The newly proposed criterion [17] is defined as the minimum of δ_{ph}. This definition relies on a constant value of A (the ratio between the preheating and the reaction zone) and can be numerically assessed as δ_{ph} over δ_{f} where δ_{ph} is defined between T_u + 1% and T_{ignition}, the latter being difficult to evaluate. The temperature corresponding to the position where 5% of the unburnt fuel mass fraction is consumed was arbitrarily considered as T_{ignition}. Over evaluating a large range of conditions, A was determined to be around 5. Upon comparison with other criteria, the authors affirm that the minimum of (δ_{ph}) is a well-optimized criterion for the extraction of high-pressure S_u and has been validated against the DNS calculations. For flame speed evaluation, this criterion is chosen as the upper-end limit on pressure. The results presented here have been evaluated using this criterion. For more information on this model, the reader is referred to [17].

2.1.4 Flame speed evaluation

OPTIPRIME is designed to afford several important pieces of information on flame dynamics like:

(i) information on the occurrence of instabilities on the flame surface

(ii) the laminar flame speed and the burned gas Markstein length can be evaluated during the initial isobaric propagation

(iii) the knowledge of the pressure and the flame radius traces allows evaluating the flame speed evolution for quite a large range of pressure and temperature conditions during the isentropic compression.

For the given scope, only the variation of pressure and temperature under isochoric conditions is of interest. It is assumed that pressure and temperature vary isentropically. Keeping the same pressure range for all conditions allows quasi-identical fresh gas temperature variations as the heat capacity ratio of the unburnt gas remains almost unchanged. The isentropic compression induces an absolute temperature variation of 100 K in the considered pressure range whereas the absolute pressure variation is proportional to the initial pressure. These different absolute variations explain the different trends observed for different initial pressure conditions. The constant volume method proposed by Lewis and von Elbe [101] uses the unsteady pressure-time history during the flame propagation event. Conversion of the reactants to hot products across the flame front results in a rapid pressure rise and a corresponding temperature rise in unburnt and burnt gas. The constant volume technique seeks to relate the instantaneous flame speed to the pressure history. In other words, in a single test, flame speeds can be obtained for a range of higher pressures and temperatures. Recently, Hinton et al. [102] pointed out the fact that the method using the pressure rise requires a more complex analysis, but has the advantage that a single experiment generates data across a range of linked temperatures and pressures [100]. The pressure and temperature rise also meaning that data can be obtained for engine-like conditions. Equations for this method have been the subject of several pioneered publications [103] . Based on the following assumptions: the pressure (p) is spatially uniform; the constituents of the burnt and unburnt gas behave as ideal gases, the following expression for the flame speed (S_u) was derived:

$$S_u = \frac{dR_f}{dt} - \frac{(R_0^3 - R_f^3)}{3\gamma_u R_f^2 p}\frac{1}{\rho_u}\frac{d\rho_u}{dt} \tag{2.1}$$

where R_f and R_0 represent the flame radius and the inner chamber radius respectively, p is the pressure in the chamber and γ_u is the heat capacity ratio of unburnt gas.

Experimental evaluation of the compression term

$$(\frac{1}{\rho_u}\frac{d\rho_u}{dt}) \tag{2.2}$$

is possible but delicate [104] . Alternatively, assuming that the unburnt gas is isentropically compressed yields:

$$S_u = \frac{dR_f}{dt} - \frac{(R_0^3 - R_f^3)}{3\gamma_u R_f^2 p}\frac{dp}{dt} \tag{2.3}$$

where R_f and R_0 represent the flame radius and the inner chamber radius respectively, p is the pressure in the chamber and γ_u is the heat capacity ratio of unburnt gas. To evaluate the flame speed, both the pressure and the flame radius need to be determined simultaneously over a sufficiently long period to enable the computation of fairly accurate derivatives. To overcome the lack of optical access in conventional isobaric combustion chambers, a relation linking the flame radius to the pressure is usually used: unburnt gas is isentropically compressed yielding:

$$\frac{R_f}{R_o} = (1 - (1 - x)(\frac{p_o}{p})^(1/\gamma_u))^(1/3) \tag{2.4}$$

with p0 the initial pressure in the chamber and $x = m_b/m$ the burnt gas mass fraction (with m the total mass and m_b the burnt gas mass). Similar to the flame radius, the burnt gas mass fraction is not accessible experimentally. The x = f(p) relation is either determined via numerical modelling [103, 105] or via simplified assumptions. The simple linear relation initially derived by Lewis and Von Elbe [101] is still widely used:

$$x = \frac{p - p_o}{p_e - p_o} \tag{2.5}$$

with p_e the theoretical end-pressure, which should be evaluated using thermochemical calculations. Its value significantly affects the flame speed determination and may be influenced by dissociation [106] . However, in this case, thanks to the wide optical access, instantaneous pressure and radius data can be obtained and may be directly used in equation 2.3 to evaluate the flame speed. More information on the methodology and validation is provided in [15, 16, 100, 107–109].

2.2 Chemical kinetic schemes

On performing a literature survey, 9 recent kinetic schemes for ammonia combustion have been chosen for this study and are presented in Table 2.1. The flame speed was calculated in Chemkin-Pro for a pressure-temperature pair which evolves isentropically mimicking the experimental combustion process. Among the 9 chosen mechanisms, it was seen that 2 mechanisms- Nakamura and Hasegawa [8] and Stagni et al. [9] predicted and captured the experimental results at all conditions better than the other mechanisms. Although all the chosen mechanisms could aptly produce the trend, i.e. the flame speed increases with an isentropic increase of temperature and pressure for all the test conditions; there is a variation in the flame speed values. To understand this and to highlight the role of the key reactions, sensitivity analyses were performed. In addition to these 9 mechanisms, three latest mechanisms were added and it was seen that three mechanims didn't predict flame speeds close to the experimental flame speeds.

2.3 Test conditions

The tests were performed for a mixture of ammonia-oxygen at 3 different equivalent ratios: 0.8, 1.1 and 1.3 at an initial temperature of 300 K. For the

Table 2.1: Chemical kinetic schemes used in this study

Kinetic Schemes	Species	Reactions	Reference
Klippenstein et al.	33	211	[2]
Dagaut et al.	42	250	[18]
Zhang et al. (2017)	37	229	[3]
Shrestha et al.	34	264	[10]
Nakamura et al.	38	232	[8]
Modified Okafor*	60	359	[1]
Otomo et al.	32	213	[19]
Stagni et al.	31	203	[9]
Mathieu and Petersen	55	278	[5]
Shrestha et al.	125	1099	[72]
KAUST	38	263	[110]
Gotama et al.	32	165	[111]

* Okafor scheme was modified to add helium using the third body coefficients of argon.

rich mixtures, the initial pressure ranged between 1 bar and 4 bar whereas, for the lean mixture, it was at 1 bar and 2 bar. 30% of the oxidiser mixture consists of oxygen and the remaining 70% is the diluent for all the conditions. The diluent is required because these flames are quite unstable in nature as both hydrodynamic and thermo-diffusive instabilities are favoured in these temperature and pressure conditions. The Lewis number of ammonia flames is close to 1 and so, in order to increase the Lewis number, there is a need of adding bath gases with high thermal diffusivity. A combination of argon and helium was used to stabilise the flame. The ratio of the diluent was chosen such that the mixture could be readily ignited and the flame sustains till it hits the wall. It is difficult to ignite mixtures with a high helium content at low pressures as helium possesses a high thermal diffusivity. In the case of high-pressure conditions, the occurrence of instabilities is promoted and so, a large percentage of helium is required to stabilise the flame. The initial conditions used are represented in Table 2.2. It is true that from an application point of view, ammonia-air flames are more relevant but these high pressure and temperature conditions cannot be easily attained by using nitrogen as the diluent. One of the ideas is also to challenge the kinetic schemes at these elevated conditions and in doing so, the flame speeds for different conditions can be predicted by using the best performing kinetic scheme. The adiabatic flame temperature has been calculated and reported in Table 2.2. At this equilibrium condition, it is seen that the dissociation reaction of H_2O to OH is favoured.

Table 2.2: Initial conditions for the test cases along with the adiabatic flame temperature (AFT)

φ	$\mathbf{P_0}$ **(bar)**	**Diluent**	**AFT(K)**
0.8	1	49% Ar 21% He	2895
0.8	2	49% Ar 21% He	2944
1.1	1	49% Ar 21% He	2976
1.1	2	49% Ar 21% He	3036
1.1	1	21% Ar 49% He	2976
1.1	2	21% Ar 49% He	3036
1.1	3	21% Ar 49% He	3069
1.1	4	70% He	3093
1.3	1	49% Ar 21% He	2885
1.3	2	49% Ar 21% He	2927
1.3	2	21% Ar 49% He	2928
1.3	3	21% Ar 49% He	2950
1.3	4	21% Ar 49% He	2965
1.3	4	70% He	2965

CHAPTER 3

CHAPTER 3

Both Chapters 3 and 4 describe the results obtained. Chapter 3 focuses on flame speeds for the different test conditions and the sensitivity analyses for the same conditions to highlight the important reactions in different kinetic schemes.

3.1 Experimental and numerical flame speeds

As mentioned in the previous chapter, the experiments were performed in the isochoric condition. The isochoric method helps to retrieve a wide band of flame speed data at elevated conditions [16,100,107–109]. This range has been chosen such that the stretch effects that occur in the initial phase and the heat losses endured when the flame front hits the wall do not affect the propagation of the flame front and hence, the flame speed. Table 3.1 represents the range of pressure and temperature for which the flame speeds have been determined. It is assumed that the temperature of fresh gases evolves isentropically while the flame front propagates. A relative accuracy of less than 0.5% on the flame radius was propagated on the flame speed leading to a maximal error lower than 5% [16]. The experiment traces have been widened to account for this uncertainty. An average of 6 shots were performed for each case to check for repeatability.

The experimental flame speeds and the flame speeds from the chosen mechanisms were calculated and plotted for all the conditions given in Table 2.2. A very similar trend for all the given conditions was noted. However, most of the schemes failed to give the flame speed value within the experimental range. Generally, it was seen that the schemes of Klippenstein, Zhang (2017) and Dagaut overestimate the flame speeds when compared to the experimental flame speed whereas Mathieu and Otomo under-estimate the flame speed. The other 4 mechanisms more or less fall within ± 5 % error bar of the experimental results. Out of the 14 cases, 3 of them are represented here in Figures 3.1, 3.2 and 3.3. The 3 chosen conditions represent a fuel-lean condition, a fuel-rich condition and a high-pressure condition to illustrate the above-mentioned

Table 3.1: Initial pressure and equivalence ratio with the range of pressure and temperature for which the flame speed has been measured. The initial temperature, T_0, was maintained at 300K

φ	P_0 (bar)	P range (bar)	T range (K)
0.8	1	2-6	369-502
0.8	2	4-16	374-555
1.1	1	2-9	371-572
1.1	2	4-16	371-557
1.1	3	6-30	372-584
1.1	4	8-37	371-575
1.3	1	2-8	370-544
1.3	2	4-17	370-555
1.3	3	6-26	370-557
1.3	4	8-36	369-563

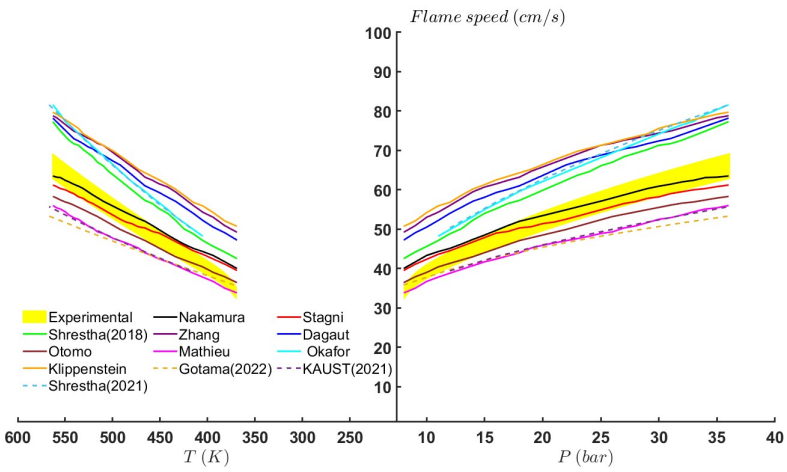

Figure 3.1: Laminar flame speeds at p_0=4 bar, T_0=302.3K, φ = 1.3, 21% Ar and 49% He.The experimental flame speeds have been thickened in yellow to account for the uncertainties incurred. The y-axis represents the flame speed whereas the x-axis is split as temperature and pressure. This is done as the flame speed is a function of both pressure and temperature which evolves isotropically during the combustion process. The orange colour represents Klippenstein [2], violet represents Zhang (2017) [3], blue represents Dagaut [18], brown represents Otomo [19], pink represents Mathieu [5], cyan represents Modified Okafor [1], green represents Shrestha [10], red represents Stagni [9] and black represents Nakamura [8]

observations. The chosen conditions help to demonstrate a fuel-rich versus fuel-lean mixture at similar initial conditions and a low-pressure versus high-pressure condition at the same equivalence ratio.

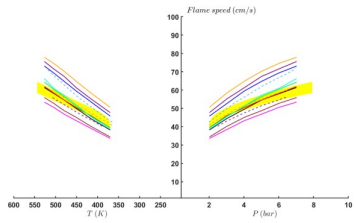

Figure 3.2: Laminar flame speeds at p_0=1 bar, T_0=296.8K, φ = 1.3, 49% Ar and 21% He

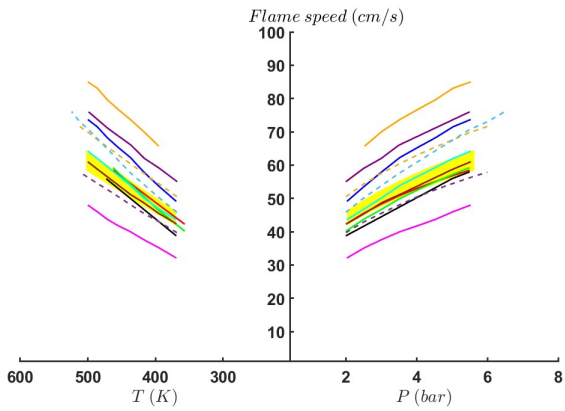

Figure 3.3: Laminar flame speeds at p_0=1 bar, T_0=296.2K, φ = 0.8, 49% Ar and 21% He

Figure 3.1 depicts the flame speed at φ=1.3, p_0=4 bar and T_0=302 K with a diluent mixture of 21% Ar and 49% He. Figure 3.2 represents the flame speed at φ=1.3, P_0=1 bar and T_0=296.8 K and Figure 3.3 represents the flame speed at φ=0.8, p_0=1 bar and T_0=296.2 K. Both the cases use the same diluent mixture: 49% Ar and 21% He. The flame speeds of the lean fuel-air ratio case, φ=0.8 higher than that of the rich case, φ=1.3. The y-axis represents the flame speed whereas the x-axis is split as temperature and pressure. This is done as the flame speed is a function of both pressure and temperature which evolves isotropically and isentropically during the combustion process. On analysing all the cases, it was concluded that both Nakamura and Stagni can predict the flame speed closest to the experimental values. It was seen that Mathieu and Otomo underestimated the values in all cases and on the other hand, Dagaut, Klippenstein and Zhang overestimated the values for all the cases. Modified Okafor predicted the values well within the experimental range for low pressure and rich conditions, whereas, for the other cases, it overestimated the values as well. A brief assessment was made on the specific rate constant, k used by the different schemes and it was seen that they didn't superimpose perfectly on each other probably explaining the difference in the performance. Figure 3.4 shows a comparison of k of $NH_3 + NH \rightleftharpoons NH_2 + H_2$ for two of the schemes- Klippenstein (which over predicts the flame speed) and Nakamura (which is within the experimental flame speed). From the work done by Alturaifi et al. [112], it was seen that on updating the mechanisms with the ammonia pyrolysis equations, there is a significant improvement in achieving flame speeds closer to their experimental reference. The experimental flame speeds along with the flame speeds from Nakamura and Stagni for all the cases are provided in Annex A. Since the study mainly focuses on 3 mechanisms, the following legend is maintained for convenience: red represents Stagni, black represents Nakamura and green represents Shrestha.

3.2 Sensitivity analyses

Sensitivity analyses were performed on a few mechanisms to understand the behaviour and to highlight the key reactions. It was seen that the most dominant reaction irrespective of the mechanism and the initial conditions are $O_2 + H \rightleftharpoons O + OH$. It is interesting to note that the sensitivity coefficient on the flow rate for the reactions for all the schemes is quite different even though the rate constant, k is quite similar. On comparing the rate constants of this reaction $O_2 + H \rightleftharpoons O + OH$ for Klippenstein and Nakamura and the flame speeds it can be confirmed that the discrepancy in the magnitude of flame speeds does not arise from the small difference in values of the k. The vast difference in the flame speeds for different mechanisms may be attributed to the global summation effect of those reactions that do not fall under the top 10 important reactions. Since Nakamura and Stagni estimate the flame speeds closer to the experimental results, a deeper study has been made on them.

Figures 3.5a, 3.5b and figures 3.6a, 3.6b depict the sensitivity analyses for Nakamura and Stagni mechanisms at $\varphi = 0.8$ and $\varphi = 1.1$ for an initial pressure of 1 bar and a diluent mixture of 49% Ar and 21% He respectively. Figures 3.7a, 3.7b represent the sensitivity analyses for Nakamura and Stagni mechanisms respectively at $\varphi = 1.1$, p_0=3 bar with a diluent mixture of 21% Ar and 49%

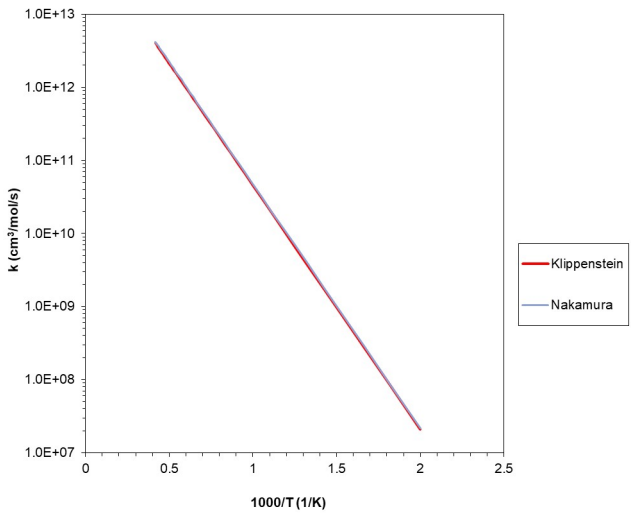

Figure 3.4: Comparison of specific rate constant, k of $NH_3 + NH \rightleftharpoons NH_2 + H_2$ over inverse of temperature for Nakamura (predicts flame speed within the experimental range) and Klippenstein (over-predicts the flame speed)

He whereas figures 3.8a, 3.8b represent the analyses at $\varphi = 1.1$, p_0=4 bar and a diluent mixture of 70% He. Figures 3.9a, 3.9b and figures 3.10a, 3.10b display the sensitivity results at $\varphi = 1.3$ for a p_0=2 bar with a diluent mixture of 21% Ar and 49% He and for a p_0=4 bar with a diluent mixture of 70% He respectively. The analyses illustrate the use of different equivalence ratios, initial pressures and diluent mixtures. The sensitivity analyses for the remaining conditions are provided under the annexe section: A.

It is interesting to note that even though the flame speed predicted by Nakamura and Stagni is quite close, the top 10 important reactions are not exactly the same. The two common reactions apart from the dominant reaction are: $HNO + H \rightleftharpoons NO + H_2$ and $NH_2 + NO \rightleftharpoons NNH + OH$. It is noticed that the reaction $H_2 + O \rightleftharpoons H + OH$ exists within the top 10 important reactions in all cases for both mechanisms except for the lean cases of Nakamura. The rich cases for both the mechanisms witnessed another 2 common reactions: $NH_2 + H \rightleftharpoons NH + H_2$ and $NH_2 + O \rightleftharpoons HNO + H$. A standard set of reactions is noted for each equivalence ratio apart from the above-stated common reactions irrespective of the initial pressure except for $H + O_2 + (M) \rightleftharpoons HO_2 + (M)$ which is found only for those with an initial pressure of 2 bar or more. However, none of the stated reactions plays a role as significant as the $O_2 + H \rightleftharpoons O + OH$ reaction does. Also, from the sensitivity analysis charts it can be seen that the flame speed is not highly sensitive to pressure. The sensitivity analyses show that these mechanisms predict a weak dependence of flame speed on pressure. On comparing with methane flames [16], the recombination reaction, $CH_3 + H \rightleftharpoons CH_4$ is one of the main reactions which becomes more sensitive at a higher pressure and equivalence ratio. The equivalent recombination reaction in ammonia flames, $NH_2 + H \rightleftharpoons NH_3$ is not as sensitive as it is for methane flames. Indeed, the mass burning rate is a parameter that indi-

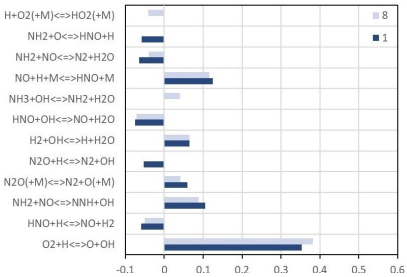

(a) Nakamura

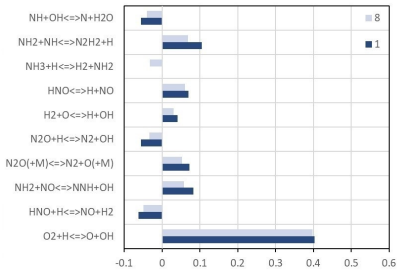

(b) Stagni

Figure 3.5: Sensitivity analyses at p_0=1 bar, φ = 0.8, 49% Ar and 21% He with the minimum pressure at 1 bar (dark blue) and the maximum at 8 bar (light blue)

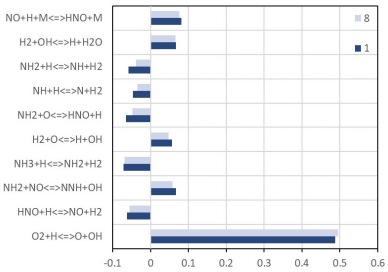

(a) Nakamura

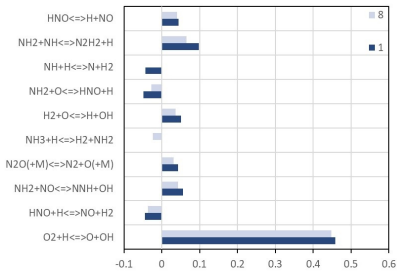

(b) Stagni

Figure 3.6: Sensitivity analyses at p_0=1 bar, φ = 1.1, 49% Ar and 21% He with the minimum pressure at 1 bar (dark blue) and the maximum at 8 bar (light blue)

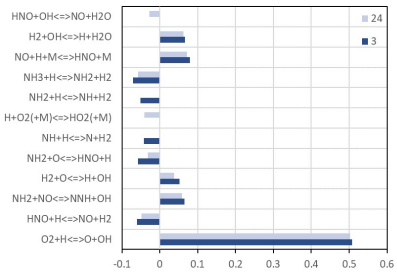

(a) Nakamura

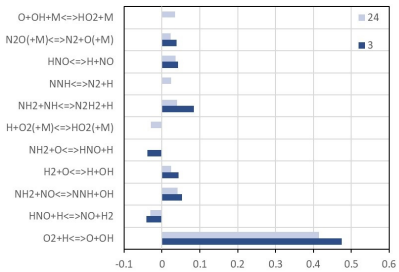

(b) Stagni

Figure 3.7: Sensitivity analyses at p_0=3 bar, φ = 1.1, 21% Ar and 49% He with the minimum pressure at 3 bar (dark blue) and the maximum at 24 bar (light blue)

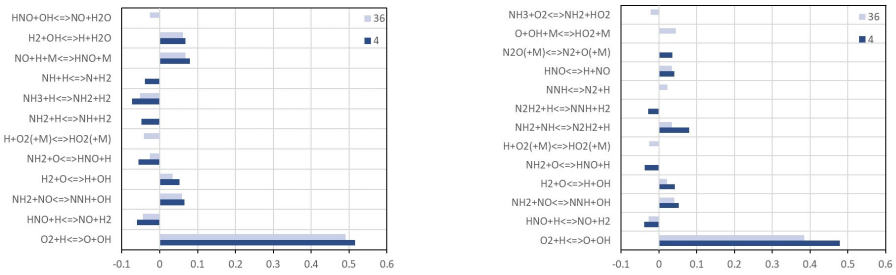

(a) Nakamura (b) Stagni

Figure 3.8: Sensitivity analyses at p_0=4 bar, φ = 1.1, 70% He with the minimum pressure at 4 bar (dark blue) and the maximum at 36 bar (light blue)

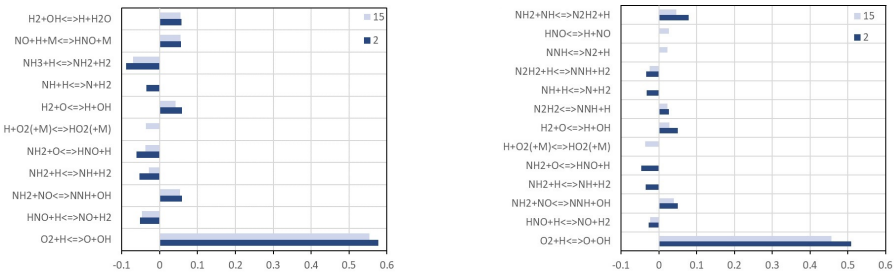

(a) Nakamura (b) Stagni

Figure 3.9: Sensitivity analyses at p_0=2 bar, φ = 1.3, 21% Ar and 49% He with the minimum pressure at 2 bar (dark blue) and the maximum at 15 bar (light blue)

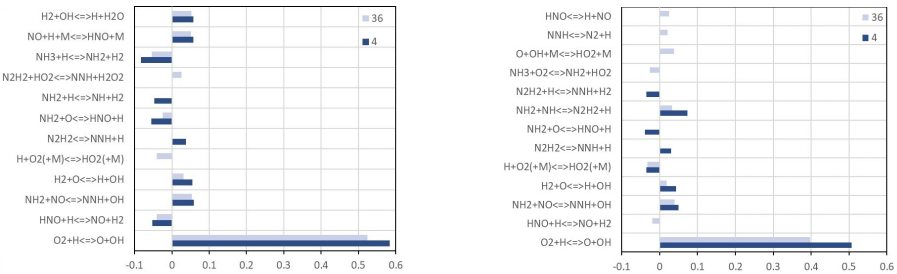

(a) Nakamura (b) Stagni

Figure 3.10: Sensitivity analyses at p_0=4 bar, φ = 1.3, 70% He with the minimum pressure at 4 bar (dark blue) and the maximum at 36 bar (light blue)

cates the reactivity. It increases as both the pressure and temperature increase for both ammonia and methane flames. It is known that when the pressure increases, the H radicals produced in the methane flames are more efficiently consumed leading to a decrease in flame speed. Here, to assess for ammonia flames, it may not be easy to conclude the effect of the recombination reaction as the pressure and temperature increase simultaneously. To evaluate this effect, isothermal and isobaric sensitivity analyses have been carried out with one of the cases represented in the supplementary document. It is seen that $O_2 + H \rightleftharpoons O + OH$ is indeed the most sensitive reaction and the recombination reaction is not as sensitive as compared to the case of the methane flames. The dominance of the driving reaction whose rate constant is pressure-independent and the absence of the equivalent sensitive recombination reaction can possibly explain the ability of all the mechanisms to produce the experimental trend invariably.

Figures 3.1 and 3.2 represent the flame speed variation over pressure and temperature for a low-pressure and a high-pressure initial condition respectively. As shown in these figures, irrespective of a high-pressure and a low-pressure initial condition, it can be seen that the flame speed variation over a pressure difference of 30 and 6 bar are translated as a variation of about 180 K in the temperature scale. In other words, the flame speed change is much higher when the temperature changes by a small amount as compared to a variation in pressure. The temperature increase is higher at the beginning of the compression and this effect decreases at higher pressure. All of these suggest that the combustion of ammonia is more temperature-sensitive rather than pressure-sensitive, thereby implying that the mechanisms may be temperature-driven and not pressure-driven. In order to understand the working of these mechanisms further study has been made. Chapter 4 gives a more detailed study of this aspect.

CHAPTER 4

CHAPTER 4

In order to understand the working of these mechanisms further study has been done. This chapter focuses on some case studies to de-couple the pressure and temperature to understand the individual effects on flame speed. A comparison among the three chosen mechanisms: Shrestha, Nakamura and Stagni is also done to see how each of these mechanisms behaves. Similar studies were done for different bath gases to see their influence.

4.1 Isotherms and isobars

4.1.1 Temperature and pressure effects

Figure 4.1a depicts the variation of flame speed overpressure at T=300 K and Figure 4.1b over temperature at p=1 bar for 3 selected mechanisms: Nakamura, Stagni and Shrestha for $\varphi = 0.8$, 1.1 and 1.3 at a diluent mixture of 49% Ar and 21% He. Isotherms were plotted at T=300 K and at T=500 K and isobars were plotted for p=1 bar and p=3 bar. Similar results were obtained for both conditions. Isotherms at T=500 K and isobars at p=3 bar are shown in Figure 4.2a and Figure 4.2b. It is important to note that the flame speed axis range for the isobars is 4 times the range of the isotherms. It can be seen that as the pressure increases, the flame speed does not vary much. The drastic change in the flame speed is between 1-5 bar for all the mechanisms. As for the case of flame speed variation over the temperature, it is seen that the flame speed increases with temperature and the change is prominent at a higher temperature. This essentially proves that the mechanisms are indeed driven by temperature. On evaluating the performance of the 3 mechanisms, it can be said that the temperature effect is the same in the 3 mechanisms. Figure 4.1a and Figure 4.2a suggest that the pressure effect is slightly more important in Stagni when compared to the other 2 mechanisms and the least in Shrestha.

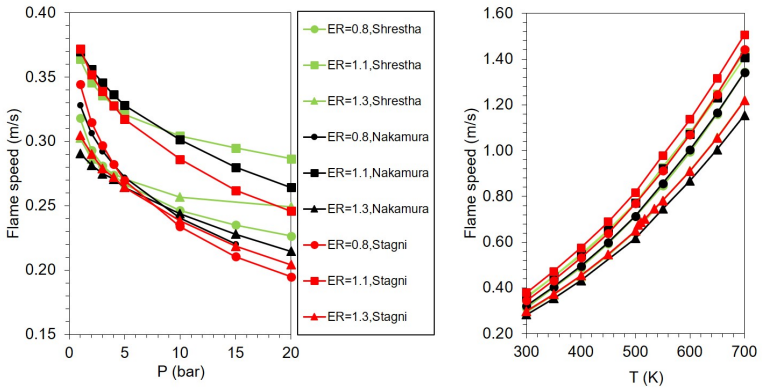

(a) Isothermal plots at T=300 K (b) Isobaric plots at p=1 bar

Figure 4.1: Comparison study of Nakamura, Stagni and Shrestha for $\varphi = 0.8$, 1.1 and 1.3 at a diluent mixture of 49% Ar and 21% He with isothermal plots at T=300 K and isobaric plots at p=1 bar, circles represent $\varphi = 0.8$, squares represent $\varphi = 1.1$ and triangles represent $\varphi = 1.3$ whereas the colours green, black and red represent the mechanisms of Shrestha, Nakamura and Stagni respectively.

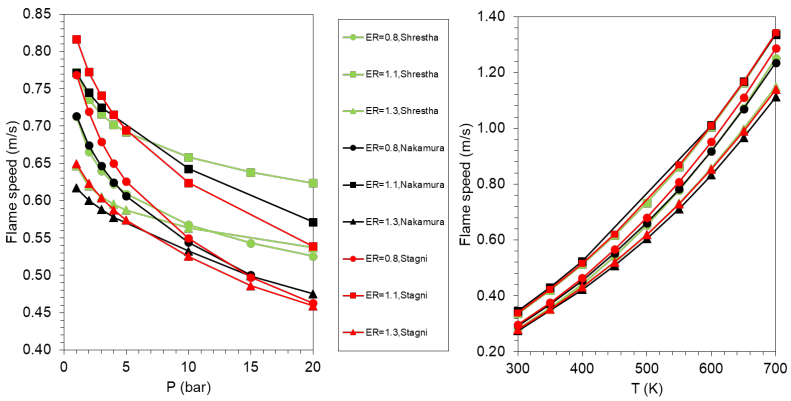

(a) Isothermal plots at T=500 K (b) Isobaric plots at p=3 bar

Figure 4.2: Comparison study of Nakamura, Stagni and Shrestha for $\varphi = 0.8$, 1.1 and 1.3 at a diluent mixture of 49% Ar and 21% He with isothermal plots at T=500 K and isobaric plots at p=3 bar, circles represent $\varphi = 0.8$, squares represent $\varphi = 1.1$ and triangles represent $\varphi = 1.3$ whereas the colours green, black and red represent the mechanisms of Shrestha, Nakamura and Stagni respectively.

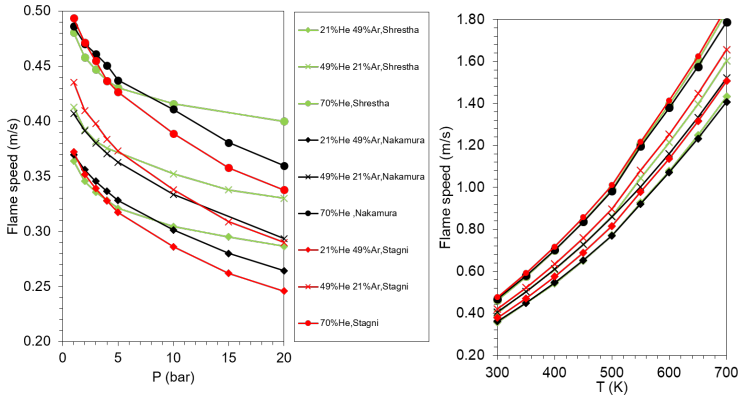

(a) Isothermal plots at T=300 K (b) Isobaric plots at p=1 bar

Figure 4.3: Comparison study of Nakamura, Stagni and Shrestha for $\varphi = 1.1$ for different bath gases compositions, circles represent 70% He with isothermal plots at T=300 K and isobaric plots at p=1 bar, crosses represent 49% He and 21% Ar and diamonds represent 21% He and 49% Ar whereas the colours green, black and red represent the mechanisms of Shrestha, Nakamura and Stagni respectively.

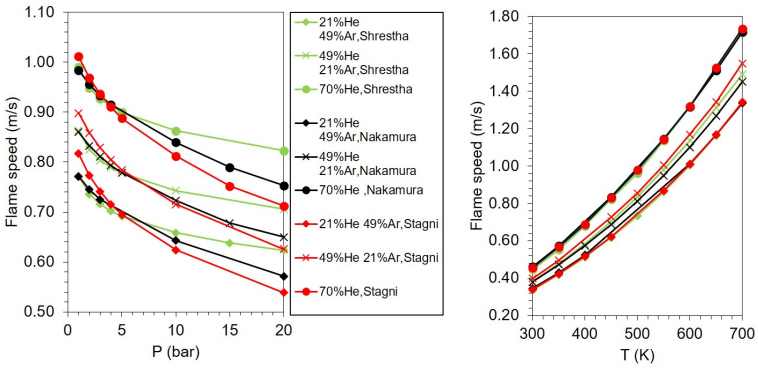

(a) Isothermal plots at T=500 K (b) Isobaric plots at p=3 bar

Figure 4.4: Comparison study of Nakamura, Stagni and Shrestha for $\varphi = 1.1$ for different bath gases compositions, circles represent 70% He with isothermal plots at T=500 K and isobaric plots at p=3 bar, crosses represent 49% He and 21% Ar and diamonds represent 21% He and 49% Ar whereas the colours green, black and red represent the mechanisms of Shrestha, Nakamura and Stagni respectively.

4.1.2 Bath gases effects

The effect of the bath gases is studied and is displayed in figures 4.4a, 4.4b, 4.3a and 4.3b. Isotherms at T=300 K and 500 K and isobars at p=1 bar and 3 bar gave similar results. Isothermal plots at T=300 K and T=500 K

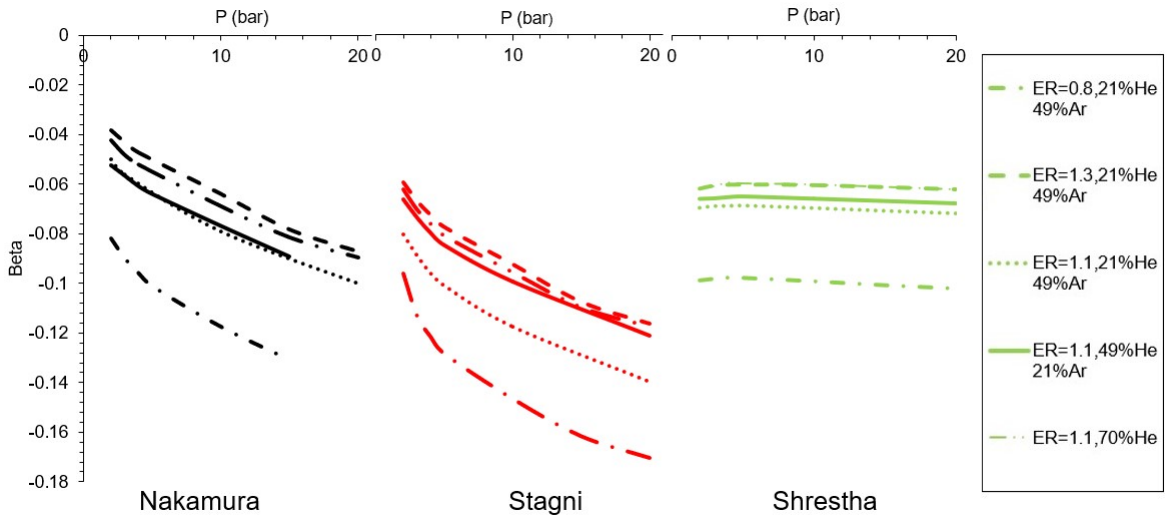

Figure 4.5: Beta trends from isotherms at T=500 K calculated using p_0=1 bar, T_0= 500 K and the corresponding flame speed depending on the equivalence ratio and the diluent mixture. φ=0.8, 21% He 49% Ar is represented by dash-dot, φ=1.3, 21% He 49% Ar by a dash, φ=1.1, 21% He 49% Ar by round dot, φ=1.1, 49% He 21% Ar by solid and φ=1.1, 70% He by long dash-dot-dot and the colours black, red and green represent Nakamura, Stagni and Shrestha respectively.

are displayed in Figure 4.3a and Figure 4.4a respectively and isobaric plots at P=1 bar and P=3 bar are shown in Figure 4.3b and Figure 4.4b. It may be concluded that for the Shrestha mechanism, the variation of the flame speed with pressure is independent of the bath gas composition while both Nakamura and Stagni show a slight dependence.

4.1.3 Alpha and beta

The pressure and temperature dependencies may be expressed as given in the equation 2.3 using a reference flame speed and the corresponding conditions if the exponential factors α and β are known.

$$\frac{S_u}{S_u^o} = (\frac{T_u}{T_u^o})^{\alpha}(\frac{P_u}{P_u^o})^{\beta} \tag{4.1}$$

Using the isothermal and isobaric curves, the values for α and β are estimated. It is observed that α varies linearly with the temperature for all the 3 mechanisms and the value ranges between 1.5 and 2. This range of value is quite common to most of the fuels [113]. β variation for Nakamura and Stagni is quadratic whereas it is almost a constant for Shrestha as seen in Figure 4.5. Beta trends represented in Figure 4.5 are calculated using p_0=1 bar, T_0= 500 K and the corresponding flame speed depending on the equivalence ratio and the diluent mixture. The values of β lie between -0.04 and -0.17 which is much lower than most of the fuels [113]. The low value of beta results from pressure-

independent behaviour. It is worth emphasising that the pressure independence increases with an increase in pressure.

4.2 Alpha and beta values for the experiment and numerical flame speeds

From the experimental test conditions, it is possible to have at least two conditions with the same equivalence ratio, initial temperature and diluent mixture but with a different initial pressure giving rise to two (p, T) pairs. A certain range of pressure is common to both conditions but the corresponding temperatures are different due to the initial conditions. The flame speeds can be obtained for two different temperatures at an isobaric condition. Considering one of the flame speed curves (here, the flame speed corresponding to the initial condition with the lower pressure) as the reference curve, an estimation of α can be made using equation 4.1 and can be optimised to get the most precise value. A similar process can be used to estimate the β values from flame speeds corresponding to two different pressures at isothermal conditions.

The values of α and β from Nakamura and Stagni lie within the experiment range. The values of β range between -0.07 to -0.21 and the values of α range between 1.5 and 1.92 depending on the initial conditions. Both α and β are not constant values, therefore an estimation of the flame speed using equation 2.3 can be made by interpolating the values within the given range for the given set of conditions. It can be intuitively said that having a low β value is advantageous as pressure oscillations would have fewer effects on flame stabilization in systems like gas turbines.

CONCLUSION

Experiments to measure flame speeds corresponding to the conditions encountered in spark-ignition engines and gas turbines have been performed. The study was done for 3 different equivalence ratios: 0.8, 1.1 and 1.3 at an initial temperature of 300 K and an initial pressure ranging from 1 to 4 bar. The data available in the literature gives the flame speeds for a maximum pressure of 10 bar and a temperature of 473 K. From this study, the laminar flame speeds for a pressure of 30 bar and a temperature of 585 K have been obtained. These tests were performed under constant volume conditions which is the most efficient way to obtain a wide range of data for elevated conditions.

A literature study had been made to select the most recent kinetic schemes for ammonia combustion. These schemes have been evaluated for the same conditions as that of the experiments. It was seen that the chosen schemes could produce the experimental trend- an increase in flame speed with an isotropic increase of pressure and temperature for all the conditions. On performing sensitivity analyses, it was understood that the most dominant reaction is $O_2 + H \rightleftharpoons O + OH$. Despite the high sensitivity of this reaction and the rate constant of this reaction being similar for all mechanisms, only 4 mechanisms: Shrestha, Nakamura, Modified Okafor and Stagni could predict the flame speeds with the $\pm$ 5 % error bar of the experimental flame speeds. The recombination reaction of the ammonia flames is pressure insensitive. In order to understand the working of the mechanisms, various simulations were performed at isobaric and isothermal conditions. The results of these simulations prove that the mechanisms are temperature-driven and not pressure-driven as the change in flame speed for a small increase in temperature is much higher than the change in flame speed obtained from the same increase in pressure. The maximum influence of pressure is seen only from 1-5 bar after which the flame speeds do not vary a lot. The increase in the flame speed is attributed only to the increase of temperature which promotes chemical reactivity. The impact of adding the bath gases has been noted for some of the mechanisms. The change in the flame speed response to pressure for Shrestha seems to have a lesser effect from the bath gas composition whereas Stagni and Nakamura seem to be influenced by the constituents of the bath gases.

A range of exponential factors α and β required to calculate the flame

speeds at a given pressure and temperature using a reference condition was determined. It is interesting to note that β, the exponential factor for the pressure is much smaller than most of the fuels emphasising the pressure independency behaviour. This implies that ammonia is an ideal fuel for spark-ignition engines and gas turbines since pressure oscillations would have limited effects on flame speed.

Finally, from the data generated, a 3D map of flame speed as a function of pressure and temperature using a fit proposed by [11] can be done. As an example Figure 4.6 3 represents the flame speeds at $\phi = 1.1$, diluent mixture of 49% He and 21% Ar, $T_0 = 300$ K, $p_0 = 1$, 2, and 3 bar as a function of p and T. The experimental data are the blue, red, and green thick lines in the volume. The blue, red, and green thin lines on the lower plane are the projections of these experimental data on the (p, T) plane representing the isentropic evolution of pressure and temperature starting from each initial condition. The idea of using this map is that by interpolating data, flame speeds can be obtained for any pressure and temperature for the given gas mixtures without the need of performing new experiments.

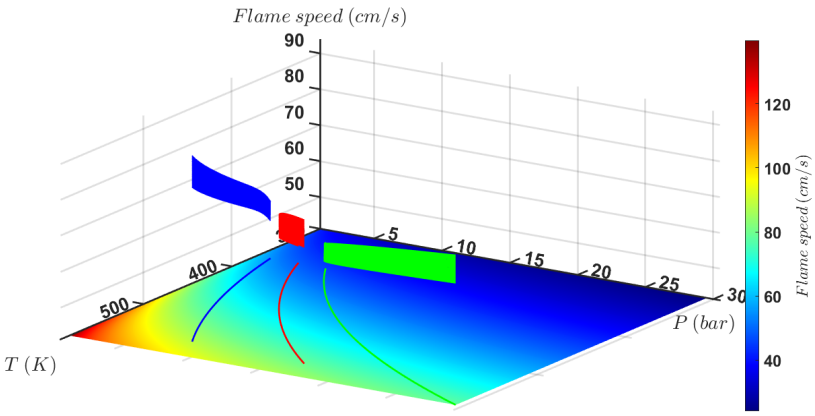

Figure 4.6: Experimental flame speeds of $NH_3/O_2/He/Ar$ mixtures at $\phi = 1.1$, $T_0 = 300$ K, $p_0 = 1$ (blue), 2 (red), and 3 bar (green).

Part II

Inner structure of a stretched premixed flame

INTRODUCTION

From the previous part, it was seen that ammonia/oxygen flame speeds at elevated conditions are on par with conventional fuels. However, it is known that ammonia/air flame speeds at atmospheric conditions are quite low. It is important to know the inner structure of the flame to understand the combustion process better and therefore, to comprehend the influence of various parameters to finally enhance the process. Ammonia/air flames are known to be much thicker than hydrocarbon flames [132]. Part II is an attempt to give an insight to the structure of stretched premixed ammonia/air flames at atmospheric conditions. The parameters that were focussed on to study were the influence of both the equivalence ratio and the curvature on the thickness and reactivity of the flame. This was experimentally achieved by studying the chemiluminescence signature of the important species.

Chapter 5 consists of a brief discussion on the different experimental setups along with the diagnostics used to determine the flame speed for ammonia/air combustion at atmospheric conditions. A glimpse into the literature describing the structure of ammonia flames has also been provided. A review of the chemiluminescence and the curvature effect has been done as well.

Chapter 6 presents a description of the experimental set-up used here. This chapter also discusses the different techniques used here in order to fulfil the set objectives.

Chapter 7 emphasizes the flame thickness and the evaluation of flame speed over a range of equivalence ratios. A comparison of the obtained flame speed with the existing literature data has been provided.

Chapter 8 pinpoints the curvature effects on different species emitted from the flame. A study of the inner structure of the flame for a slightly lean mixture, near stoichiometric conditions and a rich mixture, have been presented here. The chemiluminescence signature of these flames provides a piece of important information on the HRR which has been well noted.

To conclude, a global summary highlighting the importance of the flame thickness and evaluation of other parameters affected by the thickness like flame speed has been provided. Also, the effect of curvature on the chemical reactivity of ammonia/air flames for a given range of equivalence ratios has been summarised.

CHAPTER 5

CHAPTER 5

As mentioned in the introduction, it is important to study the flame structure and other characteristics to understand the combustion process better and to enhance the performance in energy-based applications. Determining the flame speed is important as it is one of the basic parameters which is used for assessing the characteristics of fuel and engine sizing. It is known that ammonia-air flames have very low flame speed values as reported in the literature. Flame speed is generally evaluated for an isotherm that is as close as possible to the fresh gas's temperature. The error associated with finding the values of the flame speed by not choosing the right isotherm can be large which can lead to huge errors in the assessment of other parameters based on the fresh gas isotherm. The laminar flame speed, S_L, is defined as the propagation speed relative to the unburnt mixture of a steady, laminar, 1D, planar, stretch-free, and adiabatic flame. Hence, the required isotherm is the one at the fresh gas surface for which defining the flame thickness is needed.

5.1 Experiments and optical diagnostics for flame speeds in ammonia combustion

There are several methods to experimentally determine flame speed. The most common method is the closed spherical vessel. Figure 5.1 shows the different experimental methods that are found in literature along with their pressure and temperature range. Depending on the objective of the experiment, the apt technique is used to carry out the experiment. For example, in Part I, the constant volume chamber was used as the target was to hit high temperature and pressure conditions. The constant pressure chamber is used to determine flame speeds at a constant high pressure. For both these methods, the detection of the flame front can be done by following the chemiluminescent part of the flame or by using the Schlieren method. Stagnation flow is used for a lower pressure and temperature range. Sampling probes can be used to determine the temperature at different distances. The heat flux burner is used for a narrower

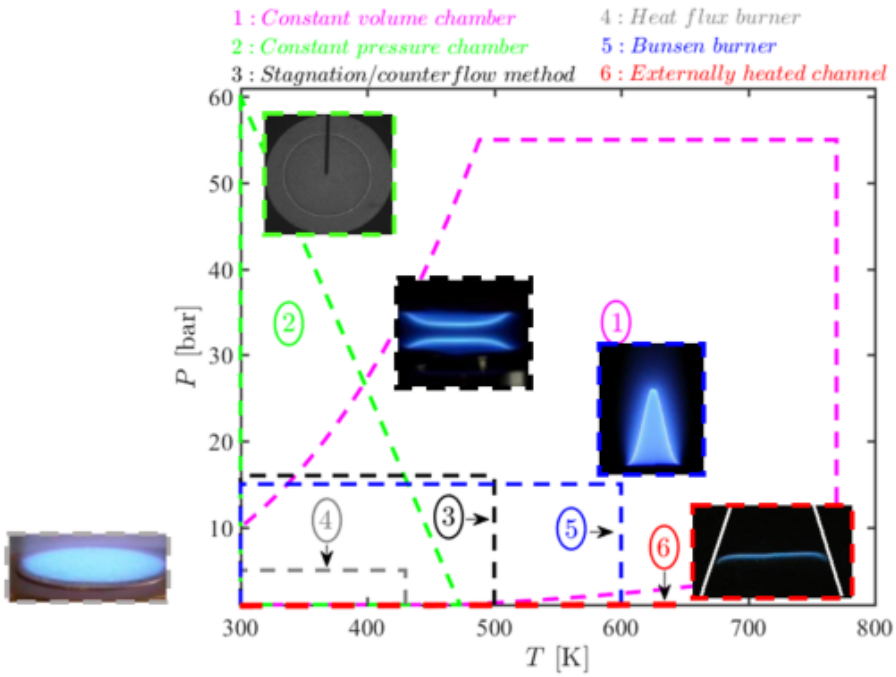

Figure 5.1: Different experimental techniques used to study flames along with the pressure and temperature range.

range of pressure and temperature. Thermocouples are used to measure the temperature difference on different parts of the plate. Using this temperature gradient, flame speeds can be found. The externally heated channel method is used for a wide range of temperature conditions. Flame speeds are computed using the temperature and the flow. The Bunsen burner is used for a slightly lower temperature range but for a higher pressure range. PIV can be used to trace particles, and so the flow velocity can be obtained.

5.2 Chemiluminescence signature of ammonia flames

Chemiluminescence is the emission of light, usually in the visible or near-infrared spectral region, as a result of an excited electronic molecular state, formed in a chemical reaction, returning to the ground state. It is often observed during the combustion process when species get excited and return to the ground state often giving a hue to the flames. In combustion, chemiluminescence is an important diagnostic tool which is often deployed to give the heat release rate position. Another reason, why these excited species are of interest from the heat release rate point of view is because it can be directly used in simulations which implement kinetic models that are based on reactions of several excited and non-excited species. Chemiluminescence can be used to study flame properties like equivalence ratio, temperature and concentration of the species. Bedard et al. [114] in their paper give an extended overview of the use of chemiluminescence as a diagnostic tool in combustion.

From the emission spectra of ammonia-air flames, NH* and NH_2* have been recognized as species of interest to study. Extensive work on the chemiluminescence of species in ammonia/air and other blended fuels [115–117] can be found in the literature. Pugh et al. [118] used chemiluminescence in both NH_3/air and NH_3/H_2/air to quantify NO in a combustor. Zhu et al. [119] obtained OH* to quantify NO in NH_3/H_2/air flames. NH_2* chemiluminescence has also been used to study NO emissions in plasma-assisted ammonia combustion [120]. Wiseman et al. [121] showed that OH* can be used to compare the flame topology before the blowout. Chemiluminescence from various species [12] was used to study radical formation in high-temperature reactions for NH_3/CH_4 blends in swirl flows both experimentally and numerically and also to determine the location of the highest heat release rate. Liu et al. [76] also used chemiluminescence to characterize the heat release rate. The chemiluminescence of selected species may be essential to characterize the flame stability and heat release. To our knowledge, no information on HRR and the curvature effect on species via chemiluminescence is available for ammonia/air flames.

5.3 Studies of stretch effects in ammonia flames

Stretch effects can be classified into two components: strain rates and curvature effects [122]. It is important to know these effects on the flame as this changes the flame surface area and hence enhances or de-enhances reactivity depending on the stretch being negative or positive. Also, flame properties like flame speeds are not the same for stretched and unstretched flames. Hence, it is important to characterize these effects. Often quantities like Markstein length and Markstein number are used to parametrize stretch effects.

DNS studies [123] were performed to study the curvature effects on NO formation in $NH_3/H_2/N_2$/air flames. There is a vast study on stretch effects and strain rates. Studies on extinction stretch rate in both premixed and non-premixed NH_3/CH_4 flames were done experimentally using OH and NO PLIF and numerically using four of the mechanisms existing in literature by Colson et al. [124]. Xiao et al. [125] studied strain rates for ammonia/methane flames and reported that the strain rate at extinction enhanced upon the addition of methane in the fuel mixtures. Lee et al [83] in their work use the Markstein number to quantify the stretch effect in hydrogen-added ammonia air flames. They reported that the general characteristics of unstable behaviour ($Ma < 0$) at fuel-lean conditions and stable behaviour ($Ma > 0$) at fuel-rich conditions are consistent with conventional explanations of flame stability. In contrast to the consistent increase in S_L with hydrogen substitution, the dependency of Ma on the nature and extent of substitution varies substantially.

5.4 Literature on ammonia flame structure

Studying the flame structure gives an insight into the different species that exist which gives information on reactivity. Understanding the position of these species and how these species react upon a perturbation gives direct knowledge of its influence on reactivity. Hence, it is important to understand the structure of the flame to enhance its properties of the flame to promote combustion.

Rocha et al. [126] gave a joint experimental and DNS study on premixed NH_3/CH_4 flames to characterize the structure of the blended flame accommodating the local flame stretch. NH and NO profiles were measured using PLIF. The molecular beam mass spectroscopy was used by Duynslaegher et al. [93] to study the structure of $NH_3/H_2/Ar/O_2$ flames along with the stretch effects. Numerical simulations were also performed to compare with their experimental study. Premixed NH_3/air flame structure was investigated [127] using LIF to obtain profiles of OH, NH, and NO which were used to evaluate four kinetic models. Wolfhard and Parker [128] carried out a spectroscopic investigation into the structure of flat diffusion ammonia-oxygen flame. Xiao et al. [125] studied the structure of ammonia/methane flame in a stagnation counter set-up and analysed various profiles like emissions of species to understand the reactions and the chemistry behind it. Lee et al [83] did a similar study with hydrogen-blended ammonia flames.

There are hardly any studies on the inner structure of ammonia-air flames using chemiluminescence. The work presented here comprises the use of chemiluminescence to study the curvature effect of different excited species and to understand the structure of ammonia-air flames at atmospheric conditions along with flame speeds at the same conditions for different equivalence ratios on a Bunsen burner.

CHAPTER 6

CHAPTER 6

This chapter describes the experimental setup and the diagnostics used for the different measurements that have been carried out.

6.1 The experimental set-up

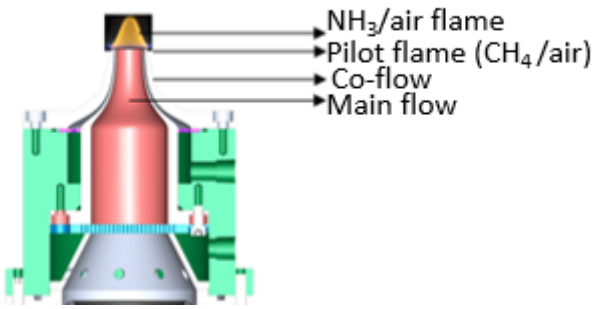

Figure 6.1: Sketch of the Bunsen burner set-up.

A Bunsen burner was used to carry out the experiments as shown in Figure6.1. The diameter of the burner outlet is 15 mm. Since a premixed mixture of ammonia/air is used for the study here which is a weak flame and cannot sustain without a co-flow or a pilot flame for stabilizing the main flame. Several studies [118,129] show the use of pilot flame to stabilise the main flame. Here, a close to a stoichiometric mixture of methane/air is used as the pilot flame. The flow of both methane and air are controlled by rotameters whose flow are set to 0.01 L/min and 0.1 L/min. The flow of ammonia and air are controlled by Brooks mass flow controllers. The mass flow controller for air ranged between 0-30 NL/min whereas for ammonia it ranged between 0-3 NL/min. The mass flow controllers required for ammonia are different from the ones used by

conventional fuels as ammonia is highly incompatible with some materials like brass, copper etc. These mass flow meters are operated using software called Supervision V12. Special pipes that are compatible with ammonia were used for the feed. This helped to eliminate the problem of corrosion of pipes. Each of the ammonia pipes was linked to a pipe filled with nitrogen gas to flush out the ammonia remains in the pipe after every experiment thereby, elongating the lifespan of these pipes. The burner was placed inside a cabin and exhaust was used to evacuate unburnt ammonia from this cabin. The mean velocity of the fresh gases at the exit of the burner ranged from 0.18 to 0.2 m/s. The fresh gas mixture is injected through the sides of the burner which further flows through a 5 mm thick aluminium grid to obtain a laminar flow. This reactive flow is ignited at the exit of the burner by the presence of the pilot flame. The pilot flame emits a power of 55 W which is required to stabilize the ammonia/air flame. The power emitted by the main flame is between 83 and 117 W. Although, the power emitted by the pilot flame in the present configuration is about half of what is emitted by the main flame, it can be safe to say that this power has no direct influence on the characteristics of the main flame as tests were done where the flow of the pilot flame was changed, therefore the power of the pilot flame was varied. It was seen that changing the power of the pilot flame did not result in a change in any of the behaviour of the parameters used in this study. Moreover, these studies are carried out away from the base of the main flame. The heat losses to the burner are not considered for the same reason. The radiation effects may occur in the burnt gases from the water vapour. For this study, these effects are not of concern as the region of interest in restricted to the initial part of the reaction zone which is away from the burnt gases.

It was seen that the flame was subjugated to a buoyancy-driven flickering. There are literature sources [130] that show these effects can be reduced by using a chimney. A 150 mm high cylinder with an outer diameter of 120 mm and thickness of 1 mm was mounted at a height of 25 mm from the burner exit which acted as a chimney and helped to reduce the entrainment of air. Figure 6.2a and Figure 6.2b depict the buoyancy-driven flame flickering and Figure 6.2c shows that using a chimney helps to reduce this effect.

6.1.1 The PIV set-up

The flame speed was determined using a PIV setup. The airflow is fed through a seeding system, consisting of an atomizer that produces droplets of size 1 µm. Di-ethyl-hexyl-sebacate (DEHS) which evaporates at 525 K was used to seed the fresh gases with droplets. The PIV setup consists of a laser source directed to a dichroic mirror kept at 45°. The light source used is a continuous Coherent Verdi G20 Laser of 532 nm. A laser power of 5 W is used. The light from this source is reflected at the mirror at a right angle penetrating through a cylindrical lens and then onto a spherical lens of a focal length, f = 750 mm providing a laser sheet perpendicular to the flame. An iris is used to control the size of the laser sheet projected on the burner to ensure that only the flame is illuminated by the laser. A CMOS high-speed camera (PHANTOM V1611) is used to capture the images and a code written in Python is used to track the particles and provide a velocity field map. A PIV interrogation window size of 32 pix^2 is set initially. Finally, an interrogation window size of 16 pix^2

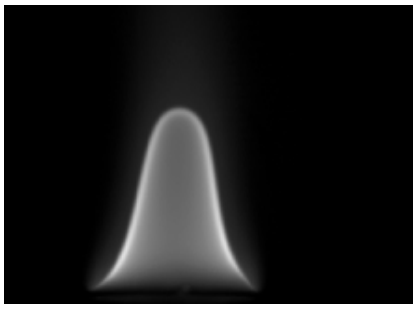

(a) The minimum of flame due to entrainemt of air

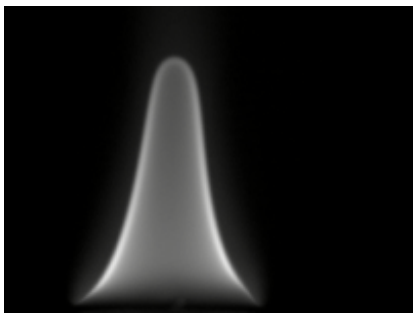

(b) The apex of flame due to entrainemt of air

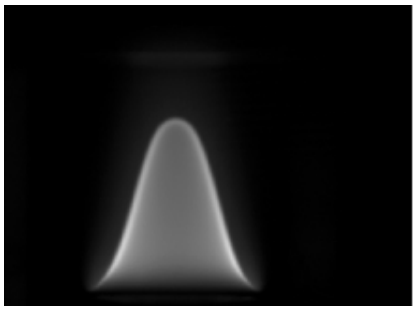

(c) Lower flickering of flame

Figure 6.2: Images of buoyancy-driven flame flickering before and after using the chimney.

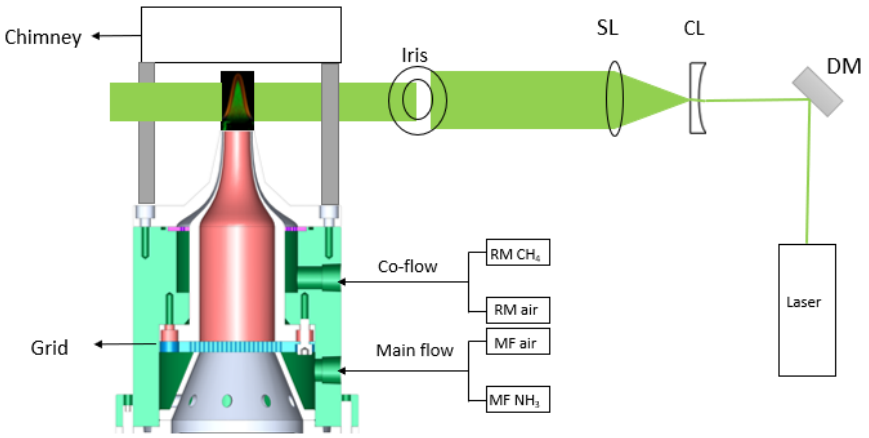

Figure 6.3: Schematic diagram of the experimental set-up along with the PIV set-up. CL: cylindrical lens, SL: spherical lens, DM: dichroic mirror, RM: rotameter, MF: mass flowmeter

with a 50% overlap is used. The conversion factor is 4.56E-2 mm/pix and the camera acquisition rate and the exposure time were set to 10000 fps and 99 µs respectively. Since the flow velocity was very low, every tenth image was chosen to track a droplet and hence, to determine the velocity. The PIV images were mainly used to determine the isotherm close to the fresh gas which is needed to evaluate parameters like flame speed and flame thickness whose definitions depend on the fresh gas isotherm. Figure 6.3 represents the schematic diagram of the set-up.

6.1.2 The chemiluminescence set-up

On studying the emission spectra of ammonia/air flames at stoichiometry, 4 species: OH*, NO*, NH* and NH_2* were identified as species of interest. The orange hue of the flame is attributed to the different peaks at about 600 nm. All of these peaks correspond to NH_2*. Figure 6.4 represents the non-calibrated emission spectra of ammonia/air at stoichiometry. The emission spectrum from the pilot flame has been subtracted from the raw spectrum of the ammonia-air flame and has been represented here. Several of the peaks have been identified using the emission spectra of ammonia flames which were found in the literature [131]. For the current study, NH* and NH_2* have been chosen as the species of interest as these two species have not been well studied.

The inner structure of the flame was determined using chemiluminescence. The filters used for NH* and NH_2* are centred at wavelengths 337 nm and 632 nm respectively with a diameter of 50 mm and a bandpass width of 10 nm. These filters were manufactured by Edmund Optics. The filter is placed in front of the high-speed IRO intensifier which is placed in front of the CMOS camera. The intensifier is used to have maximum sensitivity and to have good image quality. Two different objective lenses were used: a UV lens for NH* and a visible range spectrum lens for NH_2*. An instantaneous shot is used for the study as it was seen that an average flame perturbation of over 200 images is

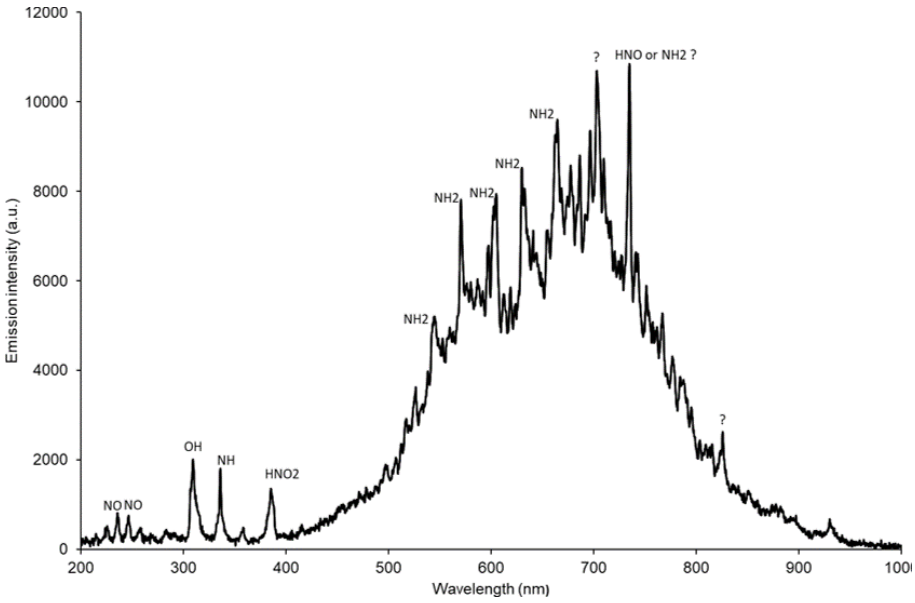

Figure 6.4: Emission spectra for ammonia/air flames at stoichiometry identifying important species. The intensity has not been calibrated. The background illumination and the pilot flame emissions have been subtracted. The emission peaks are not calibrated.

small. The induce error % in thickness is 13% for an exposure time of 200 ms. The conversion factor is 5.76E-2 mm/pix and the camera acquisition rate, and the gate of the intensifier was set to 1000 fps, and 98 ms respectively for NH_2* and 100 fps, and 988 ms respectively for NH*. A higher gate was required as the signal for NH* was much weaker than NH_2*. Figure 8.3 represents the schematic diagram of the chemiluminescence set-up.

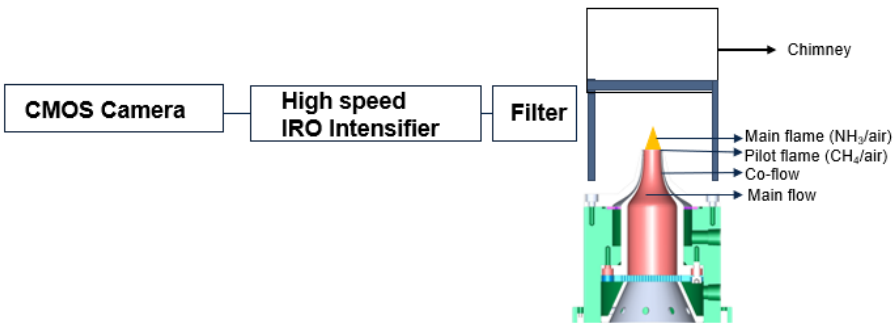

Figure 6.5: Schematic diagram of the experimental set-up for the chemiluminescence study.

6.2 1D simulation

From Part I, it was seen that both Nakamura and Stagni gave flame speeds that were close to the experimental data for all test conditions. The kinetic scheme of Stagni was chosen for the study here. This scheme has 31 species and 203 reactions. The premixed laminar flame speed calculator of Chemkin-Pro was used to simulate 1D unstretched freely propagating flame. The adaptive grid control parameters: CURV and GRAD were set to 0.01. The length of the computational domain used was 2 cm. The maximum number of grid points allowed was fixed at 2000. The species concentration, the temperature profile and the HRR profile as a function of the distance in the computational domain are obtained from these simulations.

CHAPTER 7

CHAPTER 7

This chapter discusses the results obtained using the PIV setup. The importance of the flame thickness and flame speed evaluated on the fresh gas isotherm has been provided here.

7.1 Flame thickness

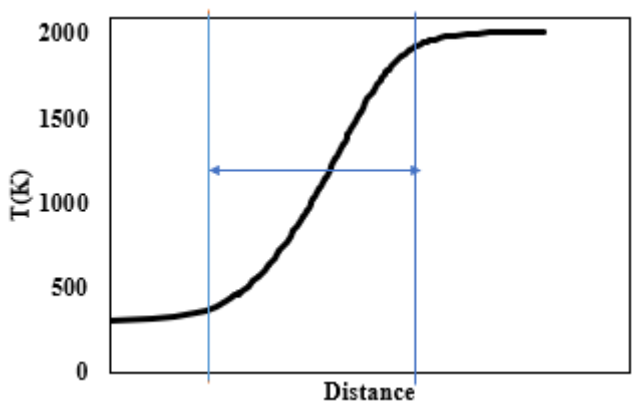

Figure 7.1: Definition of flame thickness.

Ammonia flames are known to be thicker than most flames [132]. One of the definitions of flame thickness is the distance from where the extended tangent meets the unburned fuel temperature, and the combustion products temperature. Figure 7.1 shows the flame thickness in a temperature vs distance profile. The line on the left indicates the fresh gas isotherm after which is the reaction zone, followed by the burnt gas isotherm. At atmospheric conditions, the temperature of fresh gas isotherm is about 500 K.

Figure 7.2 represents a nearly stoichiometric ammonia-air flame using the

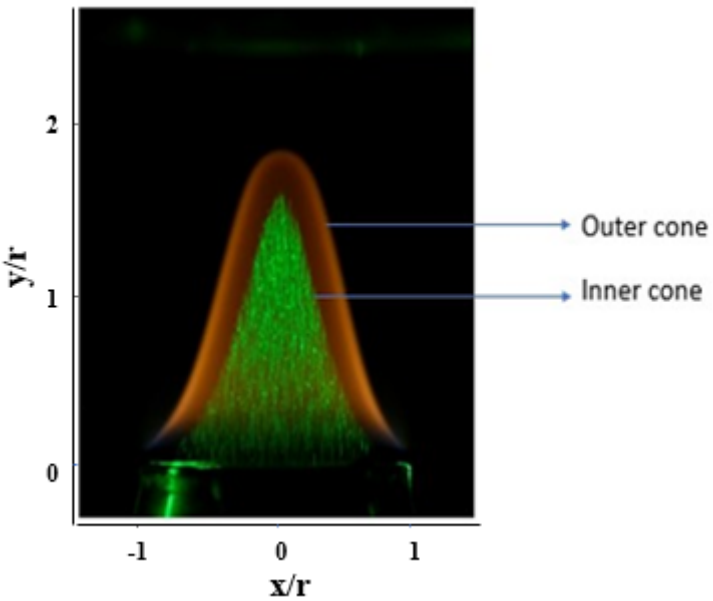

Figure 7.2: Ammonia-air flame at $\varphi = 1.1$ with PIV depicting the thick flame. The inner cone and the outer cone represent the fresh gas surface and the outer flame surface respectively. The camera used to capture this image is NIKON D850 and the exposure time has been set to 250 ms. The x and y axes have been normalized over the radius of the burner axes.

PIV set-up. This image was captured using NIKON D850 with a 180 mm lens and an exposure time set to 250 ms. It can be seen that this flame is much thicker than most hydrocarbon flames. The DEHS droplets are illuminated by the laser. When these droplets reach the 525 K isotherm, they evaporate. Thus, fresh gases are in the inner cone (in green) and the isotherm 525 K appears in Figure 7.2 as the limit between the green and the orange zones. The outermost surface of the flame is referred to as the outer cone in Figure 7.2 and is the limit between the orange and the black zones. The flame thickness, δ, can be defined as the zone between the inner and the outer cone (between the green and the black zones in Figure 7.2). The axes in Figure 7.2 represent the position normalized over the burner radius with the centre of the x-axis pinned at the centre of the burner and the zero of the y-axis at the exit of the burner. The effect of DEHS droplets has been tested and it was seen that the evaporation of these droplets didn't interfere with the parameters used in this study.

7.2 Flame speed determination

The most commonly used method to evaluate flame speed for ammonia combustion available in the literature is by using a closed spherical vessel with Schlieren [80, 84, 86] and by vertical tube with direct imaging [85, 88] Han et al. [48] used the heat-flux burner method to provide the flame speed data whereas Ronney et al. [87] provided the flame speed at microgravity in a closed

spherical vessel with thermocouples.

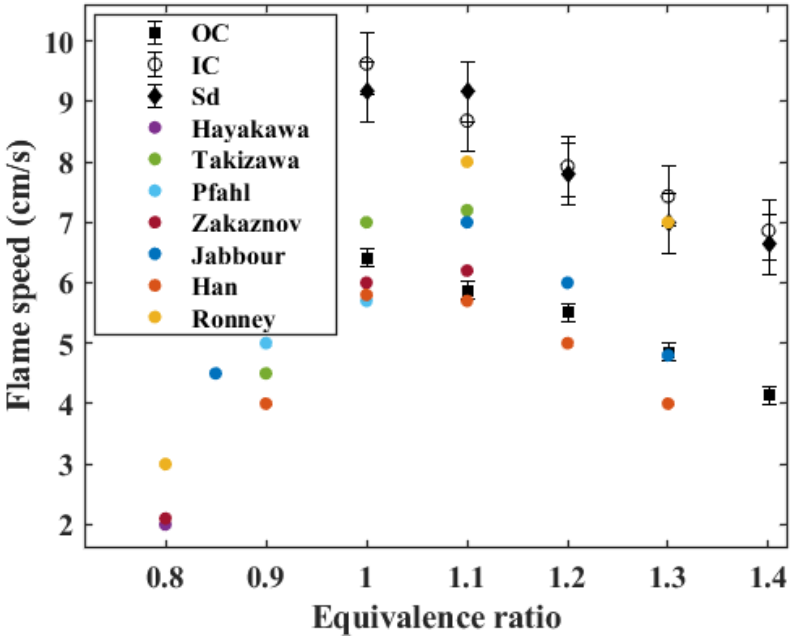

Figure 7.3: Comparison of ammonia-air laminar flame speed at atmospheric conditions available in the literature for different φ . OC (black square) and IC (black circle) represent the flame speed at the outer cone and inner cone and Sd represented by a black diamond is the displacement flame speed.

When the spherical flame method is used, stretch effects must be considered. The unstretched laminar flame speed is obtained by applying the continuity equation to the burning velocity and the flame ball expansion. For this calculation, often the thin flame approximation is imposed i.e. it is assumed that the radii of the unburnt gases and burnt gases at the flame front are the same. Pfahl et al. and Hayakawa et al. demonstrated this in equation 4 of Ref. [86] and Ref. [80] respectively by omitting the surface area in the mass continuity equation. While considering the density of the burnt gases for this equation it is assumed that density remains homogeneous which may be true for thin flames. Tazikawa et al. used equation 1 in Ref. [84] by defining the burnt mass fraction which also depends on the radius chosen. When measurements are done using a thermocouple, the distance chosen for the measurement is directly linked to the isotherm which is used to calculate the flame speed. In the case of the vertical tube method, the outermost visible layer (equivalent to the OC as shown in Figure 7.2) is chosen as the flame front.

The laminar flame speed, S_L, in the case of the Bunsen burner is obtained by applying conservation of mass at the exit of the burner to the inner surface and can be mathematically formulated as:

$$A_b.U_fg.\rho_fg = A_u.S_L.\rho_fg \tag{7.1}$$

where U_{fg} is the fresh gases velocity at the burner outlet, A_b is the exit area

of the burner, ρ_{fg} is the density of the fresh gases and $\mathrm{A_u}$ is the area of the unburnt gas surface. The displacement speed, $\mathrm{S_d}$, is defined as the propagation speed of a flame relative to the fresh gas flow and is given as:

$$S_d = (u - w).n \tag{7.2}$$

where u is the fluid velocity, w is the absolute speed of the flame in a fixed laboratory and n is the flame normal vector oriented towards the fresh gases. Here, w = 0.

As per the definition of the flame speed, the isotherm to be chosen corresponds to the inner cone. The laminar flame speed, $\mathrm{S_L}$, and the displacement speed, $\mathrm{S_d}$, are computed using Equation 7.1 and Equation 7.2. The difference in the flame speed computed at the outer cone (OC) and the inner cone (IC) represented by black squares and circles respectively in Figure fig:flamespeedis around 2-3 cm/s. As shown in Figure fig:flamespeed, on comparing with values given in the literature, it is seen that the flame speeds reported in the literature are closer to the flame speed obtained at the outer cone; far from the fresh gas isotherm. It can also be seen that the displacement speed evaluated at the inner cone which is represented by the black diamond in Figure 7.3 is in congruence with the laminar flame speed at the same surface.

These obtained experimental flame speeds were compared with the flame speeds obtained from simulating the previously chosen 2 kinetic schemes (from Part I) and it was seen that both the schemes predicted the flame speed within the error bars of the experimental flame speed.

CHAPTER 8

CHAPTER 8

This chapter describes the analyses done on the species using the chemiluminescence setup. Inverse able transformations were performed on the raw images using the Basex method to convert the integrated 3D raw image information onto a 2D plane.

8.1 Curvature effects on the species

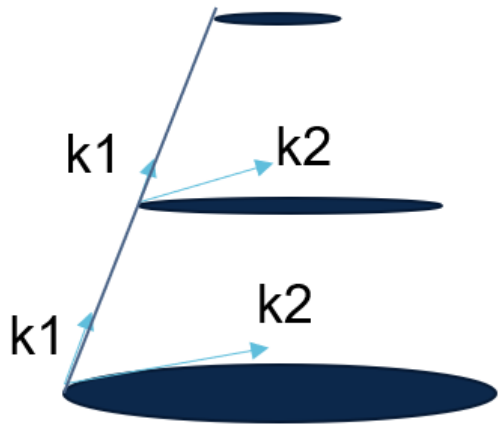

Figure 8.1: Representation of the principal curvatures k1 and k2 in the flame contour. k1 is along the contour and k2 is along the circumferential direction. Negative curvature is defined for a concave flame in the direction of the burnt gas and a positive curvature is defined for a convex flame in the direction of the burnt gas.

Experiments were performed for equivalence ratios between 0.9 and 1.4. As mentioned in [122], stretch effects, K can be decomposed into two components: strain rate,K_{T} and curvature effect, K_{C}. Curvature effect,K_{C} is defined as $2.\mathrm{S_d}.K_{\mathrm{m}}$ where K_{m} is simply the average of two principal curvature: k1 and k2. k2 is the curvature in the circumferential direction whereas k1 is the curvature in the plane. When the flame contour is expressed in terms of cylindrical coordinates with h in the streamwise direction and r in the radial direction. k1 and k2 are mathematically represented as:

$$k1 = \dot{r}\ddot{h} - \ddot{r}\dot{h} \tag{8.1}$$

$$k2 = \frac{\dot{h}}{r} \tag{8.2}$$

where the dot signifies with respect to the curvilinear coordinate s which is expressed as:

$$\int_0^{\tau} \sqrt{\left(\frac{\partial r}{\partial \epsilon}\right)^2 - \left(\frac{\partial h}{\partial \epsilon}\right)^2} d\epsilon \tag{8.3}$$

Since the flow velocity is low, it can be assumed that the strain effects are negligible and also, the focus here is on the curvature effects. Figure8.1 is a schematic representation of k1 and k2 in the flame contour. Essentially, k1 is along the contour and k2 is defined along the circumferential direction varying as the radius of the curvature changes with the flame height. Negative curvature is defined for a concave flame in the direction of the burnt gas and positive curvature is defined for a convex flame in the direction of the burnt gas.

Figure 8.2 a and b represent the inverse Abel transformed image with the pixel intensity represented in the colour bar axis for NH_2* and NH* respectively, Figure 8.2 c shows the thickness of the species (NH_2* in black and NH* in violet), and Figure 8.2 d displays k1 and k2 for NH_2*, all at $\varphi = 1.4$. k1 represents the principal curvature along the flame (shown in blue in Figure 8.2 d) and k2 represents the principal curvature in the circumferential direction (shown in red in Figure 8.2 d). The curvature for NH_2* is only presented here to be legible to the reader. The range and the trend of both k1 and k2 for NH* are similar to NH_2* (NH_2* is affected slightly higher than NH*). The x-axes of the plots represent the position normalized by the burner radius with the zero of the x-axes at the centre of the burner. The y-axis in Figure 8.2 a and b represents the position along the height normalized over the burner radius with the zero of the y-axis marking the exit of the burner. The thickness of the species was calculated as the full width at half maximum (FWHM) of the gaussian curve with a 95% confidence interval obtained when moving along the normal to front. The Abel inversion transformed images for all species at all equivalence ratio is provided in Annexe B. k1 and k2 for both NH* and NH_2* are also provided in the Annex B.

From the chemiluminescence of NH* and NH_2*, it is seen that the richer the flame, the less prominent is the curvature effect. For all conditions, except for $\varphi = 1.1$ and 1.2, it was noticed in the Abel inversion transformed images that the negative curvature at the tip of the flame does not enhance the reactivity as the average intensity remained almost constant all along the species front. Figure 8.3 a, b, and c show chemiluminescence of NH* for φ= 0.9, 1.1 and 1.3

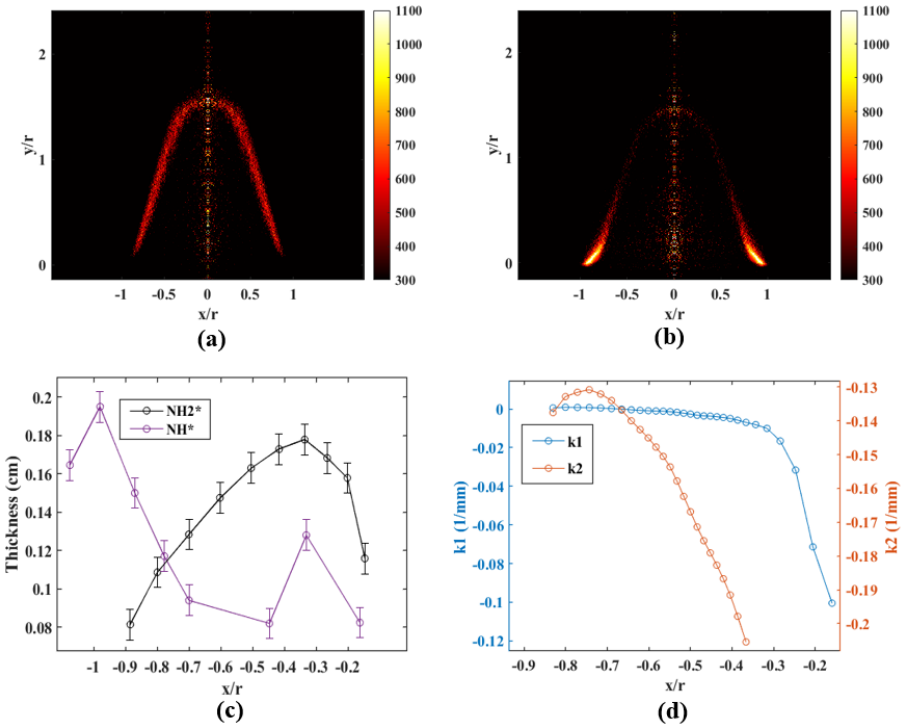

Figure 8.2: NH_2* and NH* signal in an atmospheric NH_3/air flame at $\varphi = 1.4$, (a) Abel inversion transformed image of NH_2*, (b) Abel inversion transformed image of NH* with the colour bar representing the pixel intensity, (c) The thickness of the species (NH_2* in black and NH* in violet) evaluated in the direction of the normal of the front vs. normalized position, (d) k1 (blue) and k2 (red) of NH_2* vs. normalized position.

respectively whereas Figure 8.3 d, e, and f show the chemiluminescence of NH_2* for φ= 1, 1.2, and 1.4. In these raw images, these effects are not visible simply because we see a 2D projection of the flame which means we see integrated information of the species. The chemiluminescence images of all species at all equivalence ratios can be seen in Annexe B. Since, the Lewis number increases with equivalence ratio and is close to unity [13], the effect of the negative curvature is not well pronounced at the tip of the flame, although a slightly higher effect is expected for richer flames which explains why φ= 1.1 and 1.2 witnesses a slight enhancement of reactivity at the flame tip. Irrespective of the excited species and the equivalence ratio of the mixture, it was observed that the species thickness continues to increase and begins to decrease when subjugated to the negative curve (indicated by k1) near the tip of the flame (in Figure 8.2 c and d, it is seen at x/r almost equal to -0.3). The magnitude of k2, on the other hand, increases when moving from the base of the flame to the tip of the flame. This goes to show that the mean curvature effect was simply seen as a change in thickness of the species produced if not directly the concentration of species in a given region as the average intensity remains the same (as seen in Figure 8.2). The concentration of the species was spread along

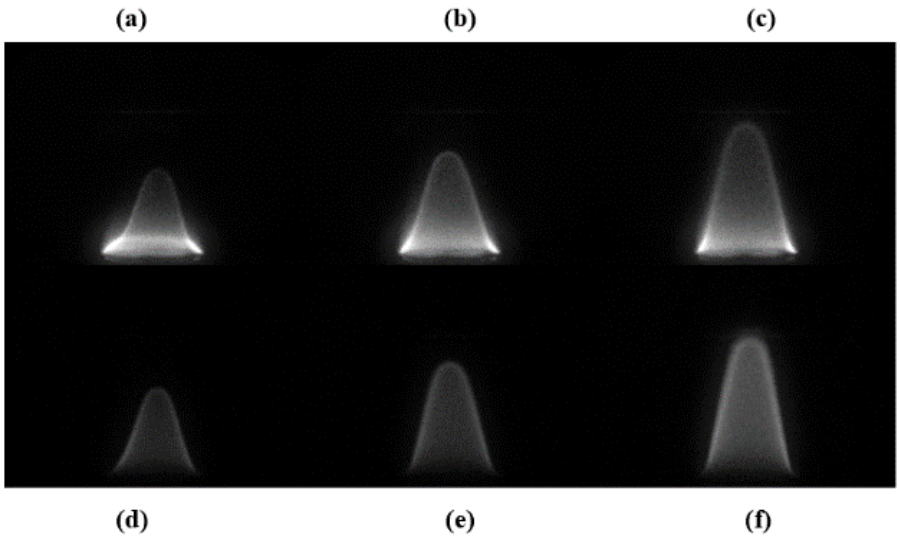

Figure 8.3: Chemiluminescence images of NH* at (a) φ=0.9, (b) φ=1.1, (c) φ=1.3, and NH_2* at (d) φ=1, (e) φ=1.2, (f) φ=1.4. The exposure time of these images is not the same.

a larger region where k1 was positive which was encountered near the tip of the burner for lean and near stoichiometric conditions and was concentrated over a smaller region where k1 was negative (seen at the tip of the flame). At the tip of the flame, the contribution of k2 is higher which gives an overall higher negative curvature effect. k1 is relatively smaller than k2 and is almost 0 until a distance of 0.3 times the burner radius. The stretch rate corresponding to the flame propagative/curved character, as presented in [122], Kc is proportional to the product of the mean curvature of k1 and k2 and the displacement speed. For ammonia-air flames, both the mean curvature and S_d are small.

On performing a species-wise comparison, it was seen that NH_2* undergoes a slightly higher mean curvature effect when compared to NH*. It was also seen that the NH_2* production was higher than that of NH* except for near the base of the flame as seen in Figure 8.2 b and Figure 8.3 a, b, and c and the thickness and the reactivity at this region being maximum (seen in Figure 8.2 c and b respectively). It was interesting to note that the NH* production was the highest at the tip of the burner and there was no production of NH_2* in this region. Since the positive curvature at the burner exit was prominent only for lean and near stoichiometric mixture conditions, the influence of the curvature leading to higher reactivity may be ruled out as the increase in production of NH* was seen unanimously for all equivalence ratios. It was initially thought that the heat from the pilot flame promoted the direct production of NH*. Nevertheless, it was confirmed that the pilot flame did not trigger thermal decomposition to give NH as if it were the case; the production of NH_2 would also be high. A simulation performed in Chemkin-Pro verified that it was not thermal decomposition. This is done under the assumption that the reaction pathway to NH is through the decomposition of NH_2. There may exist a reaction pathway to produce NH directly without the formation of NH_2 and

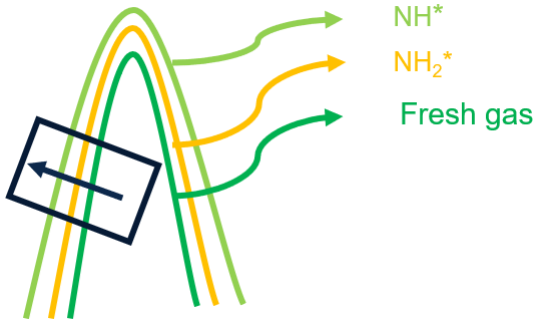

(a) The schematic diagram of superimposition of PIV and chemiluminescence results

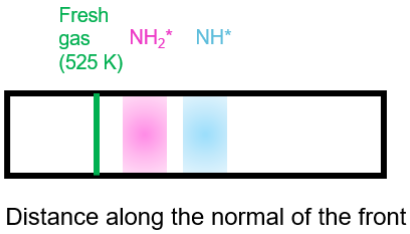

(b) The schematic representation of the experimental results in a 1D domain

Figure 8.4: Results obtained from the experiments

thereby, the corresponding excited species. It was ensured that there was no background light illumination effect. It is less likely possible that there is a presence of other species whose wavelength is within the bandpass width of the filter used as if this were to be the case, the presence of other species would be detected throughout the flame and not just at the base of the flame. The production of NH* may also be attributed to photodecomposition [133] or non-equilibrium process [134] where d'Agostino et al. employ a direct proportional relating the excited species to the non-excited species in NH_3 decomposition under radio frequency plasma at moderate pressures. Another possibility could be that since NH has weaker bonds than NH_2 and since NH is produced closer to the outer cone, it is in direct contact with the pilot flame whose temperature is about 2200 K which results in an increase of collisions resulting in a brighter zone. Further investigation needs to be done to understand this observation.

8.2 Flame structure

To study the flame structure, PIV, chemiluminescence and Chemkin simulations were used. Since, the Mie scattering images give the position of the fresh gas isotherm, i.e. the 525 K isotherm it was used as the reference. The species from the chemiluminescence image were superimposed upon the Mie scattering results which are shown as a schematic diagram in Figure 8.4a . Upon moving along the normal of the front, the species as a function of dis-

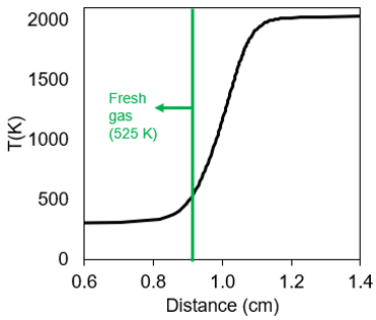

(a) Temperature vs distance at φ=1.1

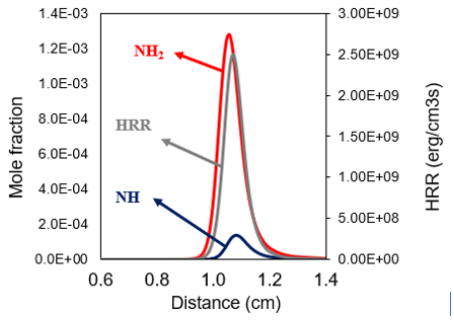

(b) Mole fractions and HRR as a function of distance at φ=1.1

Figure 8.5: Results obtained from the simulations

tance from the fresh gas isotherm can be represented in a 1D domain. Figure 8.4b is a representation of this 1D domain. Each of the species has been thickened to represent the FWHM. From the 1D simulation, the temperature profile as a function of distance and the concentration of the species can be obtained. Upon marking the 525 K line in the temperature profile, the fresh gas reference has been established. Figures 8.5a and 8.5b represent the results obtained from the Chemkin simulations. Figure 8.5b represents the mole fraction of the non-excited species and the HRR. Using this reference line, the experimental results can be superimposed over the numerical results. Figure8.6 a, b, and c represent the flame structure for φ = 0.9, 1.1, and 1.4 respectively. The fresh gas isotherm is represented as the green line. The temperature and the normalized HRR plot are shown in solid black and dashed black lines respectively. The distance along the x-axis represents the 1D domain. The species NH*, NH_2*, NH, and NH_2 are represented as cyan, magenta, blue, and, red respectively. The thickened plot for each of the species represents the standard deviation obtained for the excited species. From this fresh gas isotherm along the normal of the front, the relative position of the excited species can be obtained. To compare the stretched experimentally obtained flame with a Chemkin simulation of a non-stretched flame, a position along the experimentally obtained flame should be chosen such that, the stretch rates are negligible or quite small. For φ = 0.9, 1.1, and 1.4, at a height of about 6 mm (y/r slightly less than 1) from the base of the flame where k1 is almost zero and k2 is near -0.2 1/mm is considered as the curvature effect at this point is relatively less and may be compared to a 1D freely propagating unstretched flame. Chemkin simulations for the kinetic scheme of Stagni were performed to make this comparison. The temperature and the heat release rate (HRR) profile along with the concentration of the non-excited species can be when the excited species along the normal of the flame front and the non-excited species along the 1D domain are fitted into a Gaussian curve fit with a 95% confidence interval. It can be seen in the figures presented here that the species are overlapping with each other. For easy visualization, each of the species has been plotted as a quarter bar in order to minimize the overlapping between species which otherwise would have resulted in difficulty to understand the figure. The thickness of the flame front for each case is computed using the maximum gradient of temperature and is

found to be 2.2 mm, 1.7 mm, and 2.1 mm for $\varphi = 0.9$, 1.1, and 1.4 respectively.

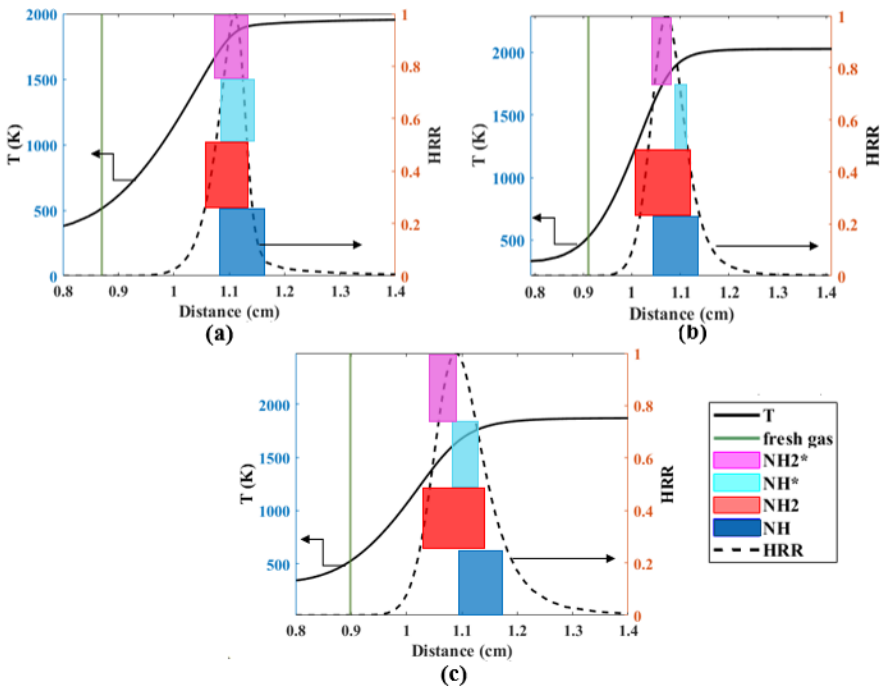

Figure 8.6: Flame structure at (a) φ=0.9, (b) φ=1.1, (c) φ=1.4. Temperature (solid black line) and the normalized HRR (dashed black line) are plotted on the left and the right y-axis respectively. The green line represents the fresh gas isotherm. The distance along the x-axis represents the 1D domain. Each of the species has been thickened to a width corresponding to the standard deviation of the gaussian-fit curve resulting in overlapping of the species. For easy visualization, each of the species has been plotted as a quarter bar in order to minimize the overlapping between species which otherwise would have resulted in difficulty to understand the figure.

From Figure 8.6, it can be seen that NH_2* is produced at a lower temperature than NH*. Also, both NH* and NH_2* are quite close to their corresponding non-excited species. The maximum HRR occurs between NH* and NH_2* for each of the cases. Therefore, the product of NH* and NH_2* is a good indicator of determining the maximum HRR experimentally. This is indeed, truly a cost-effective way of determining the HRR position.

CONCLUSION

In this part, an investigation was made to understand the inner structure of the flame. The important species were identified. The thickness of the flame In this part, an investigation was made to understand the inner structure of the flame. The important species were identified. The thickness of the flame and the position of these species within the flame have been depicted. Both experiments and simulations were used to correlate excited and non-excited species which were quite important to understand the production of these excited species. A preliminary study on the stretch effects on these species and therefore, its impact on reactivity for different equivalence ratios was performed.

The non-negligible thickness of atmospheric ammonia/air flames has been highlighted which implies that the thin flame approximation cannot be used. The dependence of the flame speed on the isotherm and the difference in the flame speed by choosing the fresh gas surface and the outer surface of the flame has been noted. To remain consistent with the theoretical definition of the flame speed, the isotherm to be chosen has to correspond to that of the fresh gases. The laminar flame speed for ammonia-air flame on a Bunsen burner at atmospheric conditions for equivalence ratios, φ = 1-1.4 by choosing the right surface has been evaluated. Evaluating the flame speed for the case of $\varphi = 0.9$ has not been presented here owing to its large error bars.

The curvature effects on both NH* and NH_2* for φ = 0.9-1.4 have been studied. It was seen that the curvature indirectly affects the production of species by modifying the thickness of the species. When k1>0, the thickness of the species is more than when compared to k1<0. The curvature effects are stronger for lean flames. Since the flow is of low velocity, the strain effects can be neglected. On comparing the species from the experiment at a height where the curvature effects are relatively lower, to a 1D freely propagating flame, the structure of the ammonia-air flame at atmospheric conditions for different equivalence ratios has been studied. It was found that both NH* and NH_2* were produced close to their counterpart non-excited species. The position of the maximum HRR can be determined experimentally from the position of these two excited species which is a useful indicator for obtaining information on flame stability in combustors.

Part III

Chemical and dynamical analyses of a premixed flame

INTRODUCTION

Part II focussed on the inner structure of a flame on a Bunsen burner using diagnostics like chemiluminescence. It was seen that there are no associated excited species accommodated in the chemical kinetics. It is interesting to add these species especially when these species can be used to obtain direct information on the position of HRR as seen in the previous part. The first step of Part III is to take it one step further by providing the concentration of certain excited species for the same configuration which is essential to add the excited species in the kinetic schemes. This step is especially useful when running simulations for different geometries and configurations.

It is known that turbulence enhances reactivity. But, turbulence is very complex in nature and capturing all phenomena is hard when they are coupled. So, the very rudimentary step is to understand a perturbed laminar flame. In this spirit, flame-acoustic interactions are studied. The objective of this section is to study the influence of curvature on the species. Upon surveying the literature, it was seen that there was no previous experimental work done on flame-acoustic interactions for ammonia flames.

Chapter 9 is a summary of the literature on the use of different excited species and the effect of perturbations in flame.

Chapter 10 is an overview of the experimental set-up used here for both determining the concentration of species and for flame-acoustic interactions.

Chapter 11 gives a detailed study of the procedure used to calibrate and find the concentration of the species. A quantitative and qualitative analysis of the emitted excited species is provided as well.

Chapter 12 sums up the different behaviours observed and attempts to give an insight into flame response to acoustic perturbations, especially with respect to curvature effects on the species.

This last part is concluded with interesting observations and results which give an answer to some of the unknowns, opening paths to new directions.

CHAPTER 9

CHAPTER 9

This chapter is dedicated to taking a quick peek into the literature to know the previous work that has been done on excited species from the chemiluminescence of ammonia flames and to understand the work done in perturbed laminar ammonia flames.

9.1 Quantitative and qualitative analysis of chemiluminescence of ammonia flames

Chemiluminescence in ammonia flames has been widely studied. A detailed review of chemiluminescence has been provided in Chapter 5. From these studies, NH_2* and OH* have been classified as species of importance as these species are indicators of certain parameters of interest. From [135], it can be seen that NH_2 is directly linked to NOx formations. For these reasons, it is interesting to study these excited species. However, in the literature, only a qualitative analysis has been provided [115, 118]. There has been no previous attempt to do quantitative analysis on these species.

Zhu et al. [115] in their work perform analysis on species like OH*, NH*, CN*, CH*, and CO_2*. The chemiluminescence intensity of these excited species is provided as a function of strain rate. The chemiluminescence intensity ratios are also provided as a function of the equivalence ratio. The objective of their work was to use their database to assess the feasibility of chemiluminescence-based sensors applied to ammonia-methane-air flames. Various ratios of chemiluminescence intensity were identified as potential surrogates for equivalence ratio and/or ammonia fuel fraction. From the results of Pugh et al. [118], it was concluded that NH_2* intensity is a good marker for NO consumption in rich NH_3 flames.

9.2 Perturbed laminar ammonia flames

There are several ways of studying the effect of stretch on flames. Some of the ways include studying swirl flows, flame-vortex interaction and even turbulent flames. Turbulent flames are quite complex in nature and so an easier way to assess the stretch effect is to study perturbed laminar flames. Studies on perturbed laminar flames including flame-acoustic interactions are quite common in hydrocarbon fuels. The idea here is to perform similar studies for ammonia flames to understand the curvature effects on the reactivity of these flames.

For ammonia flames, there exist several studies on swirl flows [42, 136] and turbulent flows [137, 138]. There is hardly any experimental work done on studying perturbed laminar ammonia flames. However, there are some numerical simulations performed. Netzer et al. [123] studied the curvature effects on NO formation and emphasized the diffusion effects of lighter species and its effect on local curvature. From the work done by Wei et al. [139], it can be concluded that the PDF of HRR indicated that the HRR was more likely to occur at slightly negatively curved flames. The present work is one of the first studies of its kind.

CHAPTER 10

CHAPTER 10

This chapter describes the two experimental setups that were used for the study: chemiluminescence for Bunsen flames and the acoustic perturbation setup used for the flame-acoustic interactions.

10.1 The chemiluminescence set-up

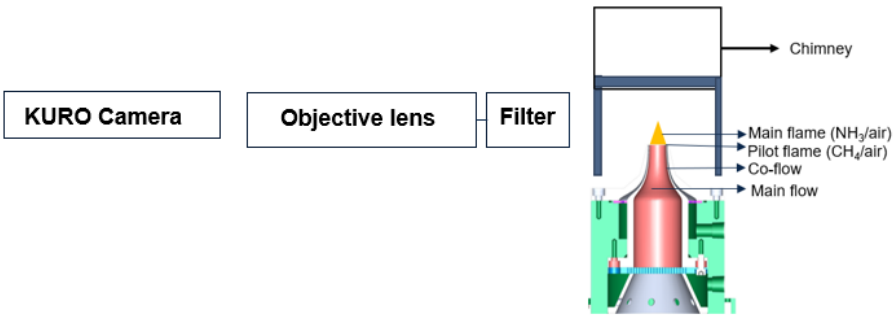

Figure 10.1: Schematic diagram of the chemiluminescence set-up.

From the previous chemiluminescence set-up, it was seen that the quality of the images obtained from using a high-speed camera was not good enough to extract the parameters of interest like curvature as the post-processing task was quite tedious due to the low signal-to-noise ratio. So, in this study, a sensitive camera offering a higher exposure time is used enabling better-quality images. This sensitive camera that was used is the Kuro back illuminated sCMOS camera and it employs a rolling shutter mode. Each line is read with a time lag of 10 microseconds with a delay of 5 microseconds. The camera is employed at a 12-bit mode with a 2048 x 2048 pix^2. Here, assessments are made locally and no information on the global geometry can be obtained as instantaneous data cannot be retrieved due to the rolling shutter mode. At a

time an evaluation is done for 50 pixels so that the total time to read 50 lines is less than the total exposure time. Figure 10.1 depicts the schematic diagram of the new chemiluminescence set-up. Since these images are captured using a more sensitive camera, an intensifier isn't required and the filters of species of interest can be mounted directly onto the camera. The software used to control this camera is LightField. The exposure time of the camera was set to 200 ms. An instantaneous shot is used for the study as it was seen that an average flame perturbation of over 200 images is small i.e. the induced error % in thickness is 13% for an exposure time of 200 ms. The conversion factor for NH_2* is 1.75 x 10^{-2} mm/pix and for OH* is 2.42 x 10^{-2} mm/pix

10.2 The flame-acoustic interaction set-up

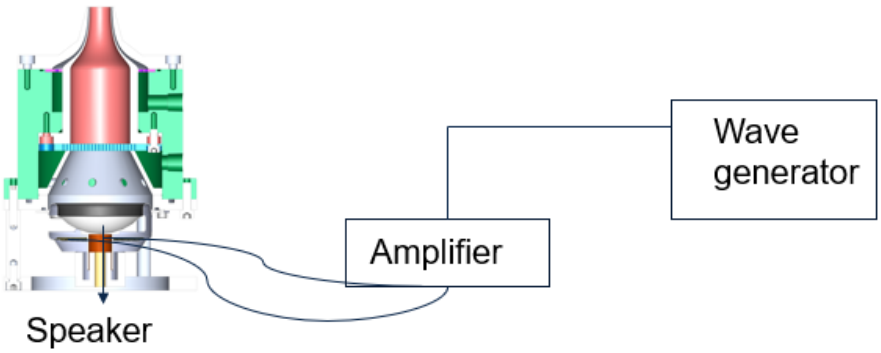

Figure 10.2: Schematic diagram of the chemiluminescence set-up.

To study the flame acoustic interactions, a speaker is placed below the burner as shown in Figure 10.2. The speaker that was used is NSW 3-193-8A of Aura. The range of frequency of the speaker is 50-100 Hz and its operating power is at 20 W. This speaker is connected to an amplifier which amplifies the signal coming from a wave generator. The amplitude and the frequency can both be controlled here. Also, the type of wave needed to be generated can also be monitored here. For this study, only sinusoidal waves that start from 0V to the desired amplitude are used.

The optical diagnostic used to study FAI is chemiluminescence. As demonstrated, from the previous part both NH* and NH_2* are good indicators of HRR and NH_2* has a higher signal than NH*. As a first step using, NH_2* alone as an indicator of the position of HRR is a good start. So the species of interest for this study is only NH_2*.

One of the ways to increase the signal-to-noise ratio is to increase the exposure time of the camera. However, when studying perturbed flames, there is a compromise between getting an image with a high signal-to-noise ratio and getting a non-blurred image caused due to accumulation of perturbed flames data over a large amount of time due to the high exposure time. In doing a brief study, it was seen that the maximum exposure time that can be set without having blurred images is 1 ms. The signal-to-noise ratio was not high enough to post-treat these data. So, tests were done on a non-perturbed flame

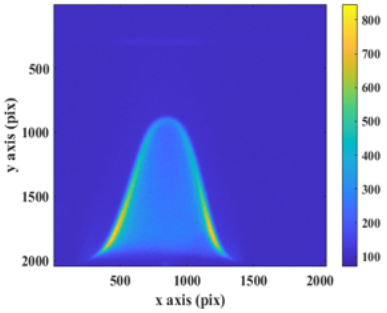

(a) NH_2* filter with the visible range objective lens.

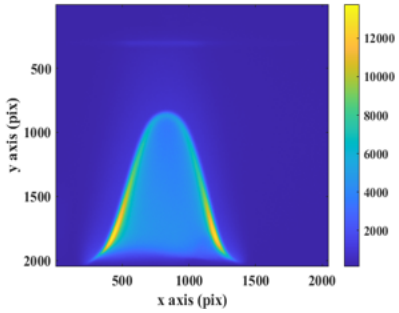

(b) Without the filter with the same conditions as before.

Figure 10.3: Raw images of the flame to note the differences between using a NH_2* filter and not.

with the NH_2* filter and without this filter, both images were captured using the visible range objective lens. As seen in figure 10.3a and figure 10.3b, the only difference in these two images is the intensities. Also, from the emission spectra, it is known that most of the peaks in the visible range belong to the NH_2* band. It is safe to say that the images captured without the NH_2* filter indicate collective information for NH_2* species at a different wavelength in the visible range and so once again, indeed HRR is still being monitored by tracking the front obtained upon using Inverse Abel transform. The conversion factor is 1.67 x 10^{-2} mm/pix.

CHAPTER 11

CHAPTER 11

The objective of this chapter is to give a meticulous description of the process involved in determining the concentration of the excited species from the chemiluminescence. The concentrations provided here do not account for the quenching effect and are for stretched flames. These concentrations that are provided are just related to the spontaneous emissions of the excited species and are proportional to the total population of the excited species. The range of the curvature undergone by these species was provided in the previous part. The idea of determining the concentration of these species is to accommodate these species in kinetic schemes that can be used in numerical simulation. Indeed the entire population of the excited species are related to collisions, chemical reactions that produce and consume these excited species and spontaneous emission of these excited species. Only the spontaneous emission of the species is measured here. The related Einstein emissions coefficients are unknown and so the concentrations that are provided are estimated concentrations. However, there are hardly any attempts to determine an estimated concentration for the excited species in ammonia flames. Including NH_2* is of special interest as it can be used to monitor quantities like the position of maximum HRR. In order to determine the concentration of these species, first calibration is required to understand how each element of the chemiluminescence set-up responds. For this step, a 95% homogeneous LED lamp of dimension 172 x 132 mm^2 is placed at the burner. The next step is to repeat the same process with a light source whose irradiation has already been determined. For this step, a quartz tungsten halogen lamp of power 45 W and current 6.5 A is used. The final step is to convert the pixel intensity as seen by the camera to concentration.

11.1 Step 1: Optics calibration

As mentioned before, to do a quantitative analysis, calibration is required to know the intensity of the images as a result of the camera response to the emission of the light source. The first step is to study the camera and the optic response of the system. Before studying this response, a region of interest

needs to be fixed. To fix the ROI, an image of the ammonia/air flame with the maximum possible height amongst the cases of interest (here at φ=1.4) was captured. This fixed ROI is given in Annexe C.

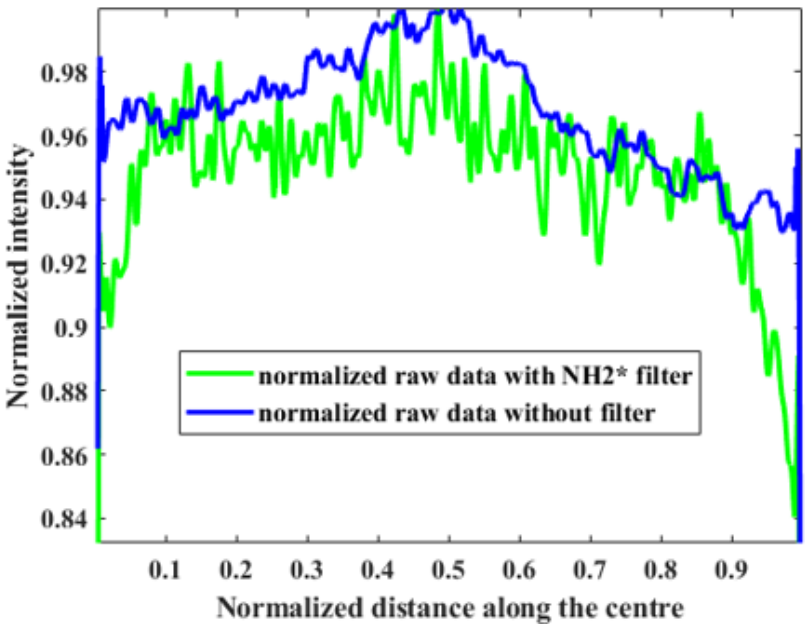

Figure 11.1: On comparing the normalized intensities along the centre of the images captured, it can be seen that by using the filter, the incoming intensity is reduced by less than 2%. The ROI is in between 0.1 and 0.8 on the x-axis and is marked in orange.

To study the camera response and the filter response, an LED lamp is placed at the burner's position. An image of the LED lamp is captured with and without the filter and is provided in Annexe C. On choosing a row passing through the centre of these images, both the intensities are normalized against its maximum value and are plotted as a function of distance. On comparing the intensity profiles, it is seen that the maximum intensity is observed at the centre of the filter. Near the periphery, the transmissivity is lesser than that of the centre. Since these curves resemble a gaussian-like curve, both curves are fitted with the appropriate gaussian curve. Upon the comparison of these intensities for both cases, it is seen that the difference in normalised intensities is only 2% and may be neglected. Figure 11.1 represent these curves. The blue and the green lines represent the raw intensity for the case without and with the filter on respectively whereas the red and the black lines represent the gaussian curve corresponding to the raw data.

To understand the camera response, first, the potentiometer of the lamp was set to a fixed value and the exposure time of the camera was increased. Next, the exposure time was set to a constant and the potentiometer of the lamp was varied. Both configurations were done with the filter mounted onto the camera and without the filter. Since the filter response was already monitored.

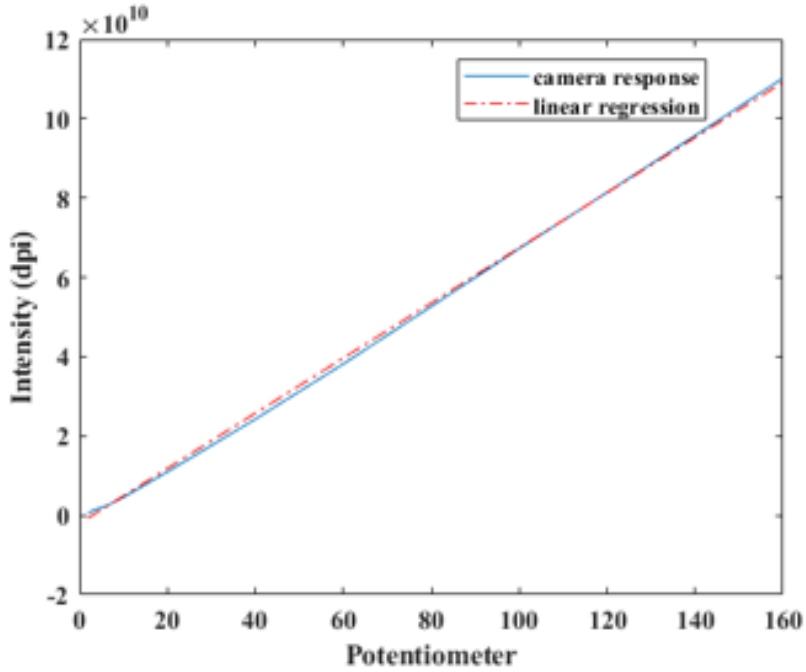

Figure 11.2: Intensity vs potentiometer of LED lamp at an exposure time of 1ms with the NH_2* filter mounted on the camera.

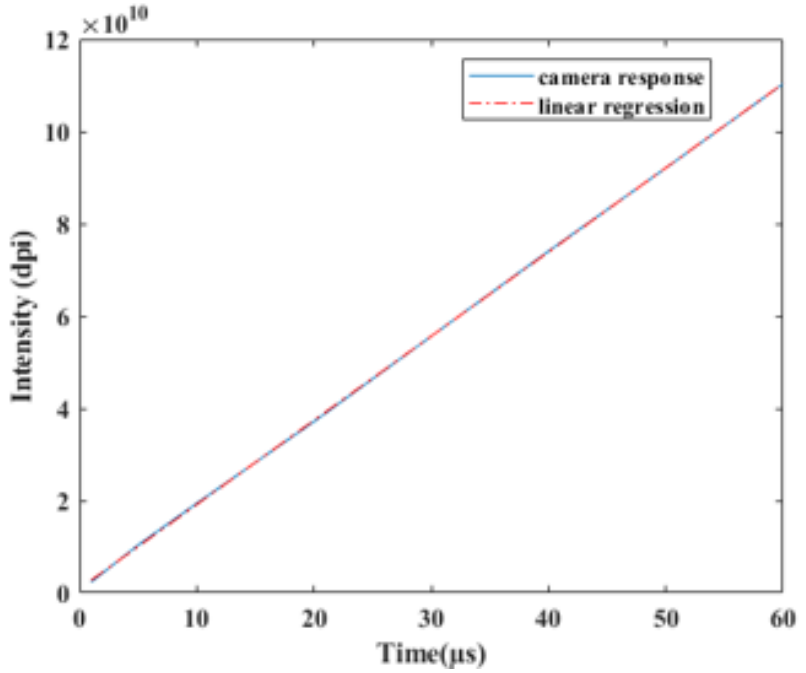

Figure 11.3: Intensity vs exposure time of camera with the potentiometer of the lamp set at k=6 with the NH_2* filter mounted on the camera.

The cases with the filter mounted on were studied. As shown in figure 11.2 and figure 11.3, linearity is seen for both cases, confirming a linear response of the camera to emission from a light source. In the figures, the red dotted line shows the linear regression and the blue lines depict the camera response in terms of the integrated intensity of the image.

The next step is to study the effect of background lighting. It is important to know the background information to get rid of the noise that might hinder the estimation process. All images are captured with the highest possible signal-to-noise ratio and so it is expected to have a very low noise signal. On subtracting the background image from the flame image, it was seen that the noise didn't cause any substantial change in information. The images supporting the case are provided in Annexe C.

11.2 Step 2: Tungsten lamp calibration

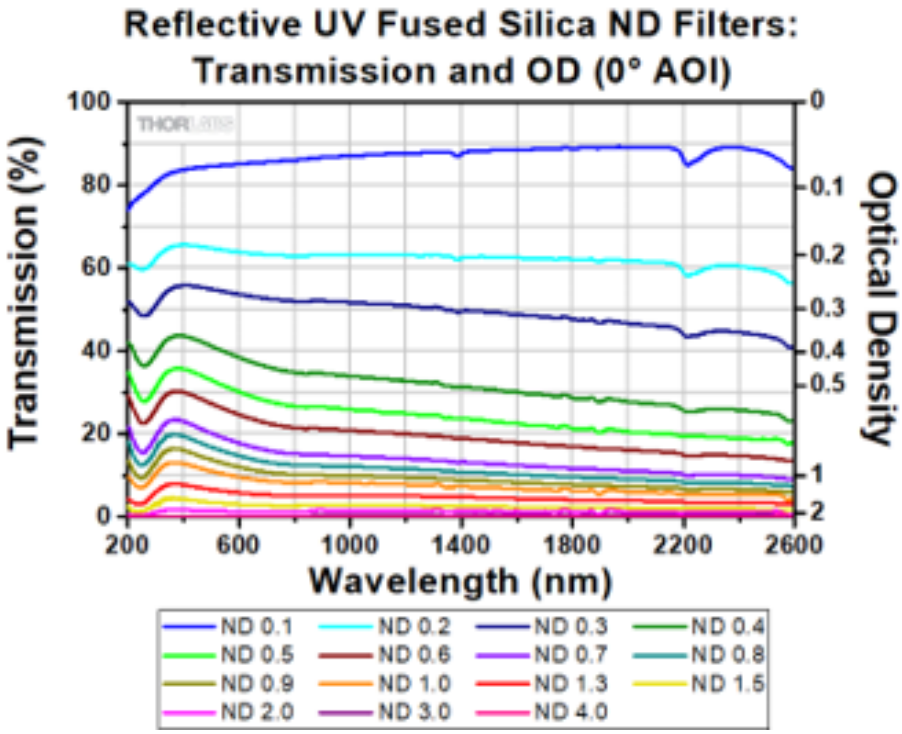

Figure 11.4: Transmission of the neutral desnity filters as a function of wavelength.

The previous step focussed on understanding and calibrating the optical part of the system. The next step is to calibrate the response of the tungsten lamp. On placing the tungsten lamp at the position of the burner, it was seen that the lamp was too bright and so 2 neutral density filters (ND 0.8 and 1) were needed to be used. The transmission of these neutral density filters as a function of wavelength is provided in the user's manual and is represented as

Figure 11.4. Since these neutral filters were added, the camera response needed to be tested again. Instead of using the LED lamp as the source, the tungsten lamp was used as the source. Figure 11.5 shows the camera response with the two neutral density filters. The response is still almost linear. The next step is to capture the image of the tungsten lamp with the filters of interest. The exposure time was set to 50 μs. The background image was subtracted and all non-filament pixels were set to 0. The region of interest was limited to the region of the tungsten lamp. Both the integrated intensities and the energies for the cases with different filters were calculated.

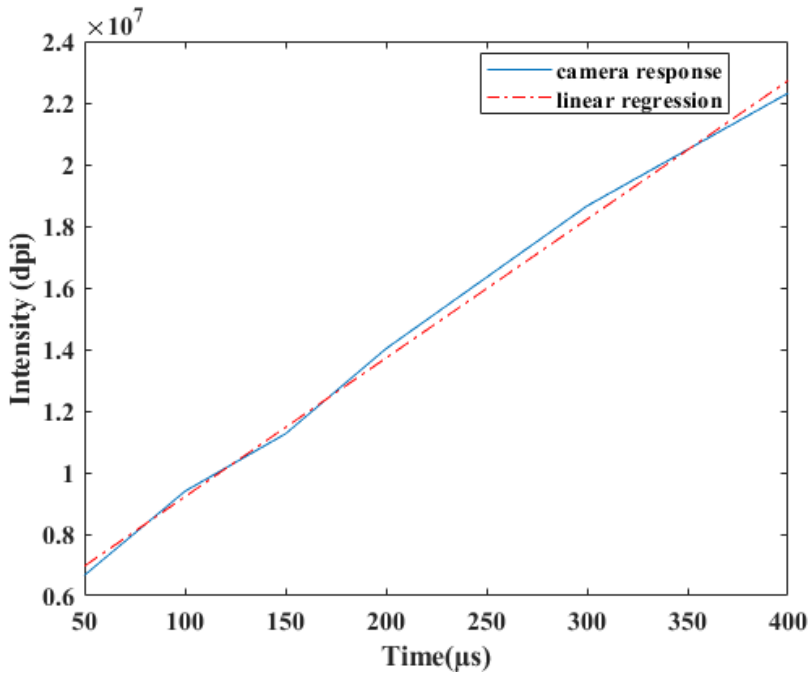

Figure 11.5: Intensity vs exposure time of camera with the ND filters and NH_2* filter.

11.3 Step 3: Correlation between concentration and intensity of the species

This step focuses on correlating the intensity as seen by the camera from an emission of the species to the concentration of the species. From [140] and [141], the ratio of the intensity of the inverse Abel-transformed image of the species to the intensity of the tungsten lamp image can be directly related to the ratio of the number of photons emitted for each case. The equation is given as:

$$\frac{I_{OH*,Abel}}{I_c} = \frac{N_{OH*}}{N_c} \tag{11.1}$$

where the subscript c denotes calibration lamp (here tungsten lamp), I denotes the intensity of pixel as recorded by the camera and N is the number of photons

emitted.

A second equation correlating the ratio of photons to the concentration of the species is also provided and given:

$$\frac{N_{OH*}}{N_c} = \frac{\frac{1}{4\pi}[OH^*]N_A\eta_3 08nm\tau\Delta t}{\int_{\lambda=305}^{315}\frac{S_c(\lambda)}{h\nu}\eta_\lambda d\lambda\tau\Delta t} \tag{11.2}$$

where N_A is Avogadro's number, η is the efficiency of the filter,τ is the efficiency of the optics, Δt is the exposure time, h is Planck's constant, ν is the frequency and S_c is the irradiation of the lamp within the wavelength of the OH* filter bandwidth.

On equating equations 11.1 and 11.2, the equation can be written as:

$$\frac{I_{species,Abel}}{I_c} = \frac{\frac{1}{4\pi}[species]N_A\eta_\lambda\tau_1\Delta t_1}{\int_{\lambda=a}^{b}\frac{S_c(\lambda)}{h\nu}\eta_\lambda d\lambda\tau_2\Delta t_2} \tag{11.3}$$

where 1 denotes the case of chemiluminescence and 2 denotes the case of the tungsten lamp. a and b denote the bandwidth wavelength of the filter used.

In equation 11.3, the efficiency of the filter used here does not change within its given bandwidth and so, it can be taken out of the integral and can be cancelled with the numerator. The exposure time used for both cases is not the same and the optics' efficiency isn't the same either as for the case of the tungsten lamp, neutral density filters are used. In equation 11.2, S_c is expressed in terms of W/m^2 μ m sr.

11.4 Step 4: Adapting the given irradiation values to the experiment set-up

The value of irradiation of the tungsten lamp as a function of wavelength starting from 300 nm in steps of 5 nm was provided as a document. These values were calculated at a position 50 cm away from the lamp. The unit of irradiation provided in this document is in terms of W/m^2 nm. The distance between the burner and the filter in the experimental setup is 32 cm. This means that the irradiation needs to be calculated at 32 cm. To compute the irradiation at this distance of interest, the value of irradiation at 50 cm is multiplied by the area of the sphere at 50 cm to get the value of the total irradiation and is then divided by the area of the sphere at 32 cm. Finally, to express irradiation in terms of W/m^2 μ m sr, this new irradiation term is divided by the solid angle. Solid angle is defined as the area of the filter divided by the square of the distance of interest i.e. 32 cm. On plugging in these values in equation 11.3, the concentration of the species can be determined.

11.5 Quantitative and qualitative analyses of species

The species of interest are OH*, NO* and NH_2*. NH* has not been used for this study owing to the low signal. The diameter of both OH* and NO* filters is 25 mm. The bandwidth of OH* is 10 nm. The filter used for NO* is a short pass cut off at 300 nm. All wavelengths below 300 nm can pass through the filter. Since the peak of other species below 300 nm is lower than that of

NO*, it can be assumed that most of the intensity corresponds to the emission of NO*. However, this filter is not very efficient as it can also pass light for a wavelength of more than 600 nm. As mentioned in the previous section, the value of the irradiation in the document provided is given from 300 nm, hence, it is not possible to determine the concentration of NO*. For these reasons, a qualitative analysis is done for NO* and a quantitative analysis is done for the other two species. Figures 11.6 and 11.7 represent the concentration of species of NH_2* and OH* with the values given in the colour bar in terms of mol/m^3 and Figure 11.8 represents the qualitative analysis of NO* with the colour bar that represents intensity. It is important to remember that these concentrations do not account for the quenching and are dependent on the stretch (even though the flame stretch is quite low).

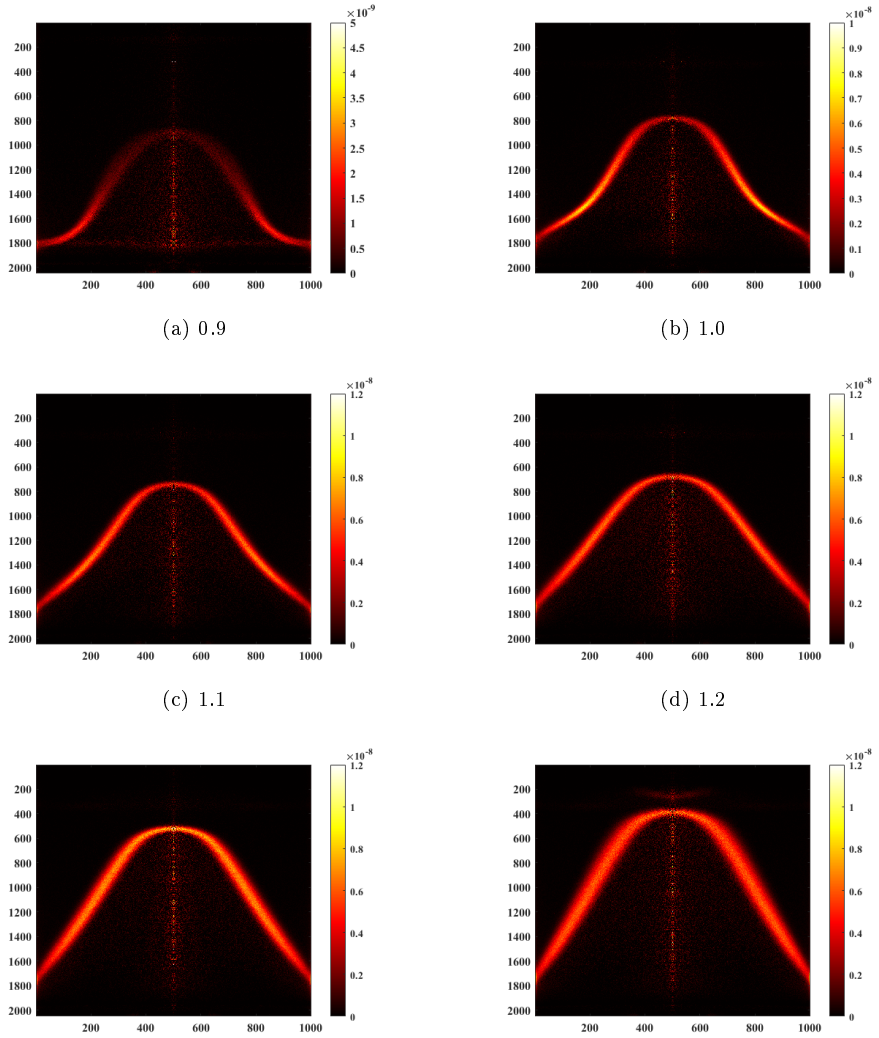

(a) 0.9

(b) 1.0

(c) 1.1

(d) 1.2

(e) 1.3

(f) 1.4

Figure 11.6: Concentration of NH_2* for $\varphi = 0.9$-1.4 with the colour bar representing the concentration in mol/m^3.

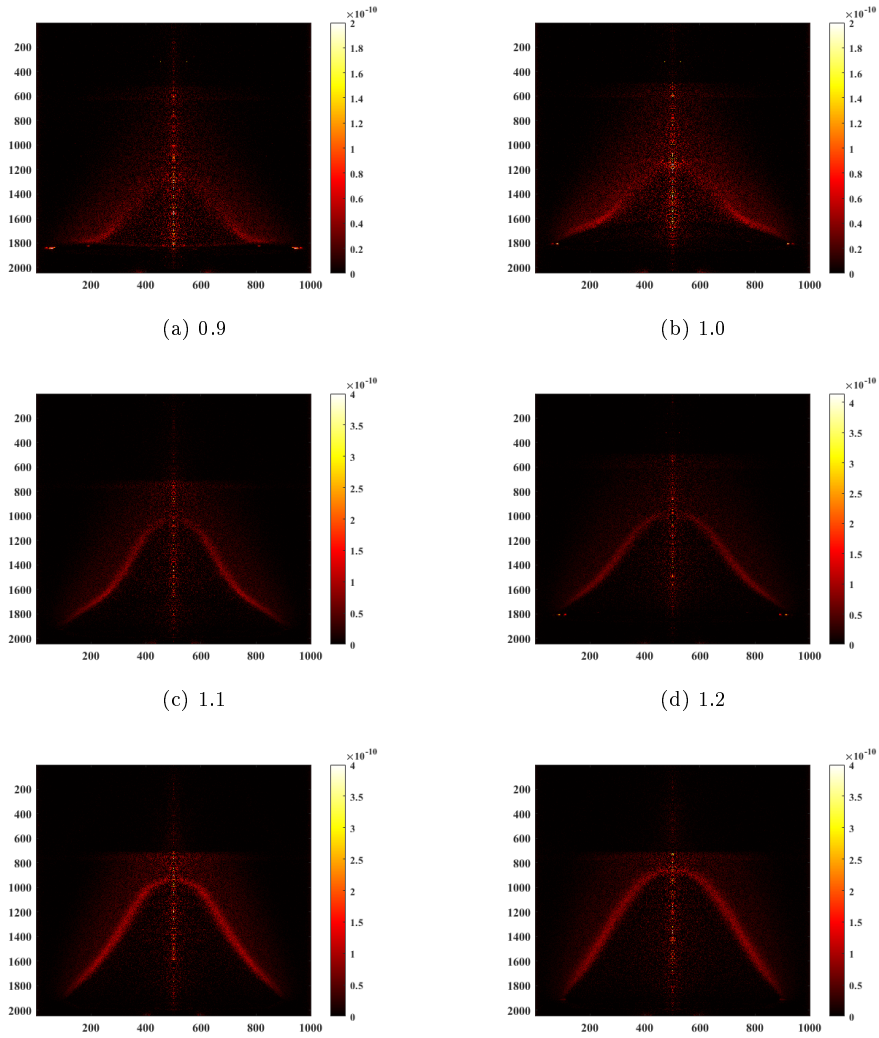

(a) 0.9

(b) 1.0

(c) 1.1

(d) 1.2

(e) 1.3

(f) 1.4

Figure 11.7: Concentration of OH* for $\varphi = 0.9$-1.4 with the colour bar representing the concentration in mol/m^3.

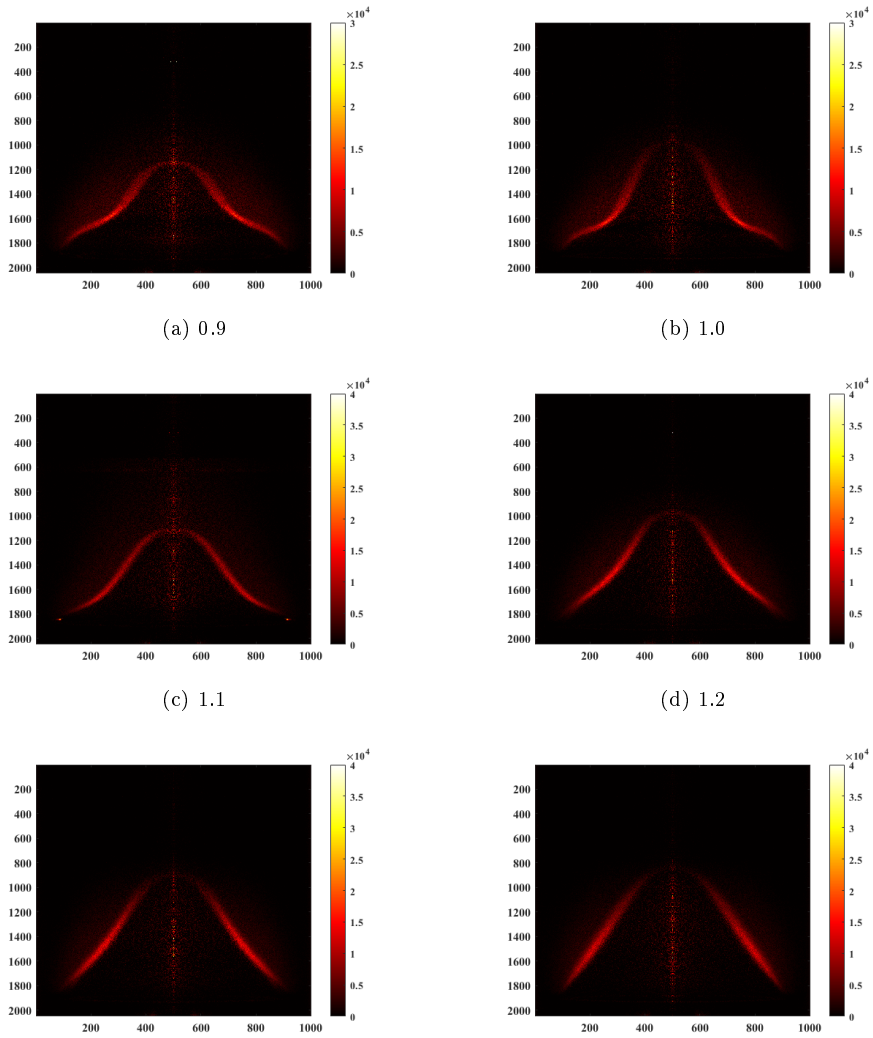

(a) 0.9

(b) 1.0

(c) 1.1

(d) 1.2

(e) 1.3

(f) 1.4

Figure 11.8: Qualitative analysis on NO* for $\varphi = 0.9$-1.4.

All of the above steps were verified by computing the concentration for OH* and CH* in methane-air flames and by comparing the value with the literature [142] and by running a Chemkin simulation using the GRI 3.0 Mech.

To compare the behaviour of each of the excited species for different equivalence ratios, a distance has been chosen (about 6 mm from the base of the flame) such that curvature effects are small and comparable for the different cases. The concentrations were plotted as a function of distance along the normal to the front from the fresh gases to the burnt gases. For NH_2*, each of these concentrations was fitted using a gaussian fit curve and the peaks have been realigned to facilitate the comparison and are presented as Figure **??**. On the other hand for OH*, the signal-to-noise ratio was quite low and so fitting these curves with gaussian curves would render wrong information and so raw

signals have been provided here in Figure 11.7. For OH*, unfortunately, a lot cannot be said but it can be" seen that the intensity for OH* is lower than that of NH_2*. The oh* fronts are thinner and do not increase as a function of equivalence ratios as is the case for NH_2*. On the other hand for NH_2*, it can be seen that the peak increases from 0.9 to 1.2 or 1.3 and then begins to decrease whereas the width increases as the equivalence ratio increases. On finding the position of the peak with respect to the 525 K isotherm reference line, it was seen that the peaks appeared closest to the reference line for the fastest flame ($\varphi = 1.1$) and it appeared the farthest for the slowest flame (φ =1.4).

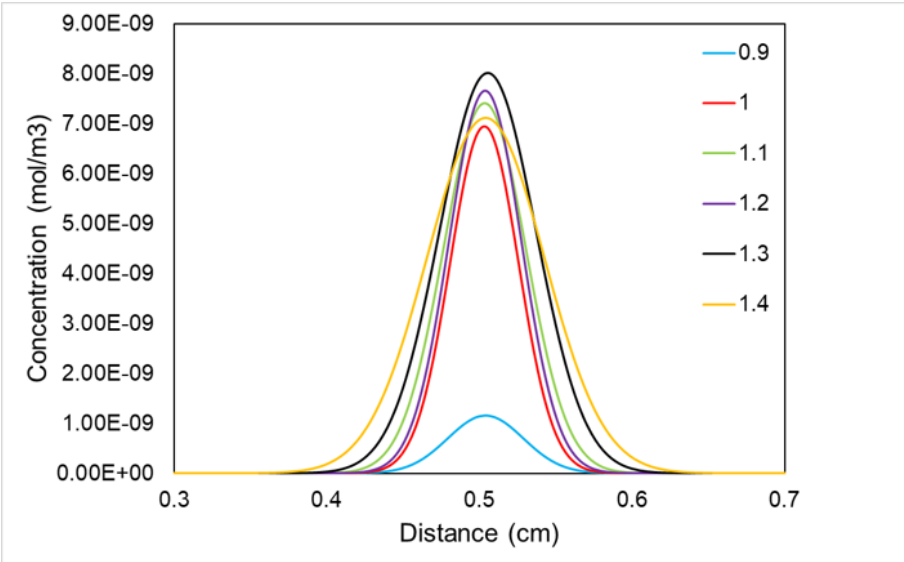

Figure 11.9: Comparison of NH_2* peaks for different equivalence ratios.

Finally, to facilitate the user, the important steps have been jotted down as points to follow and are given below:

(i) Fixing ROI in the domain.

(ii) Using the lamp as the source; recording an image with the desire filter on.

(iii) Recording an image at the same conditions without the filter on.

(iv) Comparison of these two images to know the error associated with the intensity.

(v) Camera response to the lamp used. (changing both the exposure time and the intensity emitted from the source)

(vi) Obtaining background image information (with and without the filter on).

(vii) Correcting the images (with and without the filter on) by subtracting the background noise.

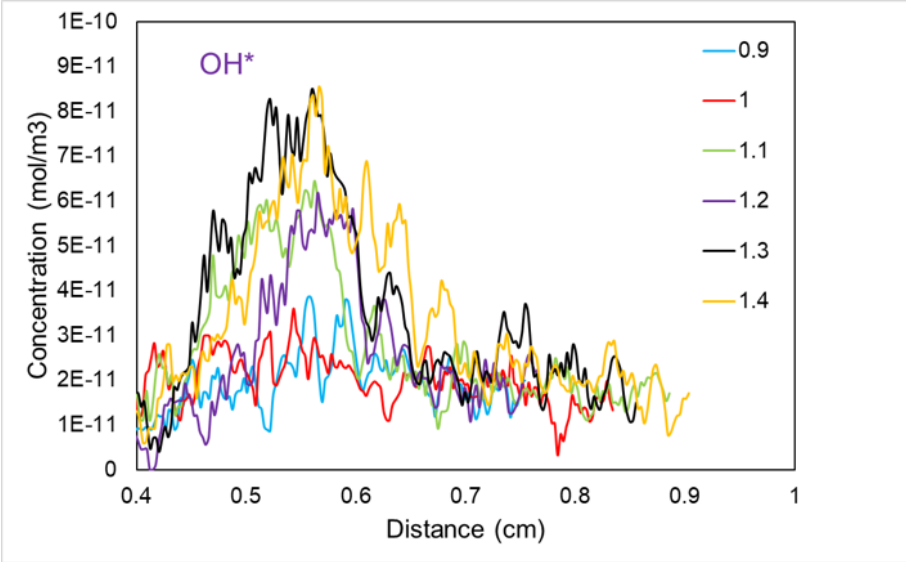

Figure 11.10: Comparison of OH* peaks for different equivalence ratios.

(viii) Recording the camera response for a tungsten lamp (calibration lamp).

(ix) Capturing an image of the tungsten lamp with the filters of interest mounted.

(x) Computing the intensity of these filament images.

(xi) Equation correlating concentration of the species to the intensity of the species.

(xii) Adjusting the given irradiation to the experimental set-up.

(xiii) Inputting the right quantities into the equation to determine the concentration of the species.

CHAPTER 12

CHAPTER 12

This chapter deals with studies on flame-acoustic interactions of premixed ammonia air flames. The focus of interest here is to understand the influence on reactivity from the curvature effect generated by acoustic perturbations.

12.1 Flame feedback due to acoustic perturbation

As mentioned in Chapter 9, the flame-acoustic interaction study is indeed a study of the flame feedback to the convective and the forced acoustic perturbation. In [14], Birbaud et al. used a critical Strouhal number, St_c to divide the flow into three regimes.

- For $St < St_c$, the flow is convective in nature,
- For $St = St_c$, the flow is of mixed type,
- For $St > St_c$, the flow is dominated by acoustics,

St_c is flame geometry dependent and is expressed as S_L/ U_o where S_L is the laminar flame speed and U_o is the convective flow velocity which can be measured from the PIV. Strouhal number, St is defined as:

$$St = \frac{fD}{U_o} \tag{12.1}$$

where f is the forcing frequency, D is the diameter of the burner exit, and U_o is the convective flow velocity.

Table 12.1 shows the Strouhal number with the respective subscript representing the forcing frequency with the critical Strouhal number for different equivalence ratios. Here, only St_{40} i.e. at 40 Hz is further explored as the Strouhal number at this frequency indicates that the acoustic perturbations are quite strong and dominate the flow very well which is the required kind of flow for this study.

Table 12.1: Strouhal numbers for different flow conditions

φ	$\mathbf{St_c}$	$\mathbf{St_{10}}$	$\mathbf{St_{20}}$	$\mathbf{St_{30}}$	$\mathbf{St_{40}}$
1.0	0.59	0.73	1.47	2.20	2.94
1.1	0.51	0.72	1.44	2.16	2.88
1.2	0.48	0.70	1.41	2.12	2.82
1.3	0.44	0.72	1.44	2.16	2.88
1.4	0.41	0.70	1.41	2.11	2.82

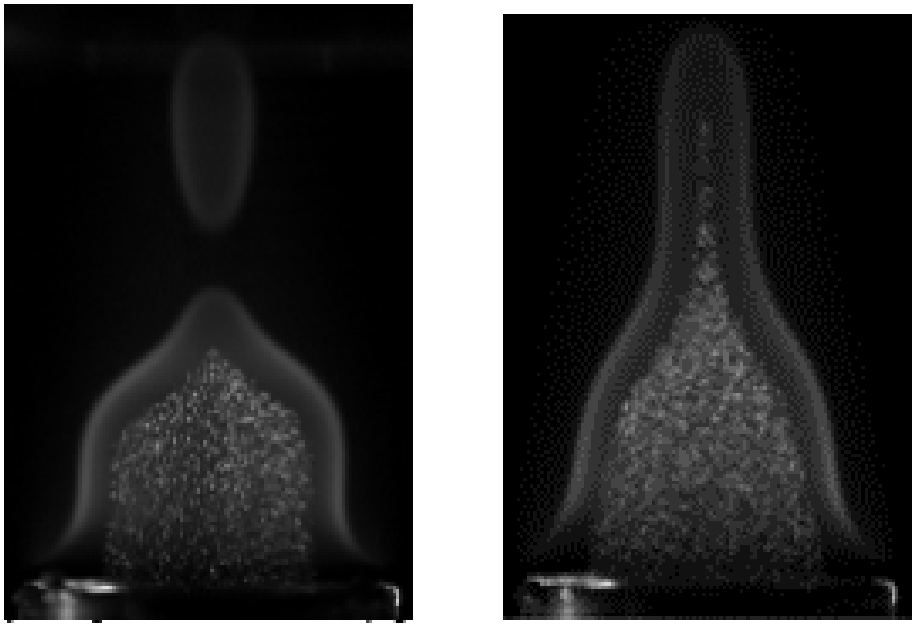

(a) Forcing amplitude = 0.375 V (b) Forcing amplitude = 0.25 V

Figure 12.1: The effect of amplitude on flames creating pockets of fresh gases for the same frequency (30 Hz) and equivalence ratio (1.1).

The acoustic perturbation itself is controlled by two parameters: A, the forcing amplitude and f, the forcing frequency. On changing the amplitude with keeping other parameters constant, it was seen that the more the amplitude more the flame elongation and compression, subsequently leading to pockets of fresh gas as shown in Figure 12.1a. Figure 12.1b was of lower amplitude and doesn't create a pocket of fresh gas. On increasing the frequency, different flame response modes were observed until a certain value, beyond which on increasing the frequency there is no change in the flame response. It was also seen that weaker flames are more easily perturbed i.e. the flame response was quicker for lower values of amplitude and frequency but on the other hand, the richer flames were not as responsive and began to show some changes only for a higher amplitude and frequency. Since, the objective of this study is solely on understanding the curvature effects on the reactivity, changing the frequency alone to obtain different excitation modes was of interest. From the Strouhal number and from understanding the effect of the equivalence ratio and the

two parameters of the forced perturbation, it was decided that only one of the case studies was to be further pursued: The forcing frequency was set to 40 Hz, the forcing amplitude was set to 0.5 V, the amplifier was set to 4 and, the equivalence ratio ranged between 1-1.4. As explained in Chapter 10, the species of interest is NH_2* and the exposure time of the camera was set to 1 ms.

12.2 Curvature effects on the reactivity

To study the curvature effect for the given test condition, it was ensured that a similar flame response mode was captured i.e. a similar flame shape was captured for different equivalence ratios. This was done to ensure that uniform parameters are maintained for all conditions. Initially, the mean curvature was obtained to quantify the curvature effect but it was seen that the flame response was too complex and so, the two principal curvatures k1 and k2 are used. Four different parameters: k1, k2, thickness along the normal to the front, and maximum intensity along the normal to the front were all plotted against the flame contours. The change in thickness of the front is an indirect effect of the change in reactivity. To understand the complete response of reactivity, the integrated intensity along the normal must be monitored. Once again, plotting curvature against integrated intensity was too complex and so this parameter was further divided into two basic parameters: thickness and maximum intensity.

After careful examination, it was seen that the effect of k1 and thickness along the contour seemed to be correlated but when it came to understanding the maximum intensity and k2, it was seen that their effect for all equivalence ratios was not very apparent. The case studies for k2 and maximum intensity have been provided in Annexe C. Each of the equivalence ratio cases has been detailed and is provided below.

Note: In each of the cases represented below, understanding the thickness vs the curvature graph is a tedious process. The reader is advised to start with the coloured point on the base of the flame, identify the corresponding point with the help of the direction of the curvature in the thickness vs k1 plot and move along the direction keeping in mind that each subsequent colour on the flame contour image is the colour to be looked out for in the thickness vs k1 graph. Numbers along the front have been added to facilitate the reader to understand the sense of direction.

12.2.1 Phi = 1.0

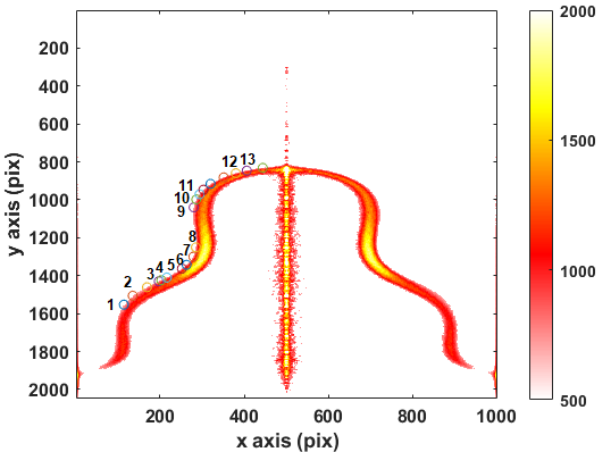

(a) Inverted Abel transformed with the points of interest depicted in coloured loops

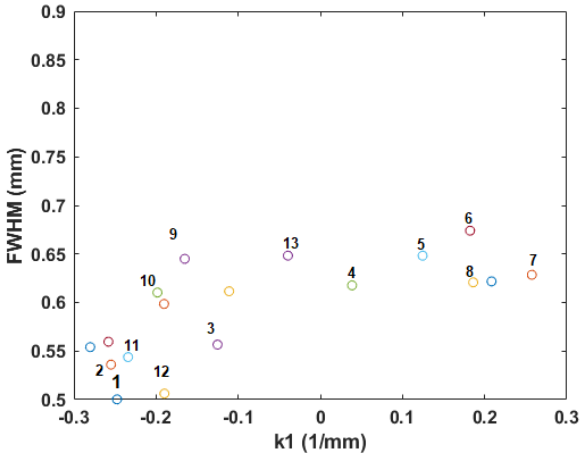

(b) Thickness vs k1

Figure 12.2: FAI for phi=1, A=0.5 V and f=40 Hz

In the case of φ=1.0, Le=1 [13] which means that both thermal and molecular diffusion plays an equally important role. It can be seen that the thickness does not vary a lot along the contour of the front. The effect of k1 on the thickness is not very evident in this case. Weak flames are more subjugated to curvature when compared to richer flames. It seems that the relatively higher magnitude of the curvature does not have a major impact on the thickness of these flames insinuating that rather than having an impact of curvature on the front, the thermo-diffusive effects play a larger role. Here, since both effects play an equally important role, the thickness seems to be uniform all along the contour.

12.2.2 Phi = 1.1

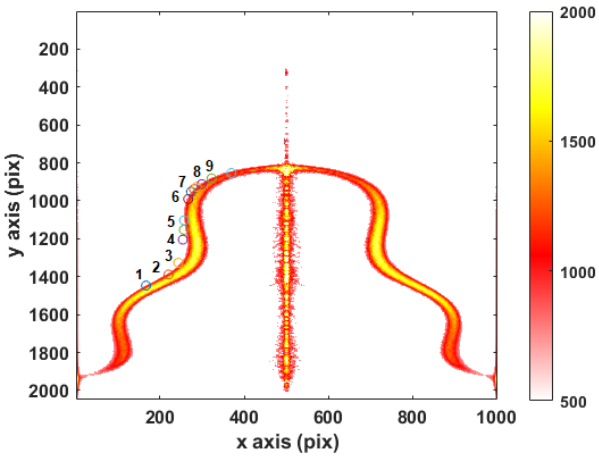

(a) Inverted Abel transformed with the points of interest depicted in coloured loops

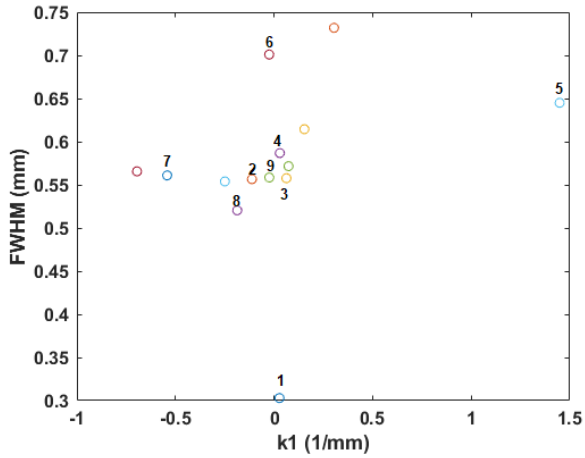

(b) Thickness vs k1

Figure 12.3: FAI for phi=1.1, A=0.5 V and f=40 Hz

At φ=1.1, Le=1.1 [13]. This implies that the thermal diffusion from the burnt gas towards the fresh gas happens at a slightly higher pace than the molecular diffusion of fresh gases into the burnt gases. In this case, a slight variation of thickness along the contour can be seen. The front gets thinner when a negative k1 is encountered and gets thicker when a positive k1 is encountered.

12.2.3 Phi = 1.2

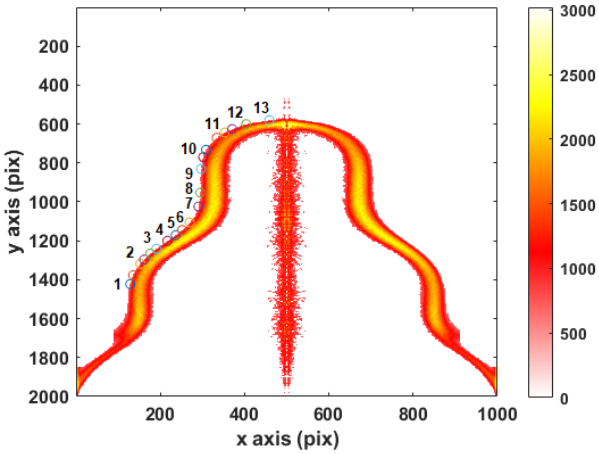

(a) Inverted Abel transformed with the points of interest depicted in coloured loops

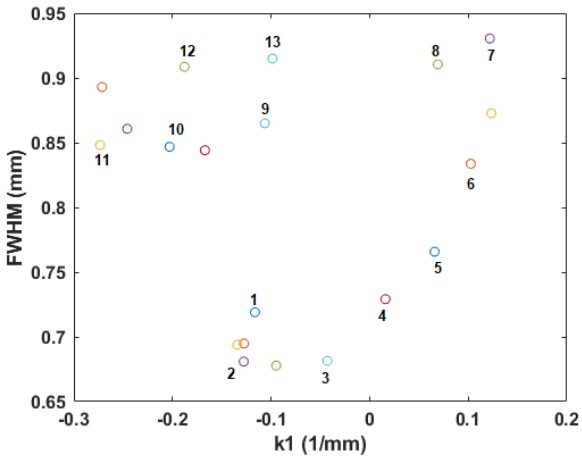

(b) Thickness vs k1

Figure 12.4: FAI for phi=1.2, A=0.5 V and f=40 Hz

In the case of, φ=1.2, Le increases slightly [13]. With an increase in equivalence ratio while almost maintaining the value of Le, shows a more prominent difference in the thickness vs curvature trend. The transition from a negative k1 to a positive k1 with thickness changing can be seen in Figure 12.4b. On comparing with φ=1.1, it can be confirmed that the Lewis number is not the only parameter that controls the flame response. From Figure 12.4b, it can be seen that for the same values of k1, the thickness value are not the same. These two points are located at two different positions along the contour. For the point further upstream, the value of thickness was higher implying that it is not just k1 that influences thickness but other parameters change from the base of the flame to the tip of the flame, thereby influencing the reactivity and

so resulting in affecting the thickness. This is further discussed at the end of the case studies.

12.2.4 Phi = 1.3

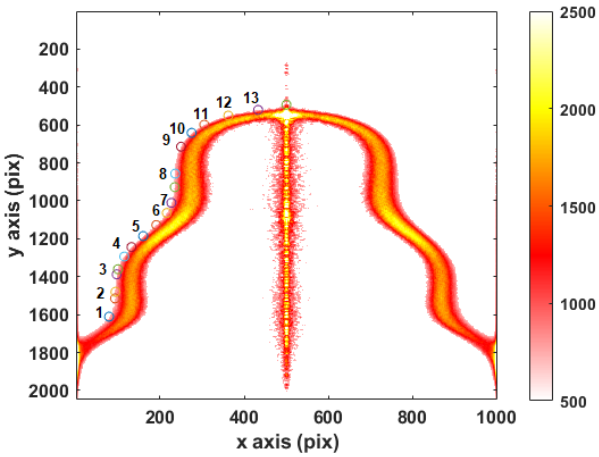

(a) Inverted Abel transformed with the points of interest depicted in coloured loops

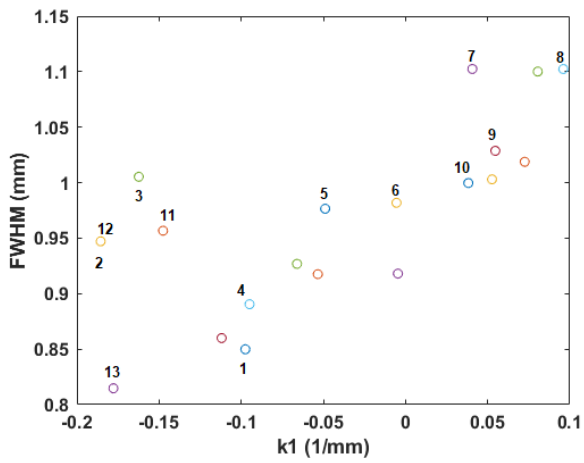

(b) Thickness vs k1

Figure 12.5: FAI for phi=1.3, A=0.5 V and f=40 Hz

For φ=1.3 with Le=1.09 [13], the trend of thickness vs k1 is quite similar to φ=1.2. However, the variation of thickness is much higher than that of φ=1.2 and the magnitude of k1 is lower than φ=1.2. As seen in the case of φ=1.2, the transition of thickness as the curvature changes can be seen in Figure 12.5b.

12.2.5 Phi = 1.4

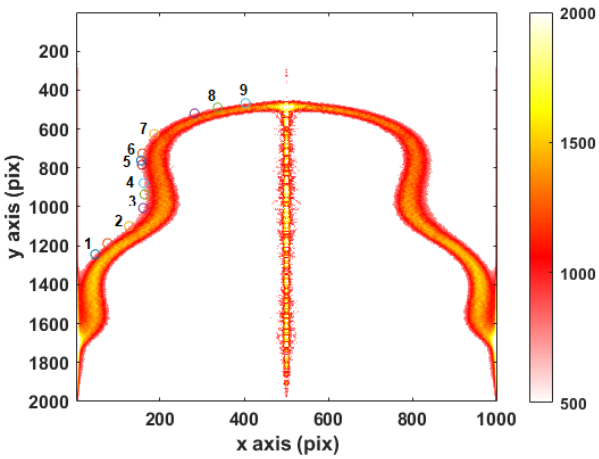

(a) Inverted Abel transformed with the points of interest depicted in coloured loops

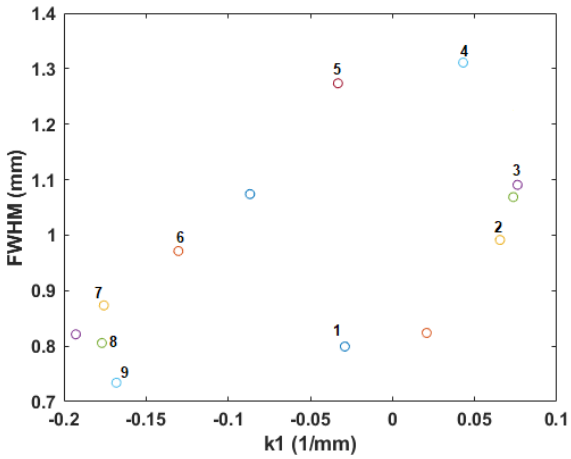

(b) Thickness vs k1

Figure 12.6: FAI for phi=1.4, A=0.5 V and f=40 Hz

For φ=1.4, the value of the Lewis number is slightly higher than 1. The range of the values of k1 for φ=1.4 and φ=1.3 is the same but the variation in thickness for φ=1.4 is higher than φ=1.3 implying that change of thickness as a function of k1 is more prominent for the very rich flames. As the flames get thicker, it is important to note that the curvature calculated at the outer contour (as done here) may not be the same as the values that will be obtained on computing in the inner contour. For consistency, only the outer contours have been used for all the cases.

From all of these cases, it is quite apparent that irrespective of the condition, a negative k1 results in the reduction of thickness and a positive k1 manifests as an increased thickness. In Annexe C, both k1 vs contour of the flame and

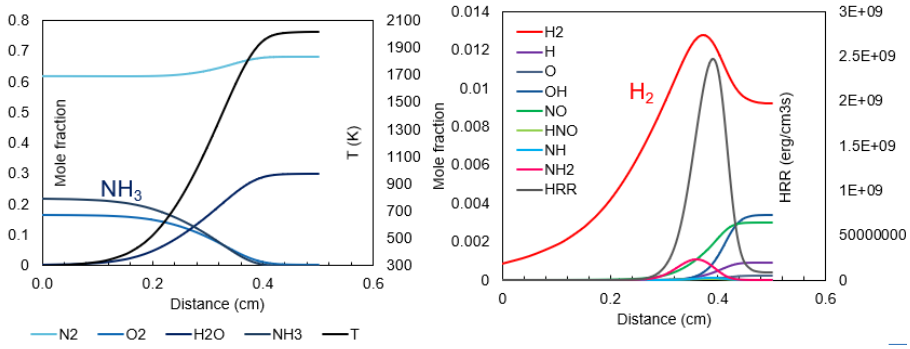

Figure 12.7: Simulation using Stagni et al. to indicate the decompisition of ammonia to produce H_2 confirming the possibility of preferential diffusion

thickness vs contour of the flame for each of the cases have been provided. As noted for some of the cases, it also seems that the intensity is higher for the positive k1 implying that the reactivity is enhanced. To test this, images were captured using a high-speed CMOS camera (PHANTOM V1611). Figure 12.7 shows the different flame responses for the case of φ =1.1. Upon inspecting every case, it was concluded that indeed the intensity remains more or less the same along the sides of the flame irrespective of the direction of curvature. Figure 12.7 represents this. On examining each pixel along the front, it can be seen that there is a slight increase in intensity for positive curvatures when compared to the negative curvature but this increase is so small that it is negligible. However, the thickening effect is influenced by the direction of the curvature. This was further verified by capturing a different flame shape by using the KURO camera. For all cases, it was seen that the intensity decreases when moving away from the flame base. This phenomenon was captured in the case of $\varphi = 1.2$ where on plotting k1 vs thickness (Figure 12.4b) the thickness was different for the same k1 at two different positions along the contour. As mentioned before thickness is also an indicator of reactivity. The reason for the enhanced intensity on the sides closer to the base of the flame and decreased intensity as one moves away from the flame base is attributed to the diffusion-convective velocities. The convective velocity is about 25 times more than the diffusion velocity of ammonia into the air at the exit of the burner. The diffusion velocity of ammonia into the air was calculated using Fick's law. It is understood that ammonia decomposes into lighter species whose diffusion velocity is much higher than the convective velocity. The preferential diffusion of H_2 and other species towards the sides play a major role in enhancing the local reactivity. For this reason, the intensity or reactivity is higher towards the sides of the flame closer to the base compared to the tip of the flame. The effect of preferential diffusion on the reactivity of curved flames has been highlighted by Mizomoto et al. [143]. A Chemkin simulation was performed using the mechanisms of Stagni et al. and it was seen that indeed there is a decomposition of ammonia into H_2 and is shown in Figure **??**. On running a reaction pathway analysis and on looking into the rate of production chart, it was seen that the dominant reaction through which ammonia decomposition takes place is $NH_3 + H \rightleftharpoons NH_2 + H_2$.

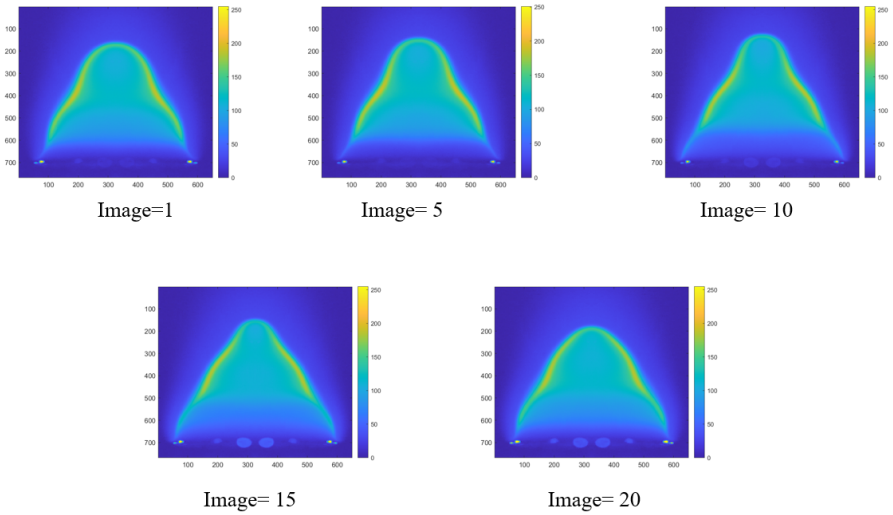

Figure 12.8: Flame response at different instants at φ =1.1, A=0.5 V, f=40 Hz.

The Damköhler number, Da is defined as the ratio of the flow time scales to the chemical time scales. The chemical times scale can be obtained by dividing the thickness of the flame by the laminar flame speed. The Damköhler number for these case studies was slightly more than 1, implying that the time of the forced perturbation on the flow was slightly more than the chemistry time scale and so, the perturbation was a little slow to interact with the flame front. However, it is important to emphasize that the time scales in both cases are still comparable and the effect of the perturbation on the flow is seen as a local change of thickness with respect to the orientation of k1 along with the Lewis number of the flame determining a major role in the flame response. It may also be concluded that for the studied cases, the preferential diffusion effects play a large role in any changes of reactivity and as far as curvature effects are concerned, the effect of k1 can be seen as a change of thickness. Studies [123] show that for a hydrogen-enriched ammonia flame, there is a change in the rate of preferential diffusion as a function of the orientation of the curvature. These effects were not observed for the given case study here.

CONCLUSION

This part is dedicated to study the behaviour of different excited species that are quite vital to understand certain behaviours of ammonia flames. The first objective of this section was to determine the concentration of some of these emitted excited species. No previous attempt was seen to determine the concentrations of these emitted excited species for at least ammonia-air flames. From the previous part, it was seen that NH_2* is a good indicator of the position of the maximum HRR. Since the excited species have not been accommodated in kinetic schemes due to lack of sufficient data, the concentration of the species like OH* and NH_2* have been provided here as a first step to achieve this task. These concentrations do not account for the quenching effect and are dependent on the stretch. It was seen from the previous section that the curvature rates are quite low. Qualitative analysis on NO* has also been provided. A detailed procedure highlighting the important steps to find the concentration has been given.

For the flame-acoustic interactions, NH_2* was monitored as this species would give direct information on the heat release rate. However, NH_2* filter was not used due to the amount of signal received by the camera. Instead, a visible range lens without any filter was used to obtain collective information of NH_2* bands in the VR spectrum. From a preliminary analysis, perturbation conditions were chosen such that $St > St_c$, so that the flow is dominated by the acoustic perturbations. The impact of the amplitude and the frequency on the flame response was studied. On pursuing a case study for different equivalence ratios, it was seen that the principle curvature k1 had a direct effect which was manifested as a change in the thickness of the species front. On studying the trends displayed by k2 and the maximum intensity, nothing conclusive was deducible. As far as reactivity enhancement is concerned, it was seen that for the given case, the convective-diffusion velocities played a major role. It was understood that ammonia decomposes into lighter species which diffuse faster towards the sides of the flames, enhancing the reactivity and decreasing this enhancement towards the flame tip. This was confirmed by performing a simulation in Chemkin-Pro. It was seen that ammonia decomposed into hydrogen. Since the Da was slightly more than 1, the time scale of the perturbation was slightly longer than the chemistry time scale. It is important to emphasize

that the time scales in both cases are still comparable and the effect of the perturbation on the flow is seen as a local change of thickness with respect to the orientation of k1 along with the Lewis number of the flame determining a major role in the flame response. In the given case study, it can be said that the preferential diffusion effects play a dominant role in changes in local reactivity although, no change in the rate of preferential diffusion was observed as a function of curvature. The effect of k1 is simply seen as a change in the thickness of the species front.

GENERAL CONCLUSION

Ammonia combustion has indeed sparked interest all around the world as a replacement for conventional fuels. It has intrigued the scientific community in the last few years as there are a lot of phenomena pertaining to ammonia combustion that has not been fully understood. The motive of this thesis is to pick a few of these unknowns and make an attempt to understand the behaviour of these flames. The primary focus of this study is on the chemical properties of premixed, pure ammonia laminar flames. The flame speeds for different initial conditions, the inner structure of the flame, the behaviour of perturbed laminar flames, and the response of the flame to change in parameters for each of the cases have been thoroughly investigated. The major part of this work is experimental in nature and has been complemented with 1D numerical studies using Chemkin-Pro. Two different experimental set-ups: the constant volume combustion chamber and a Bunsen burner were used. One of the main goals was to provide experimental data that can be used to improve the existing kinetic schemes in ammonia combustion which is used in running numerical simulations. This thesis has been divided into three parts to carefully evaluate and achieve the set objectives. Each part has afforded new insights into ammonia combustion.

The first part is dedicated to rendering flame speeds at high pressure and temperature conditions. The conditions that were targeted were much higher than the range found in the literature then. These conditions are tested with the idea of mimicking high-pressure and temperature conditions like those that are found in engines and gas combustors. In this study, the flame speeds have been reported for up to 30 bar and 585 K. The experiments were performed using premixed oxygen-ammonia mixtures with diluents for three different equivalent ratios: 0.8, 1.1, and 1.3 with different initial pressures. This work was one of the first of its kind to determine the pressure-independency of flame speeds and that flame speeds are temperature driven. A range of values of the exponential factors α and β was provided showing that the pressure exponential factor - β was much lower than most of the known fuels. Flames that lack pressure dependency are desirable in gas combustors as these flames are not easily destabilized by the constant change of conditions in the combustion chamber. A test on the dependency of bath gases was also done along with the evaluation of

the performance of some of the recent kinetic schemes in ammonia combustion. These experiments were performed in a relatively new set-up: OPTIPRIME at ICARE, CNRS, Orléans. It is a constant-volume combustion chamber which has a 360-degree view. This set-up indeed has some marvellous engineering done to obtain the smooth spherical fused silica ring. A high-speed camera was used to record these images.

The second part explored the structure of the flame. The diagnostics included PIV and chemiluminescence. A high-speed camera with an IRO intensifier was used to record these images. These tests were performed using premixed ammonia-air mixtures for an equivalence ratio ranging between 0.9-1.4 at atmospheric conditions. The highlights of this part include determining the excited species that can give direct information on the position of the maximum HRR and the non-applicability of thin flame approximations for ammonia-air flames. NH* and NH_2* have been found as indicators of the maximum position of HRR for ammonia-air flames. An assessment of flame speed calculation has also been provided. The structure of the flame for different equivalence ratios has also been described. Finally, the response of species to different equivalence ratios and curvature was noted. These experiments were performed under atmospheric conditions.

The last part involves an attempt to provide the concentration of some of these excited species. A quantitative analysis of species emitted from ammonia flames has not been given in the literature and for the same reason, these species have not been accommodated in kinetic schemes. The addition of the species to the kinetic schemes has not been done here but it is a work in progress and the core of a future publication. No previous attempts to study flame-acoustic interactions for ammonia flames have been recorded in the literature. The objective of the flame-acoustic interaction studies is to understand the curvature effect on reactivity. Monitoring mean curvature and integrated intensity along the normal (parameter to quantify reactivity) was a complicated task. And so, the mean curvature was split into two principal curvatures and integrated intensity was split into the thickness and maximum intensity along the normal to the front. For the given case study, it was concluded that even though the flow was dominated by the acoustic perturbation, the time scale to study the curvature effect on the reactivity due to the perturbation was slightly longer than the chemistry time scale. The preferential diffusion of the lighter species playing a more dominant role has been noted. The acoustic perturbation on the flow along with the Lewis number resulted in different flame response and the changes in reactivity was simply seen as a change in the thickness of the species front. This change of thickness due to curvature was attributed to the principle curvature, k1 along the contour of the front. The impact of the curvature effect on the local displacement and the consumption speed has not been done here but it is of significant interest and can give some deeper insights.

The second and the third parts were performed with the same test conditions on the same test bench which was set up specifically to cater to the use of ammonia. Pipes, mass flowmeters, and other connections that were compatible with ammonia were used to minimise ammonia-related corrosion and other hazards. A Bunsen burner with a pilot flame was used to perform these experiments at ambient conditions. The pilot flame of the methane-air mixture at stoichiometry was required to stabilise the weak ammonia flame. A sensitive camera was used to record these images.

There is still a vast amount of work that needs to be done to fill the gaps in ammonia combustion. Numerical simulations using LES or DNS can be performed at the same experimental conditions to complement the experimental data. The use of these experimental data to improve or update the existing kinetic schemes is interesting as the experiments performed here are at unique conditions when compared to the existing literature data. As mentioned before, the concentrations of the excited species can be used to accommodate these species in the kinetic schemes as these species can give direct information on some parameters of interest. For studies on flame-acoustic interactions, finding the local displacement speeds and the consumption speeds and the impact of curvature on it is quite important. Also, targetting flows with $Da \ll 1$, may be interesting to have sufficient time for the perturbation to interact with the reaction zone. These conditions may give deeper insights into the curvature effects on the reactivity. For the given experimental test bench, these conditions are not easy to achieve owing to the low flow velocities which result in a limitation in exploring different perturbation frequencies as one might reach a certain frequency beyond which increasing the forcing frequency does not change the flame response. This value of frequency is dependent on the initial flow conditions.

Overall, the performance of ammonia combustion can be drastically improved to fit within the criterion of a feasible fuel. The flame speeds can be significantly increased by the addition of excess oxygen as done in the first part here or by blending with other fuels. A significant amount of the research work available is on blended fuels and this is done with the idea of taking advantage of the desirable properties of two or more fuels. Studies show that the reactivity enhancement due to blended fuels especially hydrogen can be beneficial. Transporting and storing ammonia is easier when compared to other zero-carbon fuels of interest like hydrogen. Also, ammonia can be produced on large scales using the Haber-Bosch process. Research shows that cracking ammonia to blend ammonia and hydrogen may be one of the most sustainable ways to solve the problems that come with hydrogen and at the same time make use of the blended properties. The toxic nature of ammonia may be one of the reasons why ammonia is not user-friendly however, as mentioned in the introduction of this thesis, SCRs have been developed to convert ammonia directly into nitrogen in case of leaks. With a little more research and technology to overcome some of the other limitations, ammonia can be deployed as one of the top sources of energy of tomorrow. Indeed, ammonia shows the potential to solve the global energy crisis.

COMMUNICATIONS ASSOCIATED TO THIS WORK

Journal articles

A. Karan, G. Dayma, C. Chauveau, F. Halter, Experimental study and numerical validation of oxy-ammonia combustion at elevated temperatures and pressures, Combust. Flame 236 (2022) 111819.

A. Karan, G. Dayma, C. Chauveau, F. Halter, Insight into the inner structure of stretched premixed ammonia-air flames, Proc. Combust. Inst. 2022 (in press).

A. Karan, G. Dayma, C. Chauveau, F. Halter, Preliminary study on flame-acoustic interactions for premixed ammonia-air mixtures, JAE. 2023 (submitted).

Presentations in conferences/gatherings

A. Karan, G. Dayma, C. Chauveau, F. Halter, Laminar flame speeds of ammonia mixtures at high pressure and temperature conditions: New experimental results and performance of different kinetic models, 17th ICFD (2020), Sendai, Japan (virtual).

A. Karan, G. Dayma, C. Chauveau, F. Halter, Experimental and numerical validation of ammonia combustion in oxygen at high pressures and temperatures, 1st Low carbon conference - French and British section of the Combustion Institute (2020), Lille, France (virtual).

A. Karan, G. Dayma, C. Chauveau, F. Halter, Experimental characterisation of the reactive properties of premixed ammonia flames, 18th ICFD (2021), Sendai, Japan (virtual).

A. Karan, G. Dayma, C. Chauveau, F. Halter, High-pressure and temperature ammonia flame speeds, 13th ASPACC (2021), Abu Dhabi, UAE (virtual).

A. Karan, G. Dayma, C. Chauveau, F. Halter, A brief understanding of chemiluminescence signals of premixed ammonia air flames, 2nd Low carbon conference - French and British section of the Combustion Institute (2022), Cambridge, England.

A. Karan, G. Dayma, C. Chauveau, F. Halter, Insight into the inner structure of stretched premixed ammonia-air flames, 39th International symposium on combustion (2022), Vancouver, Canada.

A. Karan, G. Dayma, C. Chauveau, F. Halter, Chemiluminescence in premixed ammonia-air flames, Consortium : Ammonia for valuable clean energy systems (2022), Orléans, France.

A. Karan, G. Dayma, C. Chauveau, F. Halter, Investigation of curvature effects on the reactivity of premixed ammonia-air flames, 1st Symposium on Ammonia Energy (2022), Cardiff, Wales.

A. Karan, G. Dayma, C. Chauveau, F. Halter, Investigation of the chemiluminescence signature of ammonia flames, 19th ICFD (2022), Sendai, Japan (virtual).

A. Karan, G. Dayma, C. Chauveau, F. Halter, Characterisation of ammonia flames using their chemiluminescence signature, KAUST-Tohoku-Université d'Orléans core to core workshop (2022), KAUST, Saudi Arabia (virtual).

Poster presentation conferences/gatherings

A. Karan, G. Dayma, C. Chauveau, F. Halter, Experimental and numerical study of ammonia flames, Journée des doctorants d'ICARE (2021), Orleans, France.

ANNEXES

APPENDIX A

LAMINAR FLAME SPEEDS AND SENSITIVITY ANALYSES

A.1 Flame speed data for different test conditions

Experimental flame speeds have been thickened in yellow to account for the uncertainty. Black and red lines represent the values of the flame speed as predicted by Nakamura and Stagni respectively.

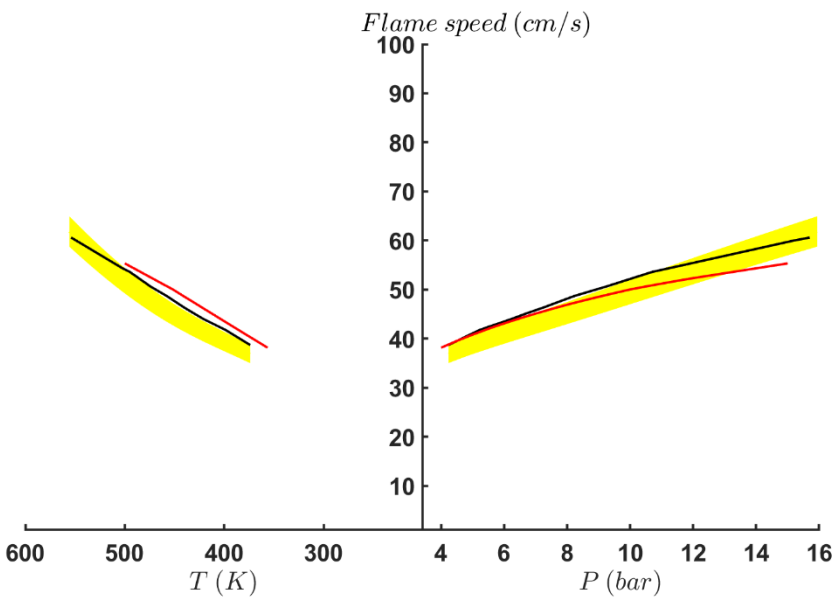

Figure A.1: Laminar flame speeds at p_0=2 bar, φ = 0.8, 49% Ar and 21% He

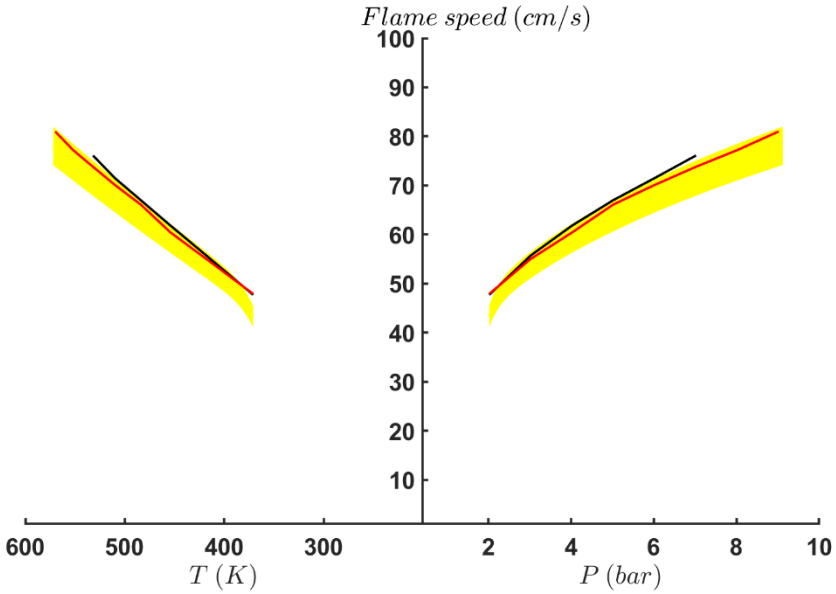

Figure A.2: Laminar flame speeds at p_0=1 bar, φ = 1.1, 49% Ar and 21% He

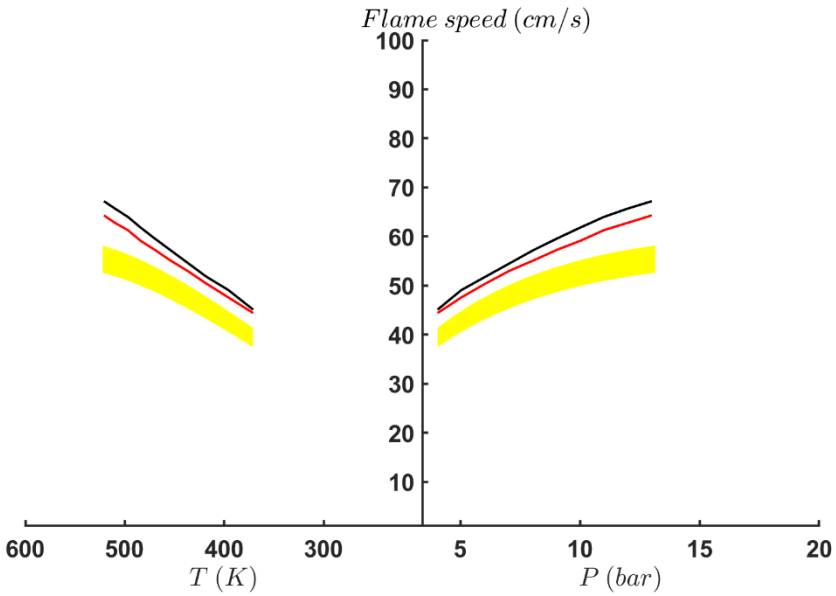

Figure A.3: Laminar flame speeds at p_0=2 bar, φ = 1.1, 49% Ar and 21% He

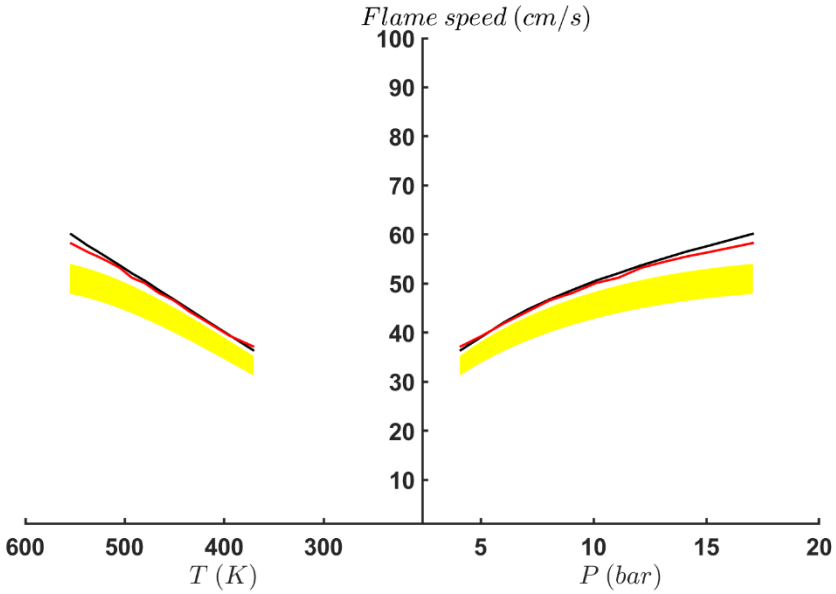

Figure A.4: Laminar flame speeds at p_0=2 bar, φ = 1.3, 49% Ar and 21% He

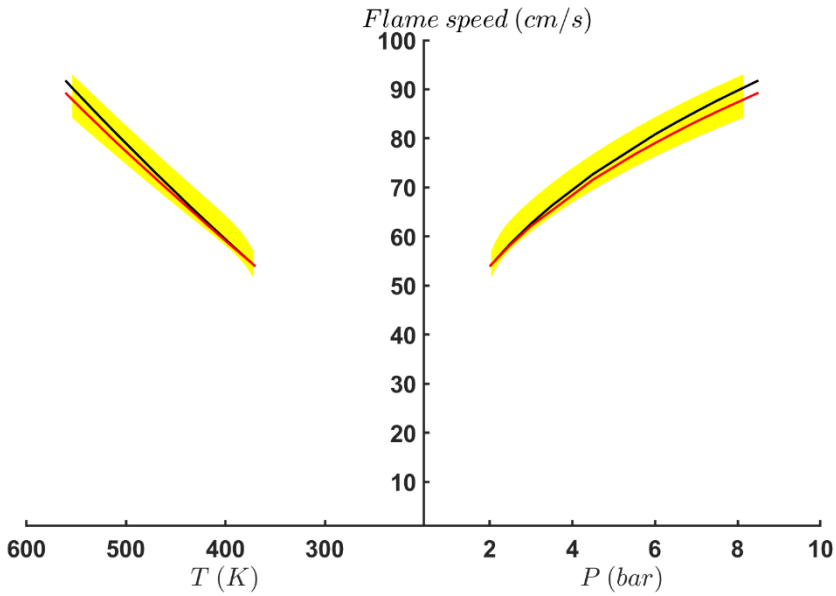

Figure A.5: Laminar flame speeds at p_0=1 bar, φ = 1.1, 49% He and 21% Ar

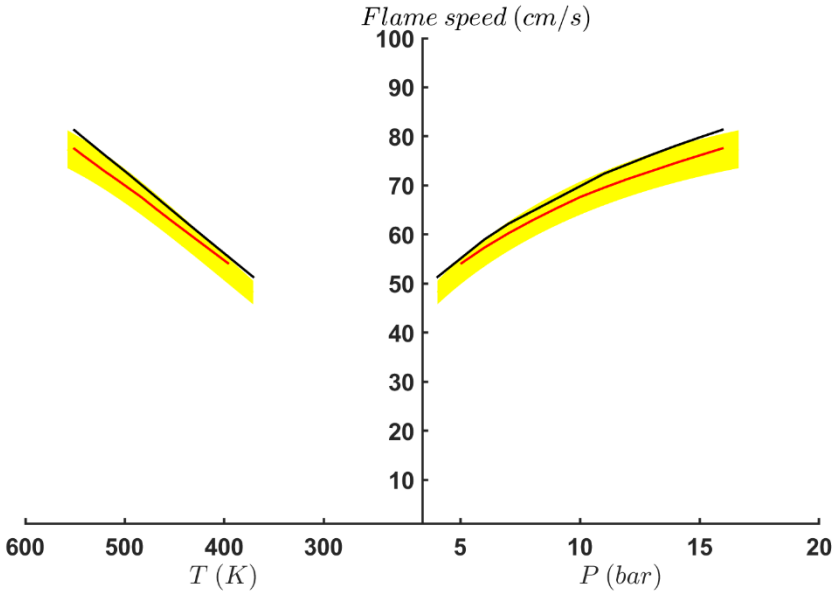

Figure A.6: Laminar flame speeds at p_0=2 bar, φ = 1.1, 49% He and 21% Ar

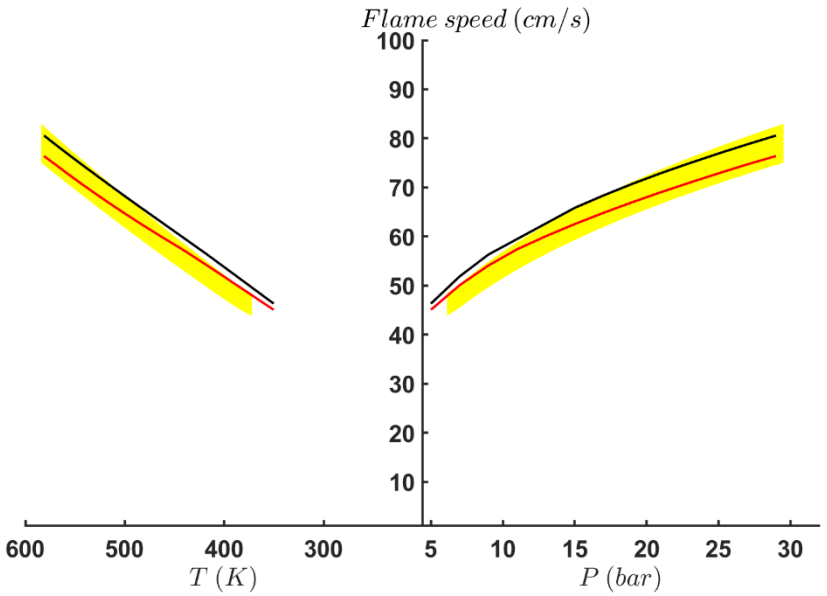

Figure A.7: Laminar flame speeds at p_0=3 bar, φ = 1.1, 49% He and 21% Ar

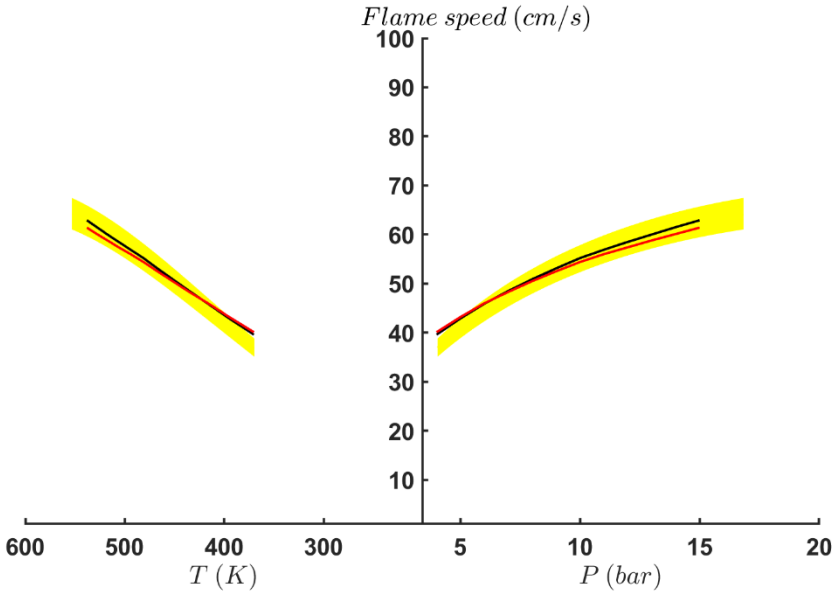

Figure A.8: Laminar flame speeds at p_0=2 bar, φ = 1.3, 49% He and 21% Ar

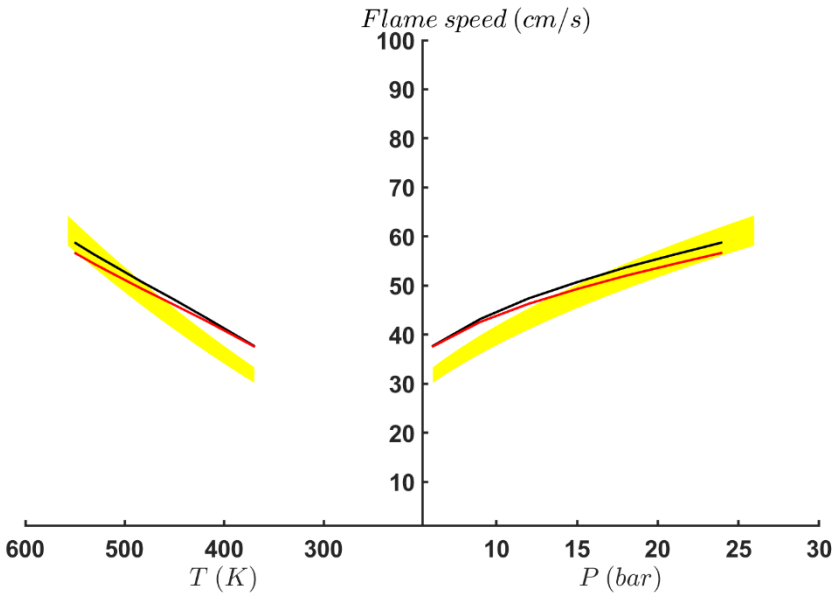

Figure A.9: Laminar flame speeds at p_0=4 bar, φ = 1.3, 49% He and 21% Ar

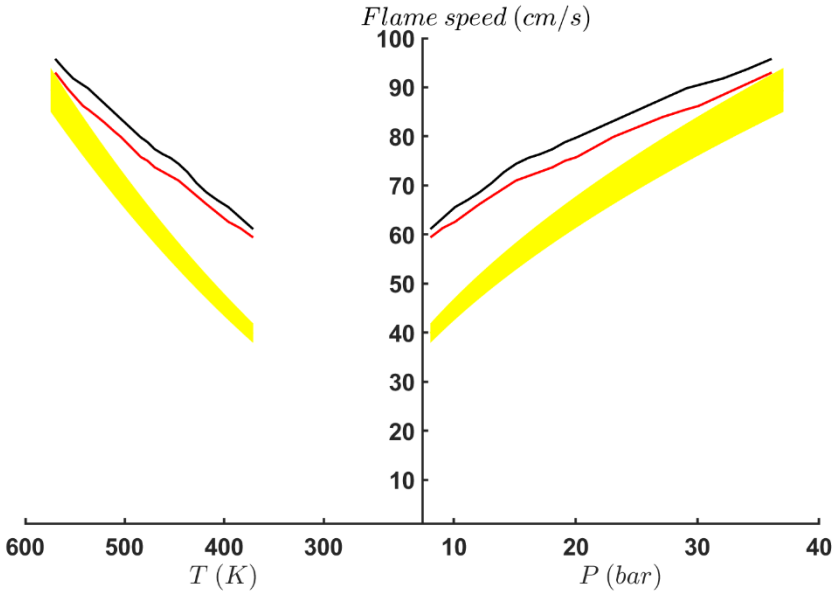

Figure A.10: Laminar flame speeds at p_0=4 bar, φ = 1.1, 70% He

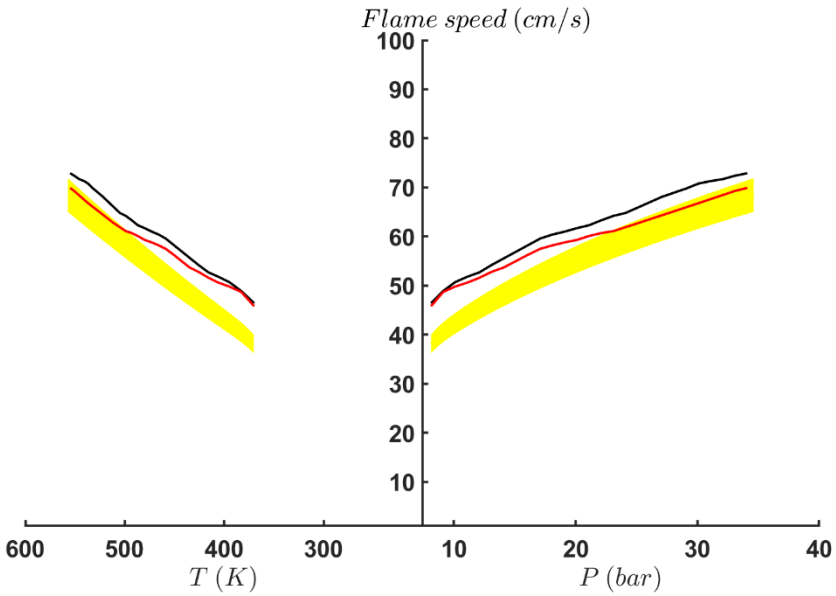

Figure A.11: Laminar flame speeds at p_0=4 bar, φ = 1.3, 70% He

A.2 Sensitivity analyses for different test conditions

From the sensitivity analyses for 2 different mechanisms: Stagni and Nakamura, it can be seen that the most dominant reaction irrespective of the intial condition is the one and the same.

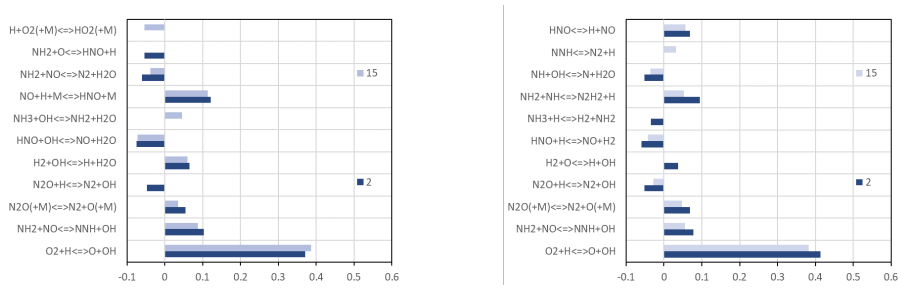

(a) Nakamura (b) Stagni

Figure A.12: Sensitivity analyses at p_0=2 bar, φ = 0.8, 49% Ar and 21% He

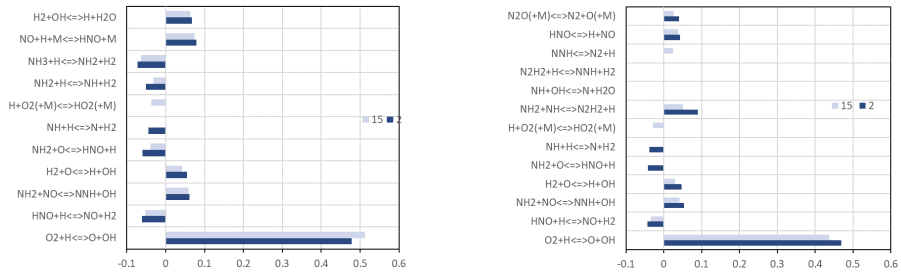

(a) Nakamura (b) Stagni

Figure A.13: Sensitivity analyses at p_0=2 bar, φ = 1.1, 49% Ar and 21% He

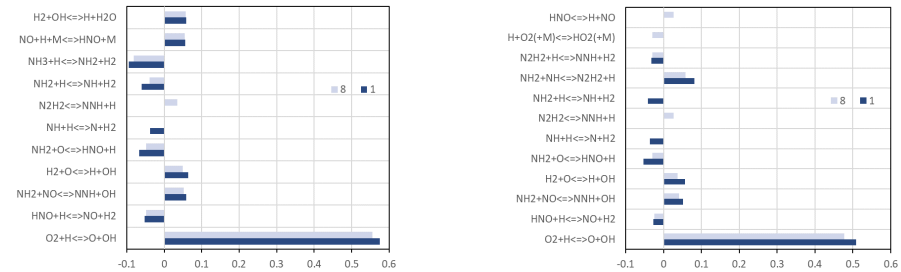

(a) Nakamura (b) Stagni

Figure A.14: Sensitivity analyses at p_0=1 bar, φ = 1.3, 49% Ar and 21% He

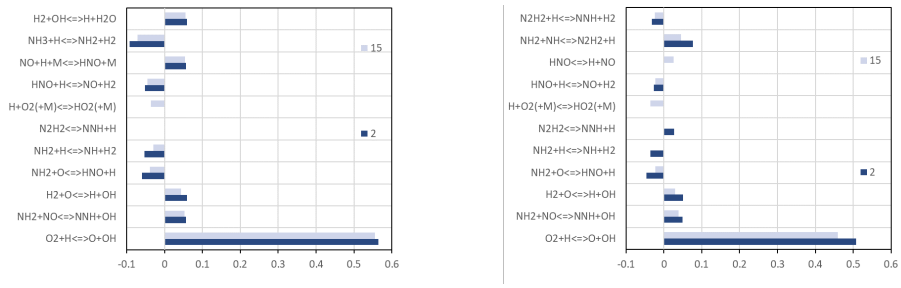

(a) Nakamura (b) Stagni

Figure A.15: Sensitivity analyses at p_0=2 bar, $\varphi = 1.3$, 49% Ar and 21% He

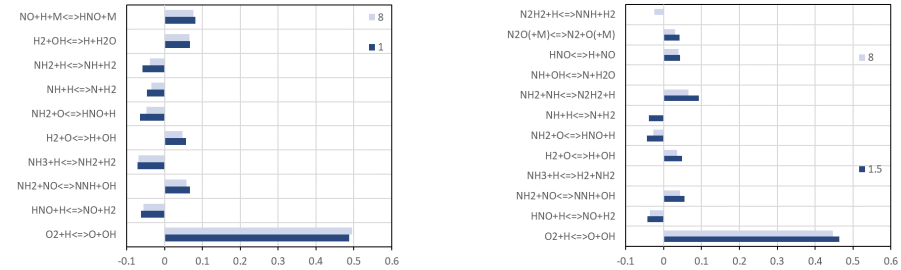

(a) Nakamura (b) Stagni

Figure A.16: Sensitivity analyses at p_0=1 bar, $\varphi = 1.1$, 49% He and 21% Ar

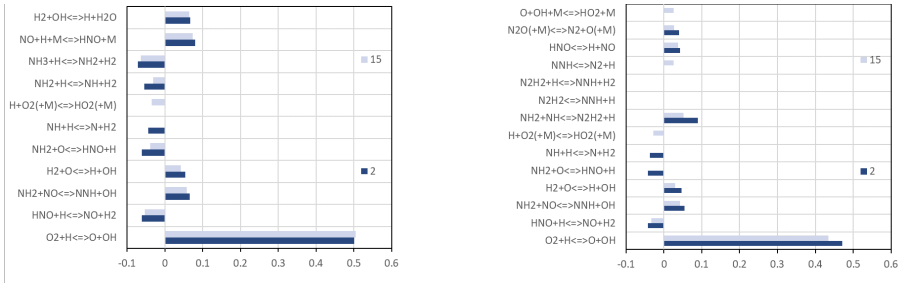

(a) Nakamura (b) Stagni

Figure A.17: Sensitivity analyses at p_0=2 bar, $\varphi = 1.1$, 49% He and 21% Ar

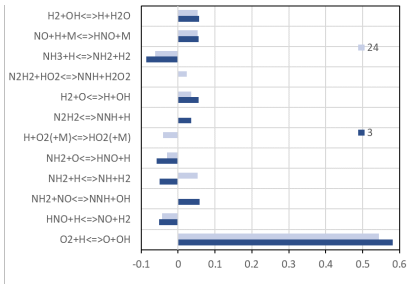

(a) Nakamura

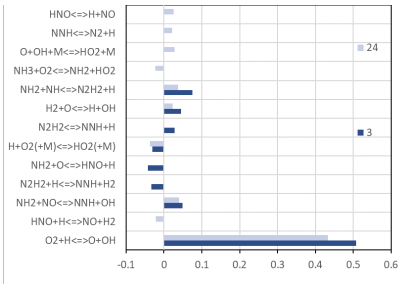

(b) Stagni

Figure A.18: Sensitivity analyses at p_0=3 bar, $\varphi = 1.3$, 49% He and 21% Ar

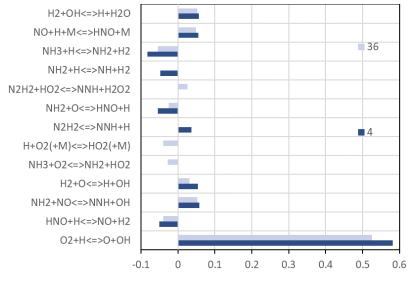

(a) Nakamura

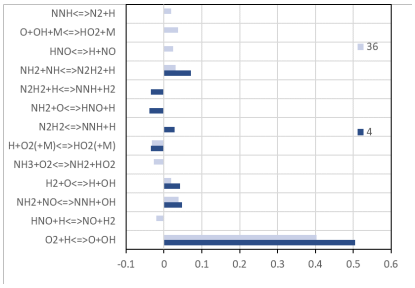

(b) Stagni

Figure A.19: Sensitivity analyses at p_0=3 bar, $\varphi = 1.3$, 49% He and 21% Ar

A.3 Sensitivity analysis at isothermal and isobaric conditions for Stagni

From this analysis, it is seen that irresepctive of the temperature or the pressure, there is only one dominant reaction.

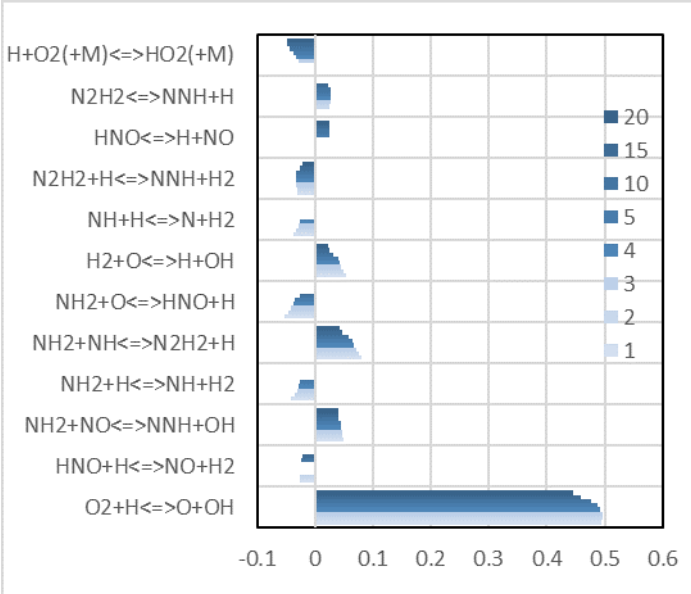

Figure A.20: Sensitivity analyses for isotherms at T=300 K over a pressure range of 1-20 bar for $\varphi = 1.3$, diluent mixture of 21% He and 49% Ar indicating that the dominant reaction is O2+H<=>O+OH and the recombination reaction of ammonia is relatively not sensitive.

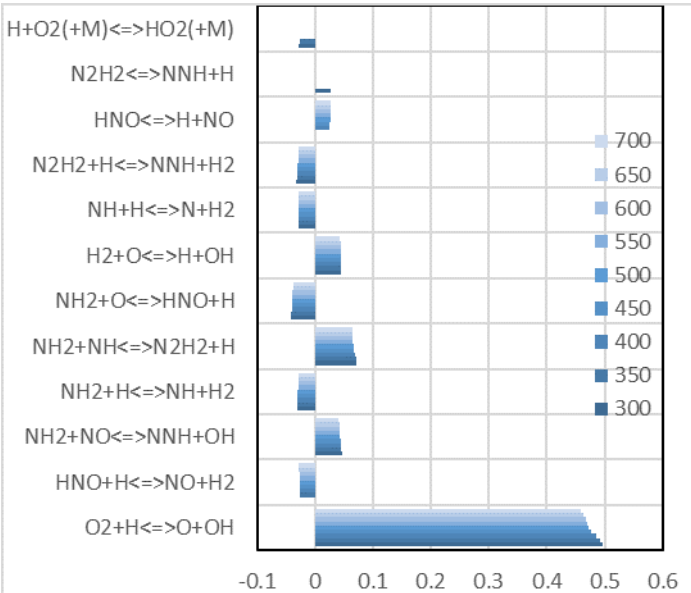

Figure A.21: Sensitivity analyses for isobars at p= 3 bar over a temperature range of 300-700 K for $\varphi = 1.3$, diluent mixture of 21% He and 49% Ar indicating that the dominant reaction is $O_2{}^+H$ and the recombination reaction of ammonia is relatively not sensitive although the magnitude of sensitivity to the flame speed is not the same for isobaric and isothermal cases.

APPENDIX B

INNER STRUCTURE OF STRETCHED PREMIXED FLAME

B.1 NH_2*

Figure B.1 depicts the images of the ammonia/air flame with the NH_2* filter and Figure B.2 represents the inverted Abel transformed images of Figure B.1. It can be seen that weak flames and in this case flames with Le<1 are subjugated to stronger curvature effects.

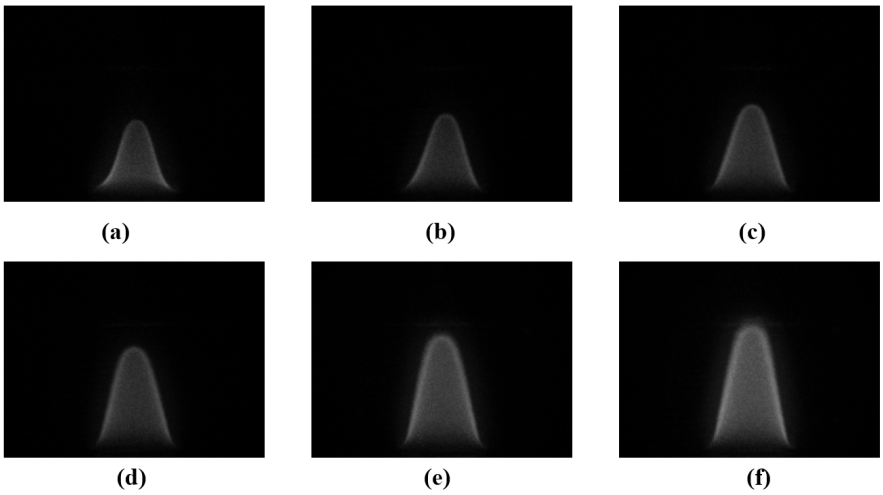

Figure B.1: Chemiluminescence images of NH_2* at φ = (a) 0.9, (b) 1, (c) 1.1, (d) 1.2, (e) 1.3, (f) 1.4.

Figure B.3 and Figure B.4 represents k1 and k2 for NH_2* φ=0.9 and 1.1.

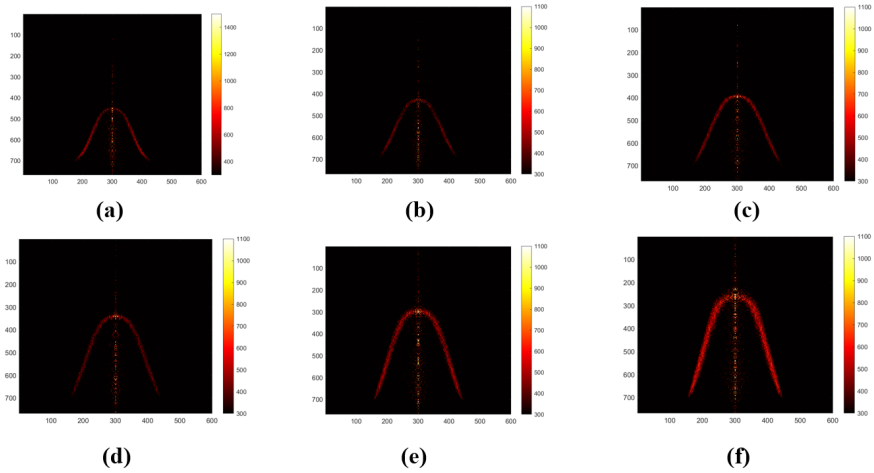

Figure B.2: Abel inversion transformed images of NH_2* at φ = (a) 0.9, (b) 1, (c) 1.1, (d) 1.2, (e) 1.3, (f) 1.4 depicting the positive curvature at the base of the flame for weak and stoichiometric conditions and the enhanced reactivity at the tip of the flame for φ = 1.1 and 1.2. The x and y axis represent the pixel and the color bar indicates the intensity of the pixel.

B.2 NH*

Figure B.5 depicts the images of the ammonia/air flame with the NH* filter and Figure B.6 represents the inverted Abel transformed images of Figure B.5. As seen in the case of NH_2*, flames with Le<1 endure stronger curvature effects. It can be also seen in both Figures B.5 and B.6 that the base of the flame is extremely bright and thicker irrespective of the flame being weak or strong. As mentioned in Chapter 8, there could be many reasons for the formation of NH* here.

Figure B.7, Figure B.8 and Figure B.9 represents k1 and k2 for NH* at φ= 0.9, 1.1 and 1.4. NH* undergoes a higher effect than NH_2*.

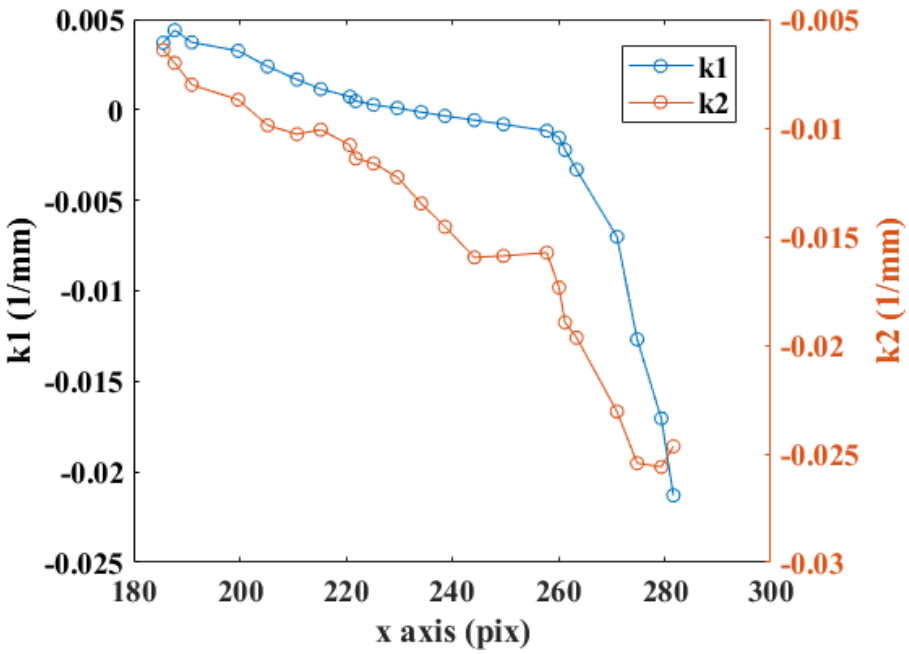

Figure B.3: k1 and k2 at $\varphi = 0.9$.

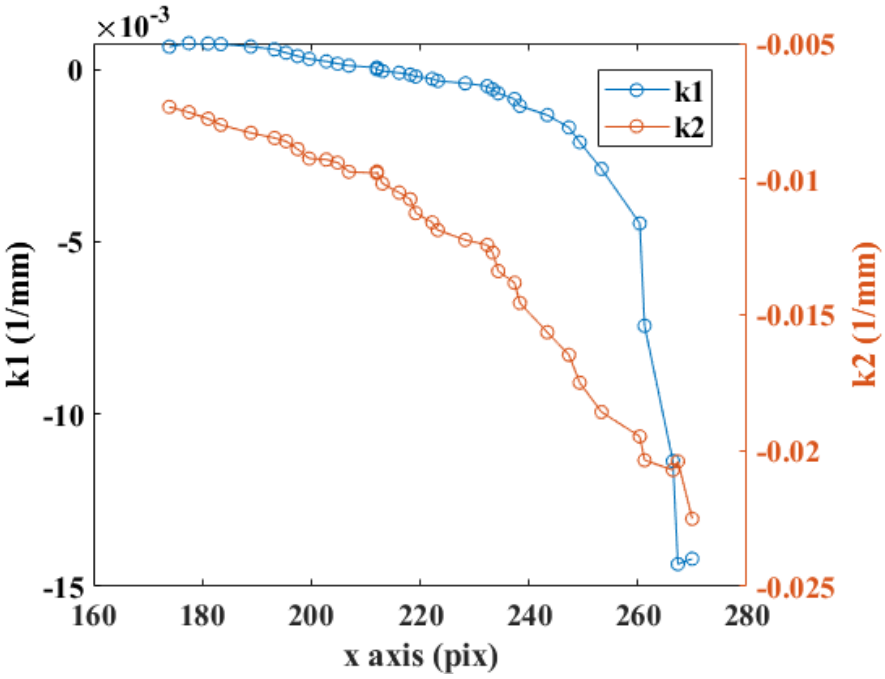

Figure B.4: k1 and k2 at $\varphi = 1.1$.

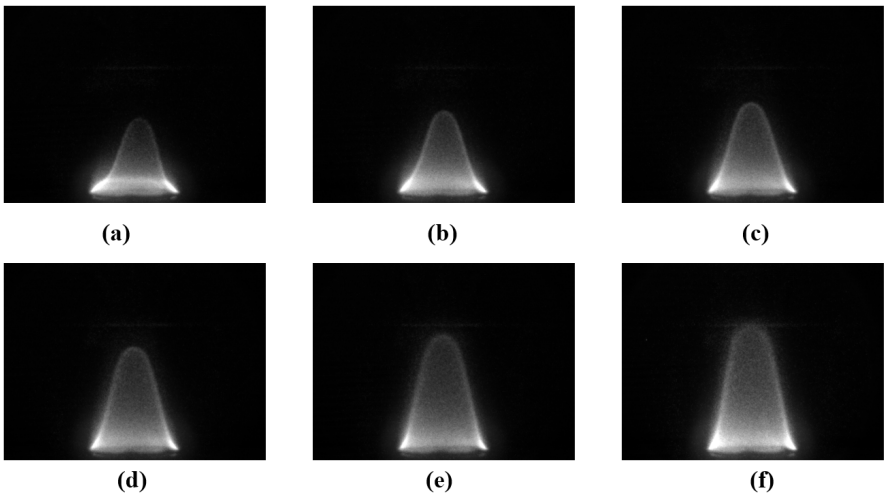

Figure B.5: Chemiluminescence images of NH* at φ = (a) 0.9, (b) 1, (c) 1.1, (d) 1.2, (e) 1.3, (f) 1.4.

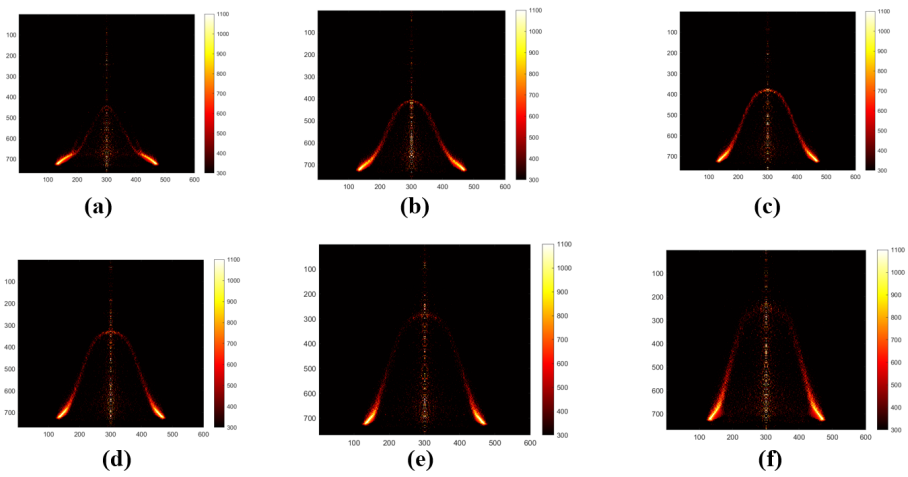

Figure B.6: Abel inversion transformed images of NH* at φ = (a) 0.9, (b) 1, (c) 1.1, (d) 1.2, (e) 1.3, (f) 1.4 depicting the positive curvature at the base of the flame for weak and stoichiometric conditions and the enhanced reactivity at the tip of the flame for φ= 1.1 and 1.2 with strong reactivity near the burner for all the cases. The x and y axis represent the pixel and the color bar indicates the intensity of the pixel.

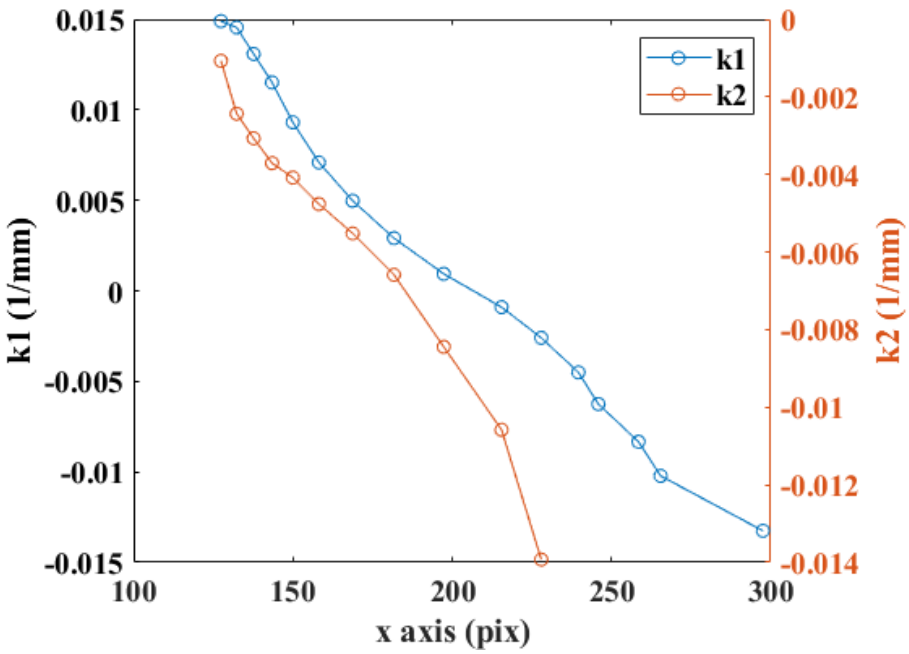

Figure B.7: k1 and k2 at $\varphi = 0.9$.

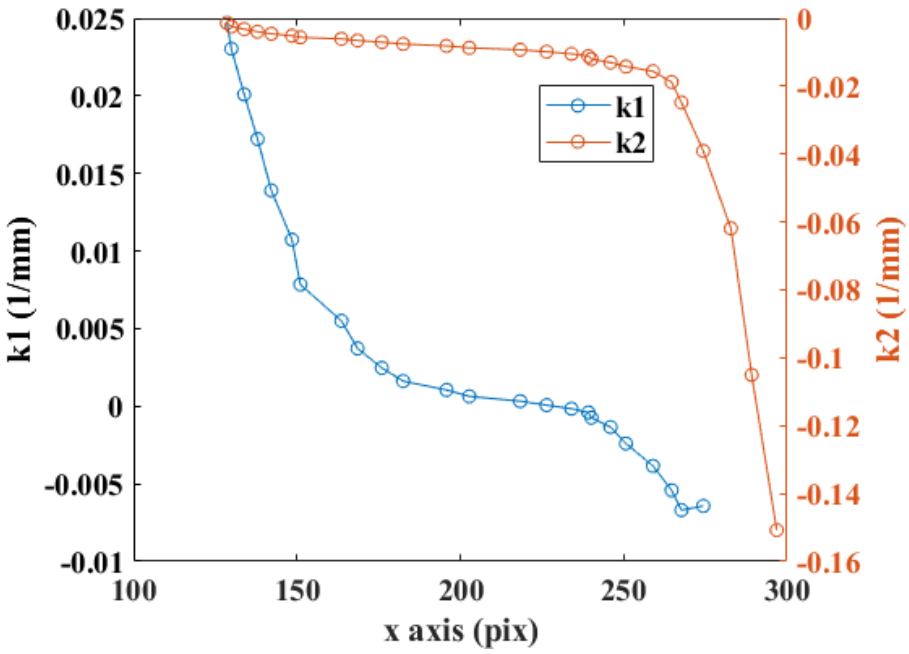

Figure B.8: k1 and k2 at $\varphi = 1.1$.

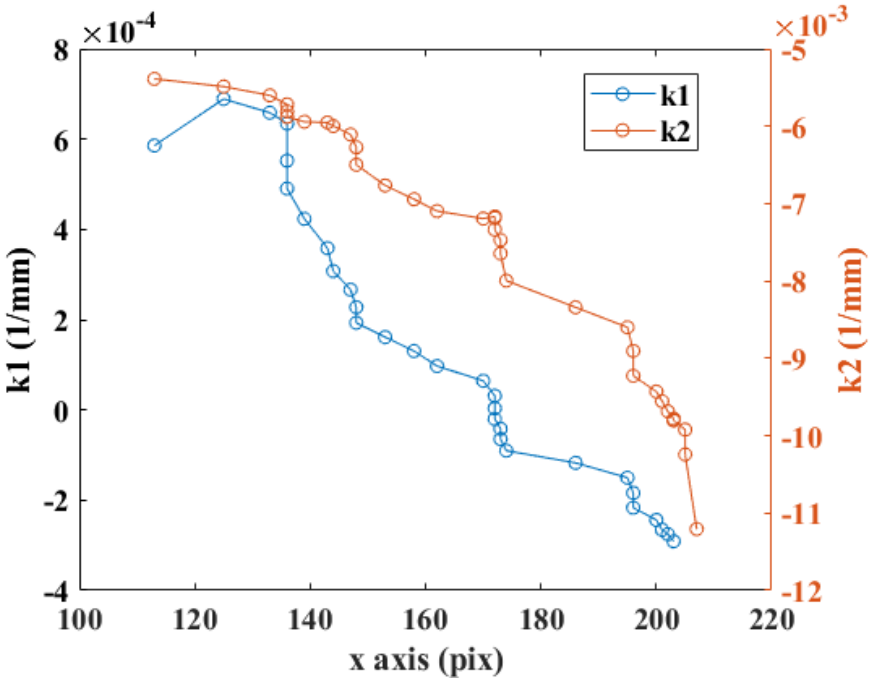

Figure B.9: k1 and k2 at $\varphi = 1.4$.

APPENDIX C

CHEMICAL AND DYNAMICAL ANALYSES OF A PREMIXED FLAME

The fixed ROI is represented in figure C.1 with the longest flame possible (at φ=1.4)

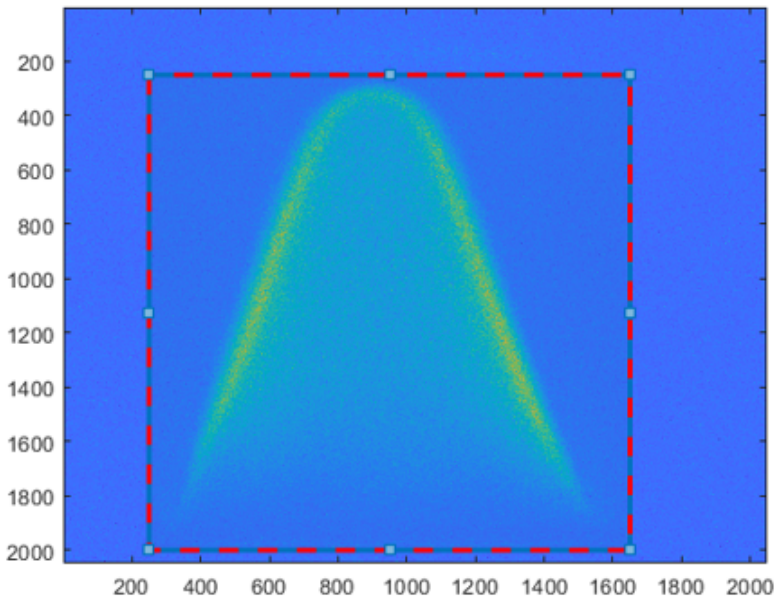

Figure C.1: Image captured at an exposure time of 1 ms with the ROI.

The images of LED lamp captured with the filter and without the filter.

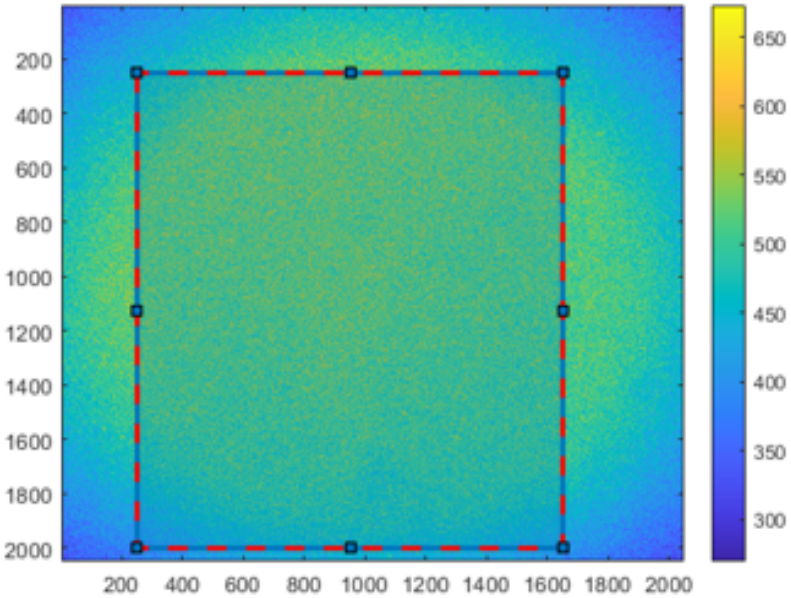

Figure C.2: Image captured at an exposure time of 1 ms, potentiometer of LED lamp set at k=6 with the filter.

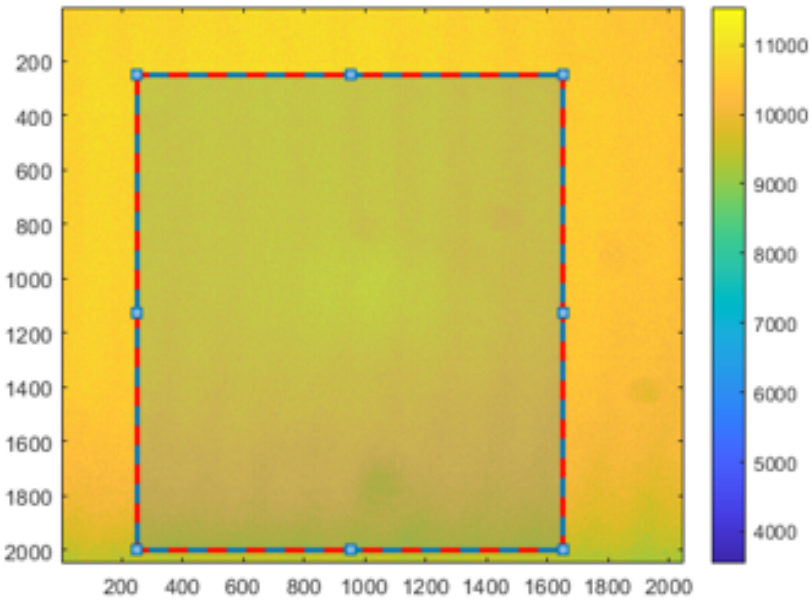

Figure C.3: Image captured at an exposure time of 1 ms, potentiometer of LED lamp set at k=6 without the filter.

Flame-acoustic interactions

The different parameters used to characterise the reactvity with the curvature for different equivalence ratio is provided here. Each of the parameters is plotted along the contour of the front.

Phi=1.0

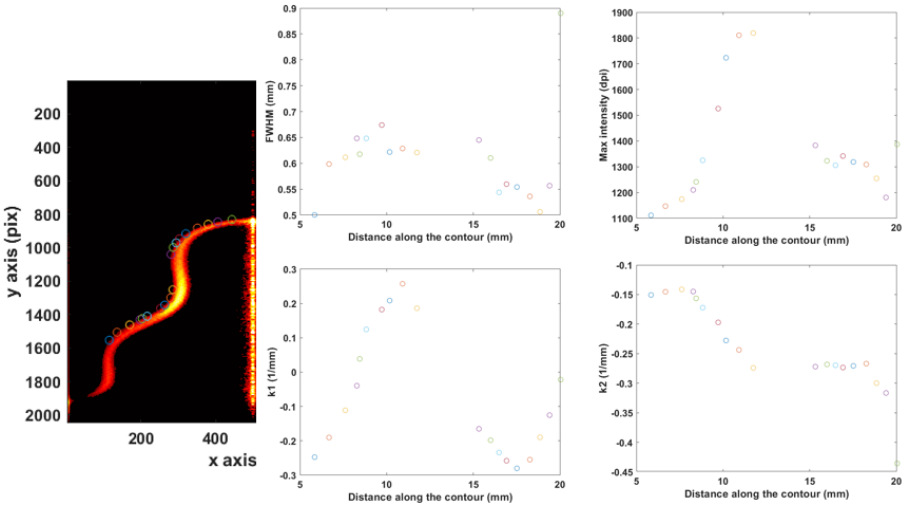

Figure C.4: Thickness, maximum intensity, k1 and k2 as a function of contour at φ=1.0

The thickness does not vary much along the contour but the variation in k1 along the contour implies that it contributes to the shape of the flame. The value of k2 continuously decreases as a function of height. The maximum intensity takes a bell-shaped profile implying that the maximum reactivity happens at around half of the maximum height of the flame.

Phi=1.1

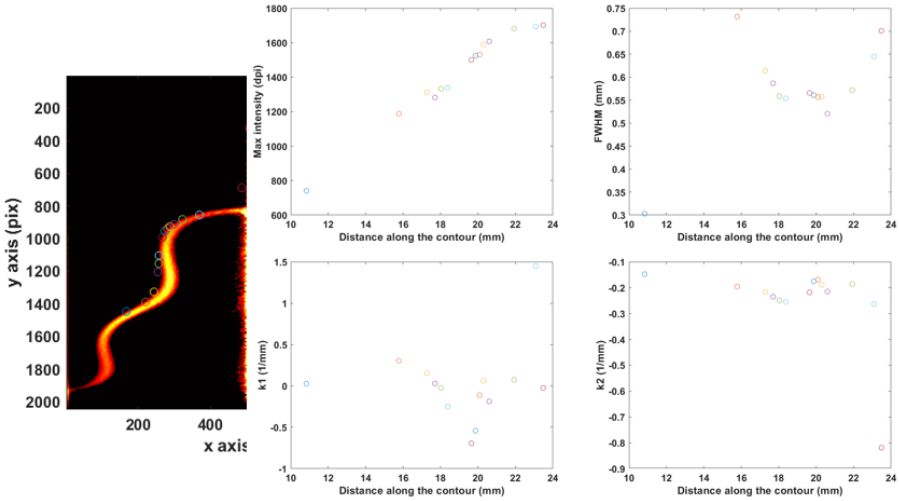

Figure C.5: Thickness, maximum intensity, k1 and k2 as a function of contour at φ=1.1

Here, the chosen points are at around midway of the total flame height. There is a small change of thickness and k1. The maximum intensity tnds to continuously increase with k2 continuously decreasing.

Phi=1.2

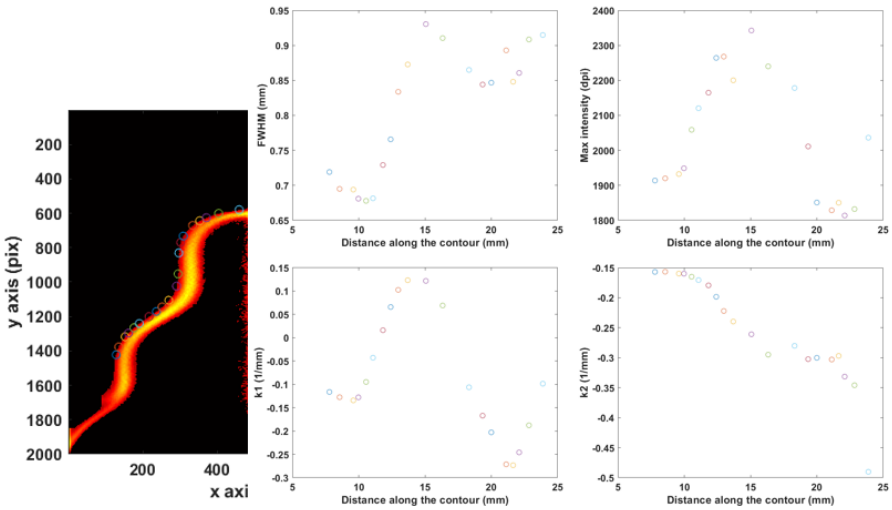

Figure C.6: Thickness, maximum intensity, k1 and k2 as a function of contour at φ=1.2

In this case, the variation of k1 and thickness seem to go hand in hand. The trend of k2 cotinues to decrease with height whereas the maximum intensity continues to take the bell-shaped profile implying once again that the maximum reactivity is most likely near half of the total height of the flame. This could be explained with the preferential diffusion effect of lighter species over the convective veocit of the flow.

Phi=1.3

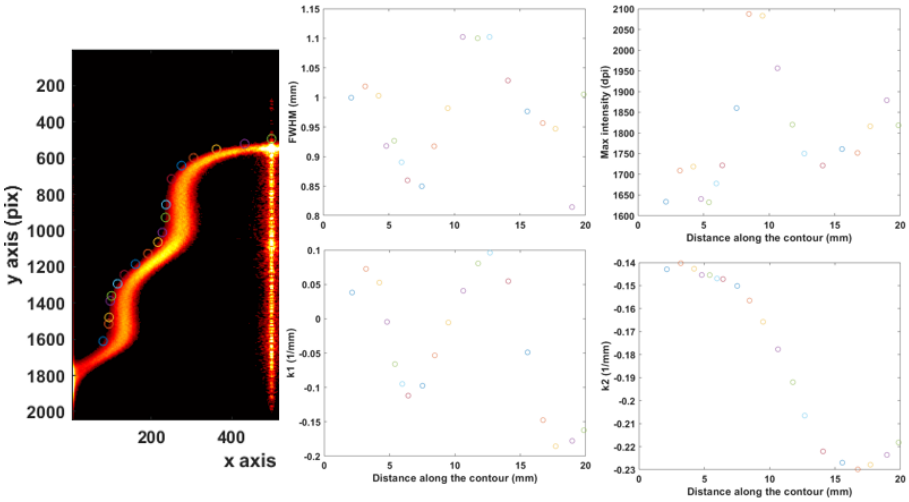

Figure C.7: Thickness, maximum intensity, k1 and k2 as a function of contour at φ=1.3

Similar trends as φ=1.2 is seen here with the change of thickness becoming more prominent.

Phi=1.4

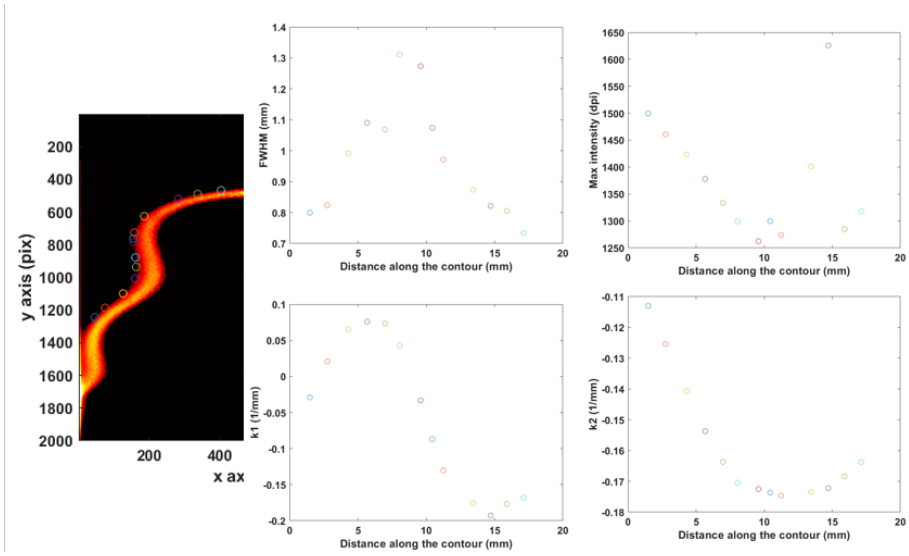

Figure C.8: Thickness, maximum intensity, k1 and k2 as a function of contour at φ=1.4

The maximum variation in thickness is seen in this case. The profile of maximum intensity slightly differs from the other as there is a slight decrease followed by an increase with a subsequent decrease along the contour. This could be due to stronger diffusion effects near the base of the flame.

BIBLIOGRAPHY

[1] E. C. Okafor, Y. Naito, S. Colson, A. Ichikawa, T. Kudo, A. Hayakawa, H. Kobayashi, Measurement and modelling of the laminar burning velocity of methane-ammonia-air flames at high pressures using a reduced reaction mechanism, Combust. Flame 204 (2019) 162–175.

[2] S. J. Klippenstein, M. Pfeifle, A. W. Jasper, P. Glarborg, Theory and modeling of relevance to prompt-NO formation at high pressure, Combust. Flame 195 (2018) 3–17.

[3] Y. Zhang, O. Mathieu, E. L. Petersen, G. Bourque, H. J. Curran, Assessing the predictions of a NO_x kinetic mechanism on recent hydrogen and syngas experimental data, Combust. Flame 182 (2017) 122–141.

[4] A. Konnov, Implementation of the NCN pathway of prompt-NO formation in the detailed reaction mechanism, Combust. Flame 156 (2009) 2093–2105.

[5] O. Mathieu, E. L. Petersen, Experimental and modeling study on the high-temperature oxidation of ammonia and related NO_x chemistry, Combust. Flame 162 (2015) 554–570.

[6] H. Kobayashi, A. Hayakawa, K. K. A. Somarathne, E. C. Okafor, Science and technology of ammonia combustion, Proc. Combust. Inst. 37 (2019) 109–133.

[7] R. C. da Rocha, M. Costa, X.-S. Bai, Chemical kinetic modelling of ammonia/hydrogen/air ignition, premixed flame propagation and NO emission, Fuel 246 (2019) 24–33.

[8] H. Nakamura, S. Hasegawa, Combustion and ignition characteristics of ammonia/air mixtures in a micro flow reactor with a controlled temperature profile, Proc. Combust. Inst. 36 (2017) 4217–4226.

[9] A. Stagni, C. Cavallotti, S. Arunthanayothin, Y. Song, O. Herbinet, F. Battin-Leclerc, T. Faravelli, An experimental, theoretical and kinetic-modeling study of the gas-phase oxidation of ammonia, React. Chem. Eng. 5 (2020) 696–711.

[10] K. P. Shrestha, L. Seidel, T. Zeuch, F. Mauss, Detailed kinetic mechanism for the oxidation of ammonia including the formation and reduction of nitrogen oxides, Energy Fuels 32 (2018) 10202–10217.

[11] E. Hu, X. Li, X. Meng, Y. Chen, Y. Cheng, Y. Xie, Z. Huang, Laminar flame speeds and ignition delay times of methane–air mixtures at elevated temperatures and pressures 158 1–10.

[12] M. O. Vigueras-Zúñiga, M. E. Tejeda-del Cueto, S. Mashruk, M. Kovaleva, C. L. Ordóñez-Romero, A. Valera-Medina, Methane/Ammonia Radical Formation during High Temperature Reactions in Swirl Burners 14 6624.

[13] R. Ichimura, K. Hadi, N. Hashimoto, A. Hayakawa, H. Kobayashi, O. Fujita, Extinction limits of an ammonia/air flame propagating in a turbulent field 246 178–186.

[14] A. Birbaud, D. Durox, S. Candel, Upstream flow dynamics of a laminar premixed conical flame submitted to acoustic modulations 146 541–552.

[15] F. Halter, Z. Chen, G. Dayma, C. Bariki, Y. Wang, P. Dagaut, C. Chauveau, Development of an optically accessible apparatus to characterize the evolution of spherically expanding flames under constant volume conditions, Combust. Flame 212 (2020) 165–176.

[16] F. Halter, G. Dayma, Z. Serinyel, P. Dagaut, C. Chauveau, Laminar flame speed determination at high pressure and temperature conditions for kinetic schemes assessment, Proc. Combust. Inst. 38 (2021) 2449–2457.

[17] A. Mouze-Mornettas, H. Keck, Y. Wang, Z. Chen, G. Dayma, C. Chauveau, F. Halter, Effect of wall heat transfer on the dynamics of premixed spherical expanding flames 29 101227.

[18] P. Dagaut, P. Glarborg, M. Alzueta, The oxidation of hydrogen cyanide and related chemistry, Prog. Energy Combust. Sci. 34 (2008) 1–46.

[19] J. Otomo, M. Koshi, T. Mitsumori, H. Iwasaki, K. Yamada, Chemical kinetic modeling of ammonia oxidation with improved reaction mechanism for ammonia/air and ammonia/hydrogen/air combustion, Int. J. Hydrog. Energy 43 (2018) 3004–3014.

[20] Q. H, N. K. Das, Ammonia - Molecule of the Month June 2013 [Archived version] 500417 BytesArtwork Size: 500417 Bytes Publisher: figshare.

[21] Haber process Page Version ID: 1085813519.

[22] Op-ed: What's the verdict on ammonia as fuel or as hydrogen carrier?

[23] The Kyoto Protocol in a Global Perspective, https://www.researchgate.net/publication/228373949_The_Kyoto_protocol _in_a_global_perspective.

[24] Paris Agreement, https://www.researchgate.net/publication/332524888 _Paris_Agreement.

[25] https://nh3fuelassociation.org/introduction/.

[26] http://claverton-energy.com/cms4/wp-content/files/NH3$_{b}us_{1}945_{J}InstPetrol31_{P}g213.pdf$.

[27] W. Cornelius, L. W. Huellmantel, H. R. Mitchell, Ammonia as an Engine Fuel, 650052.

[28] The Best Film Archives, X-15 Rocket Plane | The World's Fastest Airplane | NASA Documentary | 1962.

[29] A. Valera-Medina, D. Pugh, P. Marsh, G. Bulat, P. Bowen, Preliminary study on lean premixed combustion of ammonia-hydrogen for swirling gas turbine combustors 42 24495–24503.

[30] S. Frigo, R. Gentili, Analysis of the behaviour of a 4-stroke Si engine fuelled with ammonia and hydrogen 38 1607–1615.

[31] C. Zamfirescu, I. Dincer, Ammonia as a green fuel and hydrogen source for vehicular applications 90 729–737.

[32] A. research projects agency-energy (ARPAE), U.S. Department of Energy,)Renewable energy to fuels through utilization of energy-dense liquids(refuel).

[33] Why the Shipping Industry Is Betting Big on Ammonia - IEEE Spectrum.

[34] A. C. Egerton, The Ammonia Flame 89 270–270.

[35] R. J. Strutt, The Ammonia Flame 89 320–320.

[36] M. Bodenstein, The Mechanism of the Catalytic Combustion of Ammonia 71 353.

[37] P. V. Blarigan, 1advanced Internal Combustion Engine Research.

[38] A. Konnov, J. D. Ruyck, Kinetic Modeling of the Thermal Decomposition of Ammonia 152 23–37.

[39] K. Mann, "Premixed ammonia-methane-air combustion.".

[40] J. F. Grcar, P. Glarborg, J. B. Bell, M. S. Day, A. Loren, A. D. Jensen, Effects of mixing on ammonia oxidation in combustion environments at intermediate temperatures 30 1193–1200.

[41] P. Glarborg, Fuel nitrogen conversion in solid fuel fired systems 29 89–113.

[42] N. A. Hussein, A. Valera-Medina, A. S. Alsaegh, Ammonia- hydrogen combustion in a swirl burner with reduction of NOx emissions 158 2305–2310.

[43] A. J. Reiter, S.-C. Kong, Demonstration of Compression-Ignition Engine Combustion Using Ammonia in Reducing Greenhouse Gas Emissions 22 2963–2971.

[44] T. Cai, D. Zhao, X. Li, B. Shi, J. Li, Mitigating NO emissions from an ammonia-fueled micro-power system with a perforated plate implemented 401 123848.

[45] F. R. Westlye, A. Ivarsson, J. Schramm, Experimental investigation of nitrogen based emissions from an ammonia fueled SI-engine 111 239–247.

[46] Industry prepares ammonia for a second life as a fuel for the future.

[47] C. Lhuillier, P. Brequigny, F. Contino, C. Mounaïm-Rousselle, EXPERIMENTAL STUDY ON NH3/H2/AIR COMBUSTION IN SPARK-IGNITION ENGINE CONDITIONS 13.

[48] X. Han, Z. Wang, M. Costa, Z. Sun, Y. He, K. Cen, Experimental and kinetic modeling study of laminar burning velocities of NH3/air, NH3/H2/air, NH3/CO/air and NH3/CH4/air premixed flames 206 214–226.

[49] V. Cechetto, L. Di Felice, J. A. Medrano, C. Makhloufi, J. Zuniga, F. Gallucci, H2 production via ammonia decomposition in a catalytic membrane reactor 216 106772.

[50] K. E. Lamb, M. D. Dolan, D. F. Kennedy, Ammonia for hydrogen storage; A review of catalytic ammonia decomposition and hydrogen separation and purification 44 3580–3593.

[51] D. Cheddie, Ammonia as a Hydrogen Source for Fuel Cells: A Review, in: D. Minic (Ed.) Hydrogen Energy - Challenges and Perspectives, InTech.

[52] H. Xing, C. Stuart, S. Spence, H. Chen, Fuel Cell Power Systems for Maritime Applications: Progress and Perspectives 13 1213.

[53] F. Jiao, B. Xu, Electrochemical Ammonia Synthesis and Ammonia Fuel Cells 31 1805173.

[54] A. Karan, G. Dayma, C. Chauveau, F. Halter, Experimental study and numerical validation of oxy-ammonia combustion at elevated temperatures and pressures 236 111819.

[55] D. Andrews, P. Gray, Combustion of Ammonia Supported by Oxygen, Nitrous Oxide or Nitric Oxide: Laminar Flame Propagation at Low Pressures in Binary Mixtures, Combustion and Flame 8 (1964) 113–126.

[56] X. Han, Z. Wang, M. Costa, Z. Sun, Y. He, K. Cen, Experimental and kinetic modeling study of laminar burning velocities of NH_3/air, NH_3/H_2/air, NH_3/CO/air and NH_3/CH_4/air premixed flames, Combust. Flame 206 (2019) 214–226.

[57] A. Hayakawa, T. Goto, R. Mimoto, Y. Arakawa, T. Kudo, H. Kobayashi, Laminar burning velocity and markstein length of ammonia/air premixed flames at various pressures, Fuel 159 (2015) 98–106.

[58] C. Lhuillier, P. Brequigny, F. Contino, C. Mounaïm-Rousselle, Experimental study on NH_3/H_2/air combustion in spark-ignition engine conditions, 11th Mediterranean Combustion Symposium (2019).

[59] C. Mørch, A. Bjerre, M. Gøttrup, S. Sorenson, J. Schramm, Ammonia/hydrogen mixtures in an SI-engine: Engine performance and analysis of a proposed fuel system, Fuel 90 (2011) 854–864.

[60] C. Duynslaegher, H. Jeanmart, J. Vandooren, Ammonia combustion at elevated pressure and temperature conditions, Fuel 89 (2010) 3540–3545.

[61] A. Goldmann, F. Dinkelacker, Approximation of laminar flame characteristics on premixed ammonia/hydrogen/nitrogen/air mixtures at elevated temperatures and pressures, Fuel 224 (2018) 366–378.

[62] C. Lhuillier, P. Brequigny, N. Lamoureux, F. Contino, C. Mounaïm-Rousselle, Experimental investigation on laminar burning velocities of ammonia/hydrogen/air mixtures at elevated temperatures, Fuel 263 (2020) 116653.

[63] J. Li, H. Huang, N. Kobayashi, Z. He, Y. Nagai, Study on using hydrogen and ammonia as fuels: Combustion characteristics and NO_x formation: Hydrogen and ammonia as fuels, Int. J. Energy Res. 38 (2014) 1214–1223.

[64] K. P. Shrestha, C. Lhuillier, A. A. Barbosa, P. Brequigny, F. Contino, C. Mounaïm-Rousselle, L. Seidel, F. Mauss, An experimental and modeling study of ammonia with enriched oxygen content and ammonia/hydrogen laminar flame speed at elevated pressure and temperature, Proc. Combust. Inst. (2020) 2163–2174.

[65] Y. Xia, G. Hashimoto, K. Hadi, N. Hashimoto, A. Hayakawa, H. Kobayashi, O. Fujita, Turbulent burning velocity of ammonia/oxygen/nitrogen premixed flame in O2-enriched air condition 268 117383.

[66] G. Yin, J. Li, M. Zhou, J. Li, C. Wang, E. Hu, Z. Huang, Experimental and kinetic study on laminar flame speeds of ammonia/dimethyl ether/air under high temperature and elevated pressure 238 111915.

[67] D. Hou, Z. Zhang, Q. Cheng, B. Liu, M. Zhou, G. Li, Experimental and kinetic studies of laminar burning velocities of ammonia with high Lewis number at elevated pressures 320 123913.

[68] P. Ronan, B. Pierre, M.-R. Christine, D. Guillaume, H. Fabien, Laminar flame speed of ethanol/ammonia blends–An experimental and kinetic study 10 100052.

[69] A. Hayakawa, Y. Hirano, E. C. Okafor, H. Yamashita, T. Kudo, H. Kobayashi, Experimental and numerical study of product gas characteristics of ammonia/air premixed laminar flames stabilized in a stagnation flow 38 2409–2417.

[70] K. N. Osipova, O. P. Korobeinichev, A. G. Shmakov, Chemical structure and laminar burning velocity of atmospheric pressure premixed ammonia/hydrogen flames 46 39942–39954.

[71] Z. Wang, X. Han, Y. He, R. Zhu, Y. Zhu, Z. Zhou, K. Cen, Experimental and kinetic study on the laminar burning velocities of NH3 mixing with CH3OH and C2H5OH in premixed flames 229 111392.

[72] K. P. Shrestha, C. Lhuillier, A. A. Barbosa, P. Brequigny, F. Contino, C. Mounaïm-Rousselle, L. Seidel, F. Mauss, An experimental and modeling study of ammonia with enriched oxygen content and ammonia/hydrogen laminar flame speed at elevated pressure and temperature, Proceedings of the Combustion Institute 38 (2021) 2163–2174.

[73] X. Han, Z. Wang, Y. He, Y. Zhu, K. Cen, Experimental and kinetic modeling study of laminar burning velocities of NH3/syngas/air premixed flames 213 1–13.

[74] D. Wang, C. Ji, Z. Wang, S. Wang, T. Zhang, J. Yang, Measurement of oxy-ammonia laminar burning velocity at normal and elevated temperatures, Fuel 279 (2020) 118425.

[75] C. Lhuillier, P. Brequigny, N. Lamoureux, F. Contino, C. Mounaïm-Rousselle, Experimental investigation on laminar burning velocities of ammonia/hydrogen/air mixtures at elevated temperatures 263 116653.

[76] Q. Liu, X. Chen, J. Huang, Y. Shen, Y. Zhang, Z. Liu, The characteristics of flame propagation in ammonia/oxygen mixtures 363 187–196.

[77] B. Mei, X. Zhang, S. Ma, M. Cui, H. Guo, Z. Cao, Y. Li, Experimental and kinetic modeling investigation on the laminar flame propagation of ammonia under oxygen enrichment and elevated pressure conditions 210 236–246.

[78] A. Hayakawa, Y. Arakawa, R. Mimoto, K. K. A. Somarathne, T. Kudo, H. Kobayashi, Experimental investigation of stabilization and emission characteristics of ammonia/air premixed flames in a swirl combustor 42 14010–14018.

[79] A. Ichikawa, A. Hayakawa, Y. Kitagawa, K. Kunkuma Amila Somarathne, T. Kudo, H. Kobayashi, Laminar burning velocity and Markstein length of ammonia/hydrogen/air premixed flames at elevated pressures 40 9570–9578.

[80] A. Hayakawa, T. Goto, R. Mimoto, Y. Arakawa, T. Kudo, H. Kobayashi, Laminar burning velocity and Markstein length of ammonia/air premixed flames at various pressures 159 98–106.

[81] J. Li, H. Huang, N. Kobayashi, Z. He, Y. Nagai, Study on using hydrogen and ammonia as fuels: Combustion characteristics and NO $_x$ formation: Hydrogen and ammonia as fuels 38 1214–1223.

[82] P. Kumar, T. R. Meyer, Experimental and modeling study of chemical-kinetics mechanisms for H2–NH3–air mixtures in laminar premixed jet flames 108 166–176.

[83] J. Lee, J. Kim, J. Park, O. Kwon, Studies on properties of laminar premixed hydrogen-added ammonia/air flames for hydrogen production 35 1054–1064.

[84] K. Takizawa, A. Takahashi, K. Tokuhashi, S. Kondo, A. Sekiya, Burning velocity measurements of nitrogen-containing compounds 155 144–152.

[85] T. Jabbour, D. Clodic, Burning Velocity and Refrigerant Flammability Classification 110 522–533.

[86] U. Pfahl, M. Ross, J. Shepherd, K. Pasamehmetoglu, C. Unal, Flammability limits, ignition energy, and flame speeds in H2–CH4–NH3–N2O–O2–N2 mixtures 123 140–158.

[87] P. D. Ronney, Effect of Chemistry and Transport Properties on Near-Limit Flames at Microgravity 59 123–141.

[88] V. F. Zakaznov, L. A. Kursheva, Z. I. Fedina, Determination of normal flame velocity and critical diameter of flame extinction in ammonia-air mixture 14 710–713.

[89] D. Andrews, P. Gray, Combustion of ammonia supported by oxygen, nitrous oxide or nitric oxide: Laminar flame propagation at low pressures in binary mixtures 8 113–126.

[90] H. Tian, P. Karachalios, I. Angelidaki, I. A. Fotidis, A proposed mechanism for the ammonia-LCFA synergetic co-inhibition effect on anaerobic digestion process 349 574–580.

[91] H. Xiao, A. Valera-Medina, Chemical Kinetic Mechanism Study on Premixed Combustion of Ammonia/Hydrogen Fuels for Gas Turbine Use 139 081504.

[92] J. A. Miller, M. D. Smooke, R. M. Green, R. J. Kee, Kinetic Modeling of the Oxidation of Ammonia in Flames 34 149–176.

[93] C. Duynslaegher, H. Jeanmart, J. Vandooren, Flame structure studies of premixed ammonia/hydrogen/oxygen/argon flames: Experimental and numerical investigation 32 1277–1284.

[94] R. P. Lindstedt, F. C. Lockwood, M. A. Selim, Detailed Kinetic Modelling of Chemistry and Temperature Effects on Ammonia Oxidation 99 253–276.

[95] T. Norström, P. Kilpinen, A. Brink, E. Vakkilainen, M. Hupa, Comparisons of the Validity of Different Simplified NH_3 Oxidation Mechanisms for Combustion of Biomass 14 947–952.

[96] T. Mendiara, P. Glarborg, Ammonia chemistry in oxy-fuel combustion of methane 156 1937–1949.

[97] GRI-Mech, V., "Gas Research Institute, GRI-Mech, Ver. 3.0. <.

[98] R. Mével, S. Javoy, F. Lafosse, N. Chaumeix, G. Dupré, C.-E. Paillard, Hydrogen–nitrous oxide delay times: Shock tube experimental study and kinetic modelling 32 359–366.

[99] A. Omari, L. Tartakovsky, Measurement of the laminar burning velocity using the confined and unconfined spherical flame methods – A comparative analysis 168 127–137.

[100] R. R. Burrell, J. L. Pagliaro, G. T. Linteris, Effects of stretch and thermal radiation on difluoromethane/air burning velocity measurements in constant volume spherically expanding flames, Proc. Combust. Inst. 37 (2019) 4231–4238.

[101] B. Lewis, G. von Elbe, Determination of the Speed of Flames and the Temperature Distribution in a Spherical Bomb from Time-Pressure Explosion Records 2 283–290.

[102] N. Hinton, R. Stone, R. Cracknell, Laminar burning velocity measurements in constant volume vessels – Reconciliation of flame front imaging and pressure rise methods 211 446–457.

[103] D. Bradley, A. Mitcheson, Mathematical solutions for explosions in spherical vessels 26 201–217.

[104] A. Lefebvre, H. Larabi, V. Moureau, G. Lartigue, E. Varea, V. Modica, B. Renou, Formalism for spatially averaged consumption speed considering spherically expanding flame configuration 173 235–244.

[105] A. Moghaddas, K. Eisazadeh-Far, H. Metghalchi, Laminar burning speed measurement of premixed n-decane/air mixtures using spherically expanding flames at high temperatures and pressures 159 1437–1443.

[106] C. Luijten, E. Doosje, J. van Oijen, L. de Goey, Impact of dissociation and end pressure on determination of laminar burning velocities in constant volume combustion 48 1206–1212.

[107] K. Eisazadeh-Far, A. Moghaddas, H. Metghalchi, J. C. Keck, The effect of diluent on flame structure and laminar burning speeds of JP-8/oxidizer/diluent premixed flames, Fuel 90 (2011) 1476–1486.

[108] M. Faghih, Z. Chen, The constant-volume propagating spherical flame method for laminar flame speed measurement, Sci. 61 (2016) 1296–1310.

[109] C. Xiouris, T. Ye, J. Jayachandran, F. N. Egolfopoulos, Laminar flame speeds under engine-relevant conditions: Uncertainty quantification and minimization in spherically expanding flame experiments, Combust. Flame 163 (2016) 270–283.

[110] X. Zhang, S. P. Moosakutty, R. P. Rajan, M. Younes, S. M. Sarathy, Combustion chemistry of ammonia/hydrogen mixtures: Jet-stirred reactor measurements and comprehensive kinetic modeling, Combustion and Flame 234 (2021) 111653.

[111] G. J. Gotama, A. Hayakawa, E. C. Okafor, R. Kanoshima, M. Hayashi, T. Kudo, H. Kobayashi, Measurement of the laminar burning velocity and kinetics study of the importance of the hydrogen recovery mechanism of ammonia/hydrogen/air premixed flames, Combustion and Flame 236 (2022) 111753.

[112] S. A. Alturaifi, O. Mathieu, E. L. Petersen, An experimental and modeling study of ammonia pyrolysis 235 111694.

[113] A. A. Konnov, A. Mohammad, V. R. Kishore, N. I. Kim, C. Prathap, S. Kumar, A comprehensive review of measurements and data analysis of laminar burning velocities for various fuel+air mixtures, Prog. Energy Combust. Sci. 68 (2018) 197–267.

[114] M. J. Bedard, T. L. Fuller, S. Sardeshmukh, W. E. Anderson, Chemiluminescence as a diagnostic in studying combustion instability in a practical combustor 213 211–225.

[115] X. Zhu, A. A. Khateeb, W. L. Roberts, T. F. Guiberti, Chemiluminescence signature of premixed ammonia-methane-air flames 231 111508.

[116] A. Valera-Medina, M. Gutesa, H. Xiao, D. Pugh, A. Giles, B. Goktepe, R. Marsh, P. Bowen, Premixed ammonia/hydrogen swirl combustion under rich fuel conditions for gas turbines operation 44 8615–8626.

[117] A. A. Khateeb, T. F. Guiberti, G. Wang, W. R. Boyette, M. Younes, A. Jamal, W. L. Roberts, Stability limits and NO emissions of premixed swirl ammonia-air flames enriched with hydrogen or methane at elevated pressures 46 11969–11981.

[118] D. Pugh, J. Runyon, P. Bowen, A. Giles, A. Valera-Medina, R. Marsh, B. Goktepe, S. Hewlett, An investigation of ammonia primary flame combustor concepts for emissions reduction with OH*, NH2* and NH* chemiluminescence at elevated conditions 38 6451–6459.

[119] X. Zhu, A. A. Khateeb, T. F. Guiberti, W. L. Roberts, NO and OH* emission characteristics of very-lean to stoichiometric ammonia–hydrogen–air swirl flames 38 5155–5162.

[120] J. Choe, W. Sun, T. Ombrello, C. Carter, Plasma assisted ammonia combustion: Simultaneous NOx reduction and flame enhancement 228 430–432.

[121] S. Wiseman, M. Rieth, A. Gruber, J. R. Dawson, J. H. Chen, A comparison of the blow-out behavior of turbulent premixed ammonia/hydrogen/nitrogen-air and methane–air flames 38 2869–2876.

[122] F. Thiesset, F. Halter, C. Bariki, C. Lapeyre, C. Chauveau, I. Gökalp, L. Selle, T. Poinsot, Isolating strain and curvature effects in premixed flame/vortex interactions 831 618–654.

[123] C. Netzer, A. Ahmed, A. Gruber, T. Løvås, Curvature effects on NO formation in wrinkled laminar ammonia/hydrogen/nitrogen-air premixed flames 232 111520.

[124] S. Colson, Y. Hirano, A. Hayakawa, T. Kudo, H. Kobayashi, C. Galizzi, D. Escudié, Experimental and Numerical Study of NH_3 /CH_4 Counterflow Premixed and Non-premixed Flames for Various NH_3 Mixing Ratios 193 2872–2889.

[125] H. Xiao, S. Lai, A. Valera-Medina, J. Li, J. Liu, H. Fu, Study on counterflow premixed flames using high concentration ammonia mixed with methane 275 117902.

[126] R. C. Rocha, S. Zhong, L. Xu, X.-S. Bai, M. Costa, X. Cai, H. Kim, C. Brackmann, Z. Li, M. Aldén, Structure and Laminar Flame Speed of an Ammonia/Methane/Air Premixed Flame under Varying Pressure and Equivalence Ratio 35 7179–7192.

[127] C. Brackmann, V. A. Alekseev, B. Zhou, E. Nordström, P.-E. Bengtsson, Z. Li, M. Aldén, A. A. Konnov, Structure of premixed ammonia + air flames at atmospheric pressure: Laser diagnostics and kinetic modeling 163 370–381.

[128] H. G. Wolfhard, W. G. Parker, A Spectroscopic Investigation into the Structure of Diffusion Flames 65 2–19.

[129] A. Hayakawa, T. Goto, R. Mimoto, T. Kudo, H. Kobayashi, NO formation/reduction mechanisms of ammonia/air premixed flames at various equivalence ratios and pressures 2 14–00402–14–00402.

[130] S. M. Wiseman, M. J. Brear, R. L. Gordon, I. Marusic, Measurements from flame chemiluminescence tomography of forced laminar premixed propane flames 183 1–14.

[131] A. G. Gaydon, The Spectroscopy of Flames, Springer Netherlands.

[132] H. Kobayashi, A. Hayakawa, K. K. A. Somarathne, E. C. Okafor, Science and technology of ammonia combustion 37 109–133.

[133] A. H. White, W. Melville, THE DECOMPOSITION OF AMMONIA AT HIGH TEMPERATURES. 27 373–386.

[134] R. d'Agostino, F. Cramarossa, S. De Benedictis, G. Ferraro, Kinetic and spectroscopic analysis of NH3 decomposition under R.F. Plasma at moderate pressures 1 19–35.

[135] S. Mashruk, H. Xiao, D. Pugh, M.-C. Chiong, J. Runyon, B. Goktepe, A. Giles, A. Valera-Medina, Numerical Analysis on the Evolution of NH_2 in Ammonia/hydrogen Swirling Flames and Detailed Sensitivity Analysis under Elevated Conditions 1–28.

[136] H. Xiao, A. Valera-Medina, P. Bowen, S. Dooley, 3D Simulation of Ammonia Combustion in a Lean Premixed Swirl Burner 142 1294–1299.

[137] C. Lhuillier, P. Brequigny, F. Contino, C. Mounaïm-Rousselle, Experimental investigation on ammonia combustion behavior in a spark-ignition engine by means of laminar and turbulent expanding flames 38 5859–5868.

[138] Q. Fan, X. Liu, L. Xu, A. A. Subash, C. Brackmann, M. Aldén, X.-S. Bai, Z. Li, Flame structure and burning velocity of ammonia/air turbulent premixed flames at high Karlovitz number conditions 238 111943.

[139] X. Wei, M. Zhang, Z. An, J. Wang, Z. Huang, H. Tan, Large eddy simulation on flame topologies and the blow-off characteristics of ammonia/air flame in a model gas turbine combustor 298 120846.

[140] M. Zhao, D. Buttsworth, R. Choudhury, Experimental and numerical study of OH* chemiluminescence in hydrogen diffusion flames 197 369–377.

[141] Y. Liu, J. Tan, M. Wan, L. Zhang, X. Yao, Quantitative Measurement of OH* and CH* Chemiluminescence in Jet Diffusion Flames 5 15922–15930.

[142] C. Panoutsos, Y. Hardalupas, A. Taylor, Numerical evaluation of equivalence ratio measurement using OH and CH chemiluminescence in premixed and non-premixed methane–air flames 156 273–291.

[143] M. Mizomoto, Y. Asaka, S. Ikai, C. Law, Effects of preferential diffusion on the burning intensity of curved flames 20 1933–1939.